UC Irvine
UC Irvine Electronic Theses and Dissertations

Title

Pt/ionomer Transport and Interfacial Properties in Catalyst Layer of Polymer Electrolyte Fuel Cells

Permalink

https://escholarship.org/uc/item/483198v5

Author

Qi, Yongzhen

Publication Date

2022

Peer reviewed|Thesis/dissertation

UNIVERSITY OF CALIFORNIA, IRVINE

Pt/ionomer Transport and Interfacial Properties in Catalyst Layer of Polymer Electrolyte Fuel

Cells

DISSERTATION

Submitted in partial satisfaction of the requirements for the degree of

DOCTOR OF PHILOSOPHY

in Mechanical and Aerospace Engineering

by

Yongzhen Qi

Dissertation Committee:
Professor Iryna Zenyuk, Chair
Professor Plamen Atanassov
Professor Jack Brouwer

2022

TABLE OF CONTENTS

ii

iv

viii

LIST OF FIGURES

LIST OF TABLES

ACKNOWLEDGEMENTS

First and foremost, I would like to thank my advisor, Prof. Iryna Zenyuk, for her guidance and

studies, for high-quality work standards she upholds and installs in her students. I greatly admire

her technical expertise, hard work, exceptional creativity and her high energy drive for all our

projects. I have learned immensely from Iryna and I am grateful for her giving me an opportunity

to work on many intellectually stimulating and challenging cutting-edge research projects.

I would like to acknowledge my thesis committee, Professor Plamen Atanassov, Professor Jack

Brouwer for their valuable comments and discussions that helped in shaping my research

projects and this dissertation.

I am thankful to all SEE lab members for enjoyable collegial working atmosphere and for their

friendships. I want to thank Dr. Yu Morimoto and Masao Suzuki Shibata for their help on the

study of Pt ionomer interfacial and transport properties. I also benefited from working with Dr.

Jiangjin Liu, whose modeling skills complemented my catalyst layer ionic conductivity work. I

thank Ying Huang, Dr. Andrea Perego and Dr. Tristan Asset for doing imaging in carbon

corrosion study. I want to thank Dr Prantik Saha, Hungming Chang, Adrien Stejer, Arezoo Avid,

Kaustubh Khedekar and Devashish Kulkarni for helping me to integrate within the lab and

providing support and encouragement throughout these four years. I also want to thank Dr.

Dinesh Sabarirajan for passing the knowledge and teaching me all the experimental skills.

Finally, I am forever indebted my family and my wife Fan Yang for all their patience, support and encouragement, for having faith in my character and abilities.

VITA

Yongzhen Qi

2012-16 B.S. in Architecture Engineering, Shandong Jianzhu University, Jinan, China

2016-18 M.S. in Mechanical Engineering, Tufts University, Boston

2018-22 Ph.D. in Mechanical and Aerospace Engineering, University of California, Irvine

2021-22 Teaching Assistant, Department of Chemical and Biomolecular Engineering, University of California, Irvine

FIELD OF STUDY

Polymer electrolyte fuel cells

PUBLICATIONS

" Determining Proton Transport in Pseudo Catalyst Layers Using Hydrogen Pump DC and AC Techniques," Journal of The Electrochemical Society, 167 084521 (2020)

"Interpreting Ionic Conductivity for Polymer Electrolyte Fuel Cell Catalyst Layers with Electrochemical Impedance Spectroscopy and Transmission Line Modeling," Journal of The Electrochemical Society, 168 054502 (2021)

"Novel Fluorinated High Oxygen Permeability Ionomers for Proton Exchange Membrane Fuel Cells," Advanced Energy Materials, (under review)

"Understanding Ion Pathways and Area Effect For Polymer Electrolyte Fuel Cell with 2D Hydrogen Pump Model," (in preparation)

''Determining Platinum Ionomer Interfacial and Ion Transport Properties of Polymer Electrolyte Fuel Cell'' (under review)

"Electrochemical Characterizations and Carbon Corrosion for High Durability Carbon Support, (ready to submit)

ABSTRACT OF THE DISSERTATION

Pt/ionomer Transport and Interfacial Properties in Catalyst Layer of Polymer Electrolyte Fuel

By

Yongzhen Qi

Doctor of Philosophy in Mechanical and Aerospace Engineering

University of California, Irvine, 2022

Professor Iryna Zenyuk, Chair

Polymer electrolyte fuel cells (PEFCs) provide a promising way to mitigate global warming since these power sources produce no emissions of greenhouse gases. PEFCs convert chemical energy of hydrogen and air to electricity via electrochemical pathway. For broad deployment of PEFCs in transportation sector cost and durability need to be addressed. At the heart of the fuel cell is the catalyst layer, where platinum (Pt) catalyst is used to catalyze oxygen reduction reaction (ORR). Pt is typically dispersed on carbon support and with ionomer (such as Nafion) to enable ORR. Understanding Pt-ionomer interface is critical to enable PEFCs with low Pt content. Therefore, in this work Pt- ionomer interfacial and transport properties within the catalyst layers were examined using variety of electrochemical diagnostic techniques.

Optimizing electrode morphology with a more uniform ionomer distribution is key to reducing ohmic losses and increasing electrocatalyst utilization in PEFCs. For ionomer transport properties, we determined three different methods including direct current (DC) hydrogen pump (HP), HP electrochemical impedance spectroscopy (EIS) and H_2/N_2 EIS to investigate catalyst

layer ionic conductivity, and it was the first and unique study to compare each method. Apart from that, we developed an 1D H_2/N_2 EIS impedance fitting model, which enable us to evaluate catalyst layer ionic conductivity with good accuracy. For Pt ionomer interfacial properties study, we first studied performance and electrochemical characterizations for MEAs containing novel high oxygen permeability ionomers (HOPIs) synthesized by Giner, and a comparison was made between novel ionomer and commercial Nafion ionomer. After that, we investigated some possible factors which influence cell performance and catalyst/ionomer interfacial properties using 3M materials including Pt loading, ionomer content and carbon support types, which would bring thoughts and inspirations to community regarding the design of optimal catalyst layer. Finally, we studied Pt ionomer transport and interfacial properties change during carbon corrosion accelerated stress tests (ASTs). We performed both in-situ and ex-situ measurements on MEAs containing different types of carbon support, which enable us to better understand the causes for drop of performance from ionomer interfacial properties perspective.

Chapter 1. Introduction

1.1 Motivation

Fossil fuel, which is considered as non-sustainable energy source, is a major contributor of energy production for all nations, which also results in well-developed economies and high public living standard [1]. However, fossil fuel is also considered as the main cause of climate change due to the greenhouse gases emission after combustion [2]. In the Paris agreement, 2016, 195 countries agreed on "holding the increase in global average temperature well below 2 °C above pre-industrial levels" [3]. However, the United States total primary energy production increased from 69.4 quadrillion Btu in 2005 to 97.7 in 2021. With increase in energy production, energy consumption remained at around 98 quadrillion Btu. For energy production, utilization of fossil fuel occupied the majority of energy consumption and increased from 55 quadrillion Btu to 77 quadrillion Btu in the last 16 years. To be more specific, transportation sector used around 67 % of petroleum products. However, for renewable energy, energy production increased much faster, which from 6.2 quadrillion Btu to 12.3 quadrillion Btu. The fast development of renewable energy applications brought inspiration and great motivation to the public and community [4]. Furthermore, hydrogen has high potential for renewable market penetration, as when used in electrochemical devices, such as PEFCs, no emissions are produced. [5].

According to the 2021 annual survey of more than 1,000 executives in the global automotive industry, 68 % people were concerned about the sustainability and emissions that are being produced currently [6].

In December 2014, Toyota launched the world's first commercially available fuel cell vehicle (FCV) the "Mirai" powered by the Toyota Fuel Cell System (TFCS) [7]. The long diving range and fast gas filling properties enable PEFCs vehicles to become competitive to commercial internal combustion vehicles (ICEs). Apart from that, the environmental-friendly characterization makes PEFCs potentially can be an alternative way to mitigate global warming. Although PEFC can be used as sustainable and environmental-friendly device, which provides a promising way to mitigate the emission of greenhouse gases, commercial PEFC using Pt as precious catalyst material has several issues regarding kinetics, durability and mass transport, etc [8,9]. Therefore, there is urgent need to reduce the amount of Pt used in the PEFCs and this thesis addresses this problem.

1.2 Background

In the automotive sector, PEFCs are being developed to replace the internal combustion engines (ICEs) for automobiles as their low operation temperature and sufficient reactant gas. Light duty and heavy duty vehicles and as electric vehicle range extenders, due to their high efficiency and zero tail-pipe emissions [10,11]. However, as PEFC operates, it experiences many losses and it is critical to diagnose the losses. In this section, the principles of PEFC operation will be discussed. Apart from that, performance losses that PEFC experiences and challenges of PEFC will be discussed.

1.2.1 Polymer electrolyte fuel cells operating principles

PEFCs are electrochemical devices that convert chemical energy of H_2 and O_2 into electricity, and during energy conversion, water and heat are produced. **Figure 1.1** shows the schematic of

PEFC's components and how it operates. For the most common PEFC, it has different components clamped and combined in a sandwich-shape. As **Figure 1.1** shows below, it contains one gas diffusion layer (GDL) and catalyst layer for both anode and cathode. There is a polymer membrane located in the middle, which separates anode and cathode. Bulk perfluorinated sulfonic acid bulk film is the most commonly used membrane material, which conducts H^+ from anode to cathode. On the anode side, H_2 is used and it diffuses through porous media (PD) and micro porous layer (MPL) to reach anode catalyst layer. After that it forms H^+ and e^- via hydrogen oxidation reaction (HOR). As H^+ are transported through the membrane, e^- are transported through the outer circuit as the membrane is electron-nonconductive. On the cathode side, O_2 diffuses though cathode side GDL and MPL then reach catalyst layer. After that, O_2 reacts with H^+ coming through the membrane and e^- coming through the out circuit to form water and release heat, which denotes oxygen reduction reaction (ORR).

$$H_2 \rightarrow 2H^+ + 2e^- \ (HOR) \qquad 2H^+ + 2e^- + \frac{1}{2}O_2 \rightarrow H_2O \ (ORR)$$

Total reaction: $H_2 + \frac{1}{2}O_2 \rightarrow H_2O$
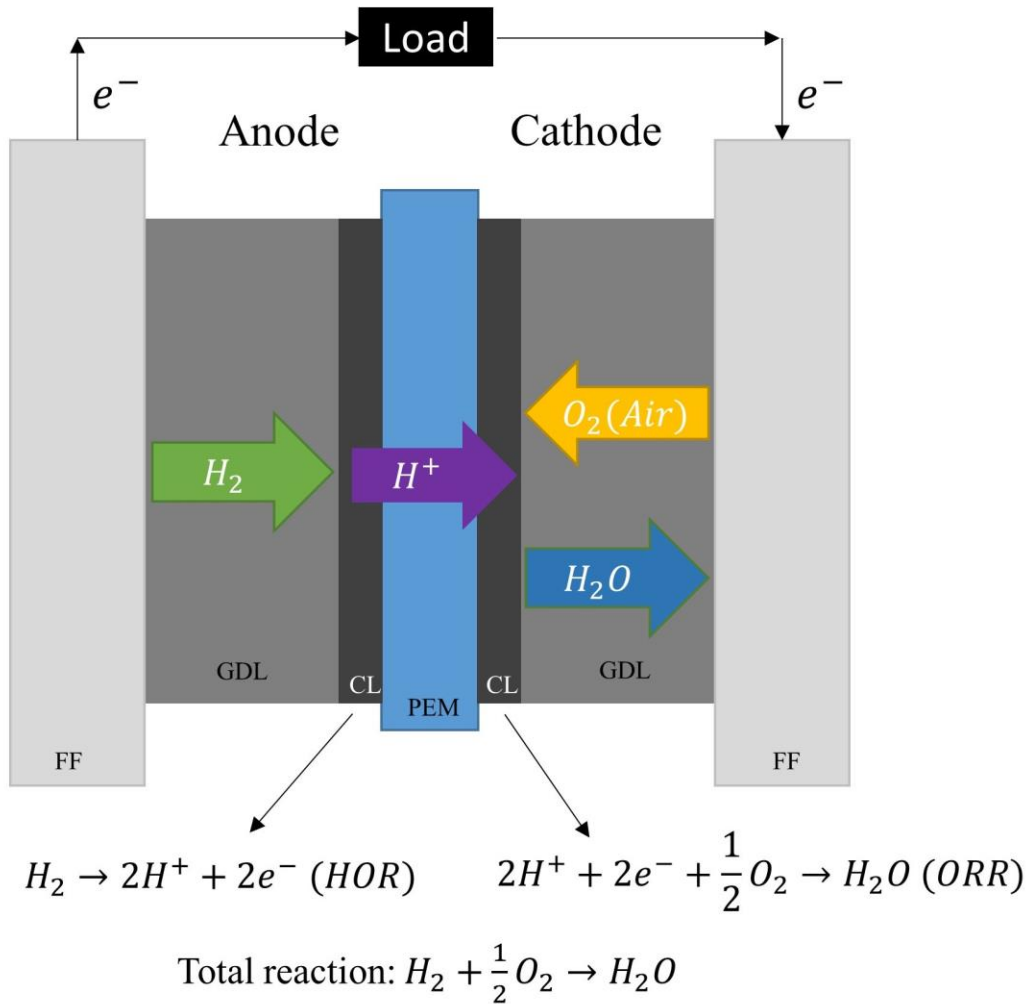
Figure 1.1 Polymer electrolyte fuel cell compositions and working principles, where anode and cathode reactions are shown, as well as total reaction.

1.3   PEFCs challenges

1.3.1   Precious catalyst material loading

Platinum nanoparticles dispersed in carbon support (Pt/C) with particle size around 50 nm are used as the most common catalyst material for PEFC. They have higher catalytic activity and better stability than other noble metals in strongly acidic electrolytes at low temperature [12]. One of the key challenges preventing PEFCs to be competitive with the ICEs is the relatively

high amounts of expensive platinum (Pt) used. Roland Berger concluded that unless the use of Pt was reduced to less than 10 gPt/vehicle, FCEVs would remain as a small part of global vehicles production [13]. Current state-of-the-art fuel cell vehicles is still using more than 20 grams per vehicle. To be competitive to ICEs vehicles, however, less than 5g/20g of Pt per light/heavy-duty vehicle is recommended [14–16], respectively. However, DOE's study also showed that further reducing Pt loading would also cause increased stack cost to compensate the performance drop for low-loaded PEFCs [17]. Also with Pt loading decreased, there is an unexplained mass transport resistance shown in performance plot (**Figure 1.2**), and the resistance is relative to the local effects at catalyst sites [18]. However recently, great progress has been made in the research community. Both Pt activity and dispersion on carbon particles were much improved by using different approach. Brookhaven National Lab developed Pt-monolayer catalyst by placing Pt atoms on the surface of support material to eliminate the waste of Pt [19,20]. Argonne National Lab found Pt-skin overlaying on PtNi (111) single crystal showed high ORR activity. After that, with developed synthesis technology, shaped controlled PtNi with optimal size was found to have greater ORR activity in a rotating-disk electrode (RDE) [21–25]. More advanced Pt catalyst core structure compositing Pt-skin and sublayers in binary Pt-alloy system also showed greater durability and activity [26–28], and was selected as main catalyst material in Toyota Mirai PEFCV [29].
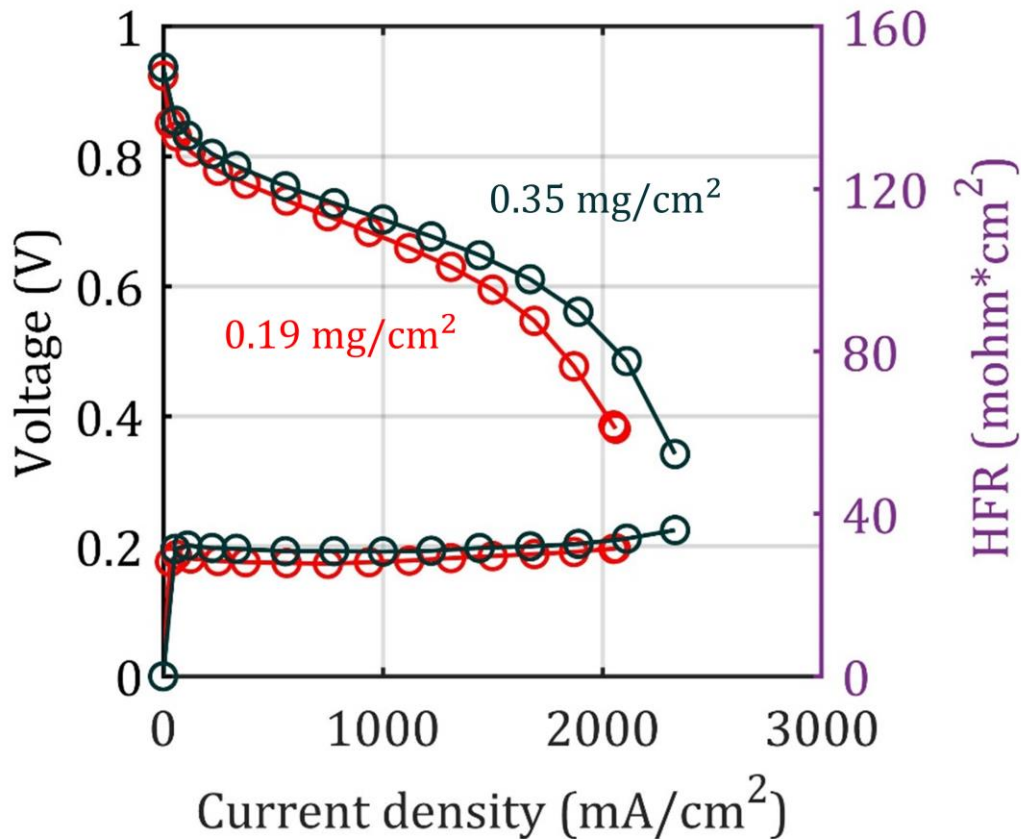
Figure 1.2 Polarization curve comparison between MEAs with different Pt loadings at 80 °C, 100 % and 150 kPa using H$_2$/air with flow rates of 1/1.5 SLPM.

1.3.2 Degradation and electrochemical surface area (ECSA)

Due to the extended lifetime of PEFC and targets published by DOE, as 5000 hours for light duty vehicle [30], one biggest concern is the ECSA loss [31–35] during the operation causing significant performance drop. One reason is that Pt nanoparticles dissolve and re-deposit onto some existing Pt particles or form Pt band within the membrane [36] due to Ostwald ripening and particle coalescence [37–40]. Pt dissolution occurs during potential cycling from 0.6 V to 0.95 V due the formation of Pt ions (**Figure 1.3**), and catalysts accelerated stress test (AST) comprises 30000 cycles using 0.6/0.95 V constant voltage hold with 3 s duration time was

proposed by DOE, which has been shown to equate to a projected system lifetime of 5,000 hours

[41]. Apart from that, carbon support degradation also is another reason causing the reduction of

ECSA, which will be discussed in the later chapter.

$$PtOH \rightarrow PtO + H^+ + e^-$$

$$Pt + H_2O \rightarrow PtOH + H^+ + e^-$$

$$Pt \rightarrow Pt^{2+} + 2e^-$$
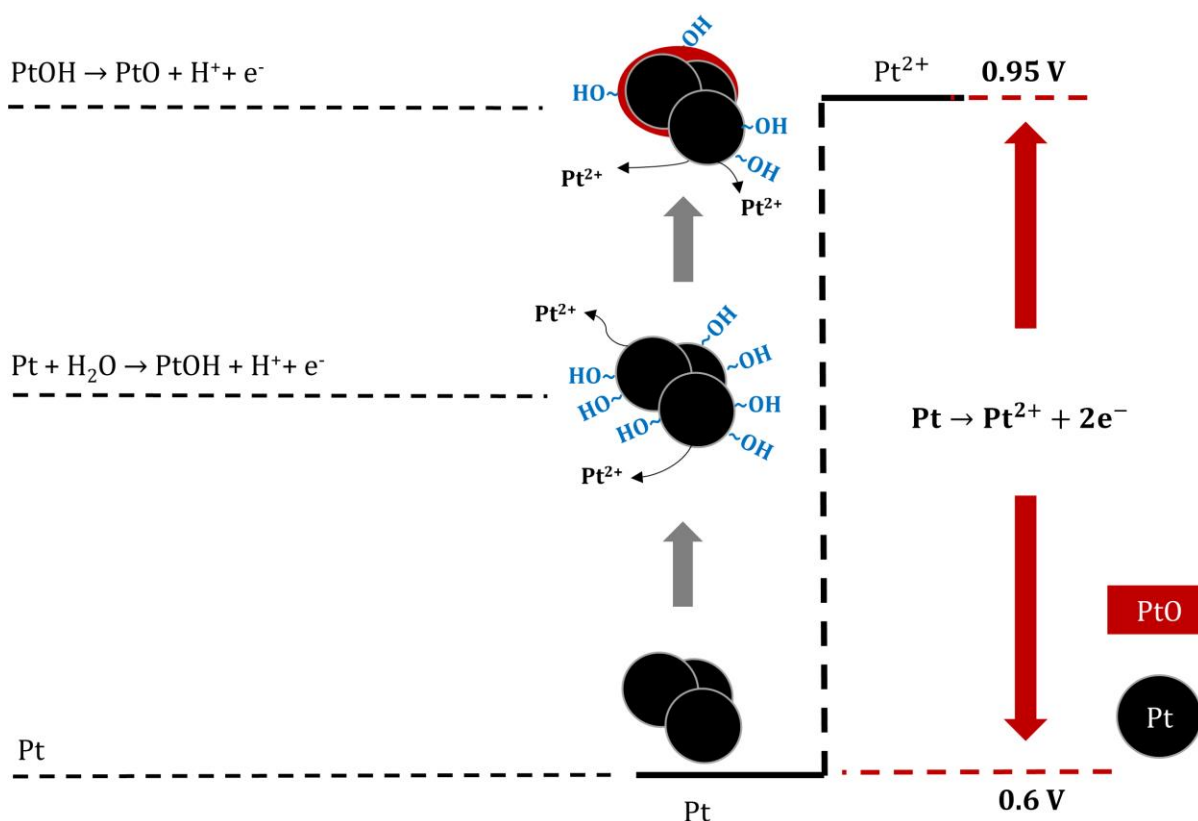
Figure 1.3 Mechanism of Pt dissolution by applying square wave potential hold from 0.6 V to 0.95 V using 0.2/ 0.3 SLPM H_2/N_2.

1.3.3 Ionomer poisoning and coverage

Ionomer is the most commonly used as a binder in catalyst layer and H^+ conductor in catalyst

layer for PEFCs. For ionomer, perfluorinated sulfonic acid polymers (PFSA) ionomer for

example Nafion, is the most used ionomer type due to their high chemical stability and H^+

conductivity. PFSA ionomer consists of an electrically neutral semicrystalline polymer backbone

(polytetrafluoro- ethylene (PTFE)) and a randomly tethered side-chain with a pendant ionic group, SO_3^- acid group (polysulfonyl fluoride vinyl ether). Although it provides H^+ accessibility and has good chemical stability, it suppresses ORR activity, as well [42,43]. Subbaraman et al. observed deteriorated ORR because of adsorptions of sulfonate moieties in the ionomers on the Pt surface [44,45]. Kodama et al. found at dry condition, sulfonate moieties of ionomer showed greater absorptivity, causing ORR activities of Pt catalysts seriously deteriorated in PEFCs operation [46].

Apart from suppression of ORR activity, ionomer also deteriorates mass transport under high current density operation. When ionomer contacts with Pt, the perfluoroalkyl chain is oriented parallel to the Pt surface as **Figure 1.4** shows. ORR is suppressed because of the interaction between the ether group and Pt surface via the lone pair of the oxygen atom in addition to van-der-Waals interactions between perfluorinated parts and the surface [18,47]. In this case, O_2 transfer is difficult, since O_2 has to penetrate PTFE backbone to reach the reaction site.
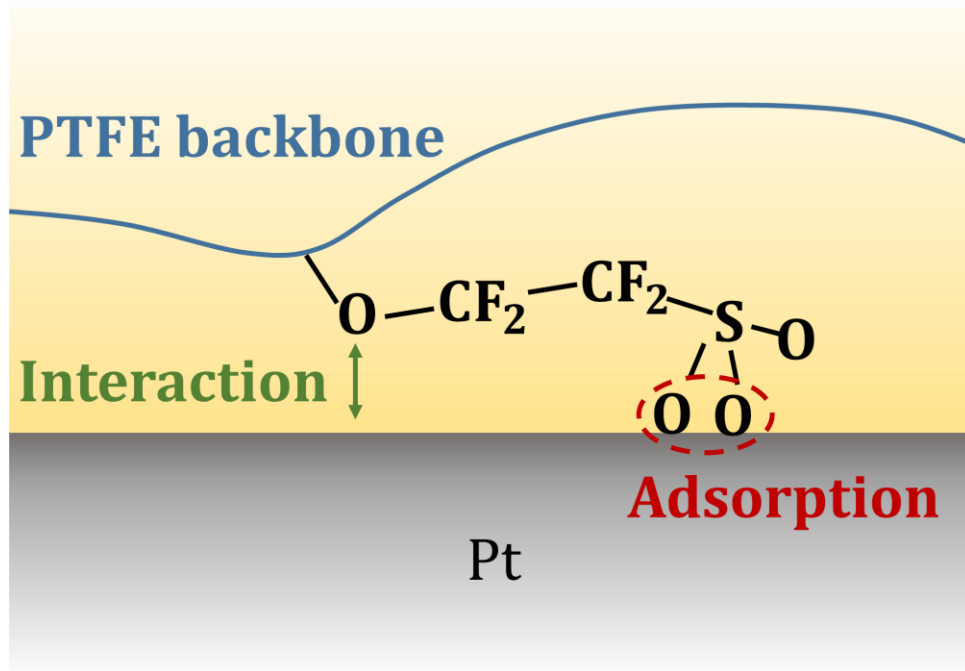
Figure 1.4 Pt/ionomer interface and adsorbed structure of PESA anion on Pt surface [47].

1.4 Scope of thesis work

This dissertation discusses the study of Pt/ionomer interfacial and transport properties in PEFC.

This dissertation is divided into 6 chapters. Chapter 2 is the introduction to all the material and

techniques used in this work. The next two chapters focus on Pt/ionomer transport properties.

Chapter 3 focuses on determining catalyst layer ionic conductivity using hydrogen pump method.

Chapter 4 focuses on determining catalyst layer ionic conductivity using H_2/N_2 EIS method.

Apart from that, two equivalent circuits were developed and used to get the ionic conductivity of

a catalyst layer. Chapter 5 investigates the Pt/ionomer interfacial and transport properties for

MEA using novel ionomers. Chapter 6 shows the work on Pt/ionomer interfacial properties,

work on 3M ionomer, also different possible factors were investigated. For example, Pt loading,

I/C ratio, carbon support type and process of cell conditioning and voltage recovery. Chapter 7

studies the Pt/ionomer interfacial and transport properties change during carbon corrosion AST. Then final chapter reviews the conclusion and contributions of this research and makes recommendations for future work.

Chapter 2. Experimental methodologies

2.1   Introduction

In this chapter, both experimental setups and testing protocols are introduced. Based on the testing protocols, calculation method interpretations were carried on, then data analysis and results sections will be shown in later chapters.

First of all, information of pseudo catalyst electrodes, catalyst electrode, polymer electrolyte membranes and catalyst coated membranes (CCMs) which were applied and used in this thesis work are provided. For ionomer transport properties study, especially for catalyst layer ionic conductivity measurement study, in-house-made CCMs were used by hot pressing electrodes and membranes manufactured by 3M. For ionomer interfacial properties study, various CCMs from different collaborators were used. For example CCMs manufactured by Giner lab were used and tested to measure interfacial properties of novel ionomer, CCMs manufactured by 3M company were tested to measure possible factors that would influence ionomer interfacial properties and CCMs manufactured by IRD company were tested to exam the interfacial properties change of ionomer during the carbon corrosion AST.

Second part covers the testing protocols showing how measurements were carried on and elaborated, including measurements of voltage cycling break-in, voltage recovery, polarization curves, mass activity, cyclic voltammetry, electrochemical impedance spectroscopy, CO

displacement and stripping and carbon corrosion. Third part shows the calculation methods clarifying how data were processed. Here, calculations of ECSA, double layer capacity, sulfonic acid group coverage and ionomer on Pt coverage.

Fourth part of the section shows the testing protocols for ex-situ measurements including scanning electron microscope (SEM), energy dispersive spectroscopy (EDS), transmission electron microscope (TEM), X-ray fluorensence (XRF), and X-ray photoelectron spectroscopy (XPS).

2.2   Material preparation

2.2.1   Material in HP set up (chapter 3)

2.2.1.1   Anode/cathode electrodes and flow-fields used in HP set up

Anode and cathode gas-diffusion electrodes (GDEs) were made in-house using Sigracet SGL 29 BC and catalyst ink with Pt loading of 0.3 mg/cm^2, and I/C ratio of 0.8. Catalyst inks were prepared by mixing the components (typically 4–5 g of catalyst or carbon per batch) into an ink containing water and alcohols (such as nPa) at a ratio of 1:3. The carbon or catalyst powder was added first with water, followed by additional solvents and ionomer solution. After combining all the components, the catalyst ink or carbon ink was mixed by using sonicator and homogenizer for 1 hour, respectively. Using the pipettes, the catalyst inks were dropped onto the Sigracet SGL 29 BC gas diffusion layers and dried at room temperature for 36 hours. In this work, 50 cm² 14 channel serpentine flow-fields with channel and land width of 0.5 mm x 0.5 mm was used (**Figure 2.1**).
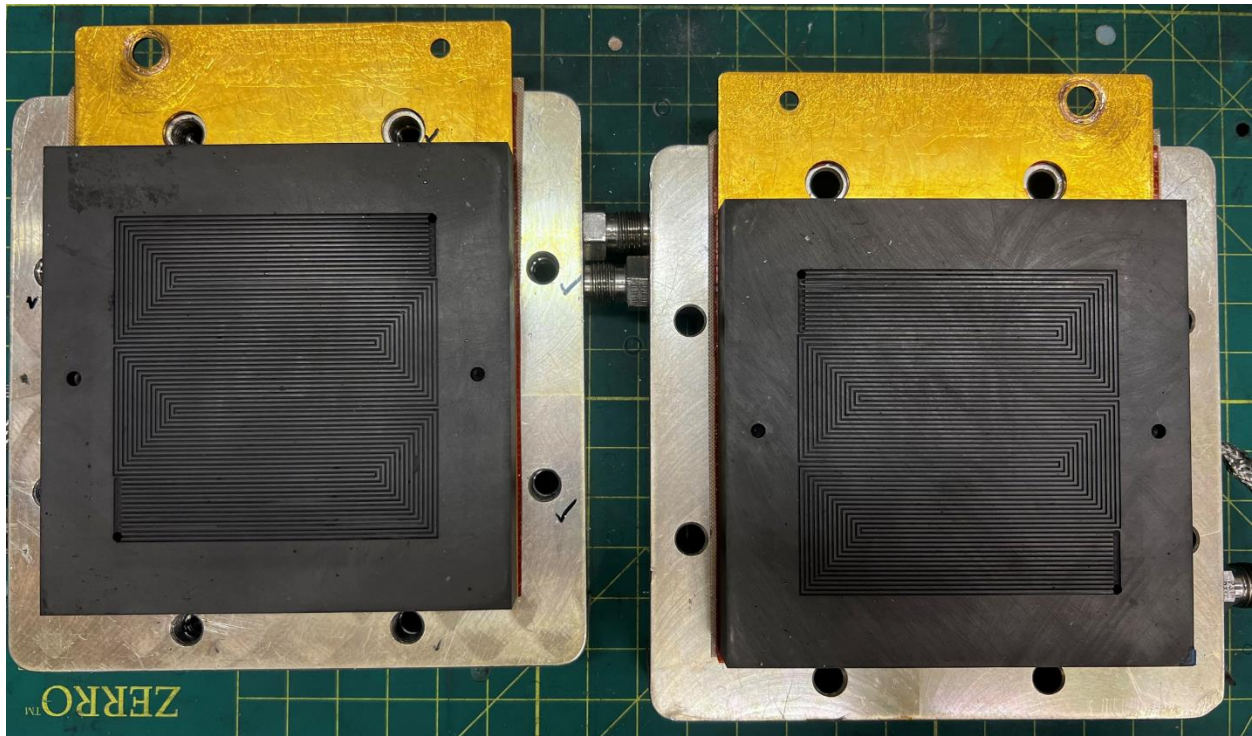
Figure 2.1 A photograph of a 50 cm^2 14 channel serpentine flow field developed by DOE.

2.2.1.2   Electrode used in HP set up

For catalyst layer ionic conductivity measurement, due to the material limitation regarding to configuration of HP set up, Pt/C couldn't be used as the internal layers. In that study, pseudo catalyst layers (PCLs) were used and hot pressed between two membranes in the set up. PCLs were fabricated by 3M with Vulcan XC-72 carbon and ionomer dispersion. The PCLs shown in **Figure 2.2** contained 3M 825 EW ionomer with ionomer-to-carbon (I/C) ratios of 0.6, 1.0 and 1.4 and Vulcan XC72 carbon black as Vulcan XC-72 is commonly used as a carbon support for metal on carbon catalysts (example: TKK 10V50E).
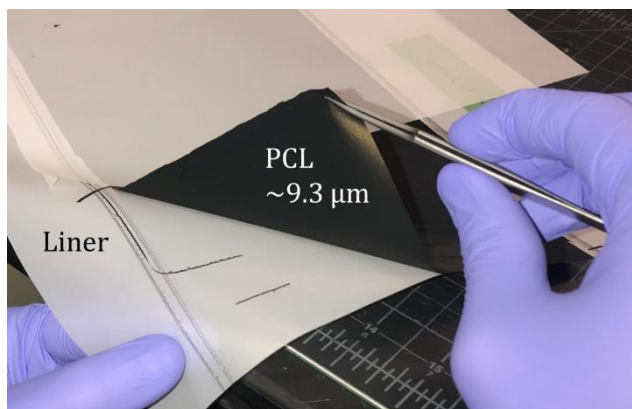
Figure 2.2 A photograph of PCL peeling off the liner.

2.2.1.3 CCM manufacturing in HP set up

For HP set up, carbon-ionomer composite layers were peeled off from the liners and stacked into configuration of 2, 4, 6 and 10 layers between 250 μm Teflon fiberglass sheets and hotpressed at 120 °C and 40 psi pressure for 5 min. The hot-pressed layers were masked by Kapton film with opening of 2 cm × 2 cm for active area, after which two membranes were hot-pressed onto the pseudo-catalyst layers.

2.2.2 Material used in H_2/N_2 EIS set up (chapter 4)

2.2.2.1 Anode electrodes used in H_2/N_2 EIS set up

For PCL ionic conductivity study, anode catalyst layers were laminated at 3M and consisted of Tanaka TKK 10V50E (47 wt% Pt on Vulcan carbon), 3M 800 EW ionomer at an I/C ratio of 0.8 and a Pt loading of 0.19 mg/cm^2.

For catalyst layer ionic conductivity study, anodes for all the MEAs consisted of 0.10 mg Pt/cm^2 loading, 50 wt% Pt on graphitized carbon ($\sim$80 $m^2\ g^{-1}$ surface area), 3M 800 EW I/C = 0.8 ionomer.

2.2.2.2   Electrodes (cathode electrode) used in H_2/N_2 EIS set up

For PCL ionic conductivity study, all the PCLs were manufactured by 3M with same carbon support type and I/C ratios were chosen as cathode electrodes to enable comparison with HP set up.

For catalyst layer ionic conductivity study, four different MEAs with Pt/C layers as cathode catalyst layers were manufactured at 3M company with Pt/C loading of 0.2–0.3 mg/cm^2, whereas ionomer fraction and type of carbon support were varied. Table 1 shows the cathode sides for four MEAs used in this study.

Table 1. Cathode side for four MEAs used in catalyst layer ionic conductivity study using H_2/N_2 EIS method

	I/C ratio	Pt loading (mg/cm^2)	Type of cathode carbon
MEA 1	0.4	0.29	Graphitized carbon (GrC)
MEA 2	0.9	0.21	Graphitized carbon (GrC)
MEA 3	1	0.24	High-surface area carbon (HSC)
MEA 4	1.2	0.205	Vulcan XC72, medium

surface area carbon (MSC)

2.2.2.3   CCM manufacturing in H_2/N_2 EIS set up

For H_2/N_2 EIS set up, to measure ionic conductivity of PCL, house-made CCMs were manufactured. The cathode PCL was hot pressed onto the other half of the CCM and sandwiched between Kapton® polyimide sheets of 25 μm thickness, masking an active area of 5 cm^2. The hot press condition was 140 °C and 2000 kg total pressure. The duration of hot-press procedure was 3 min.

2.2.2.4   Gas diffusion layers (GDLs) and flow-fields (FFs) used in H_2/N_2 EIS set up

Sigracet SGL 29 BC was used as the gas diffusion layer (GDL). Teflon fiberglass sheet layer of 180 μm thickness was used on both sides between MEA and bipolar plate as hard-stop gasket to achieve a 20% compression of the GDL. Scribner hardware with 5 cm2 flow-field with a single serpentine of 1 mm × 1 mm land and channel was used (**Figure 2.3**).
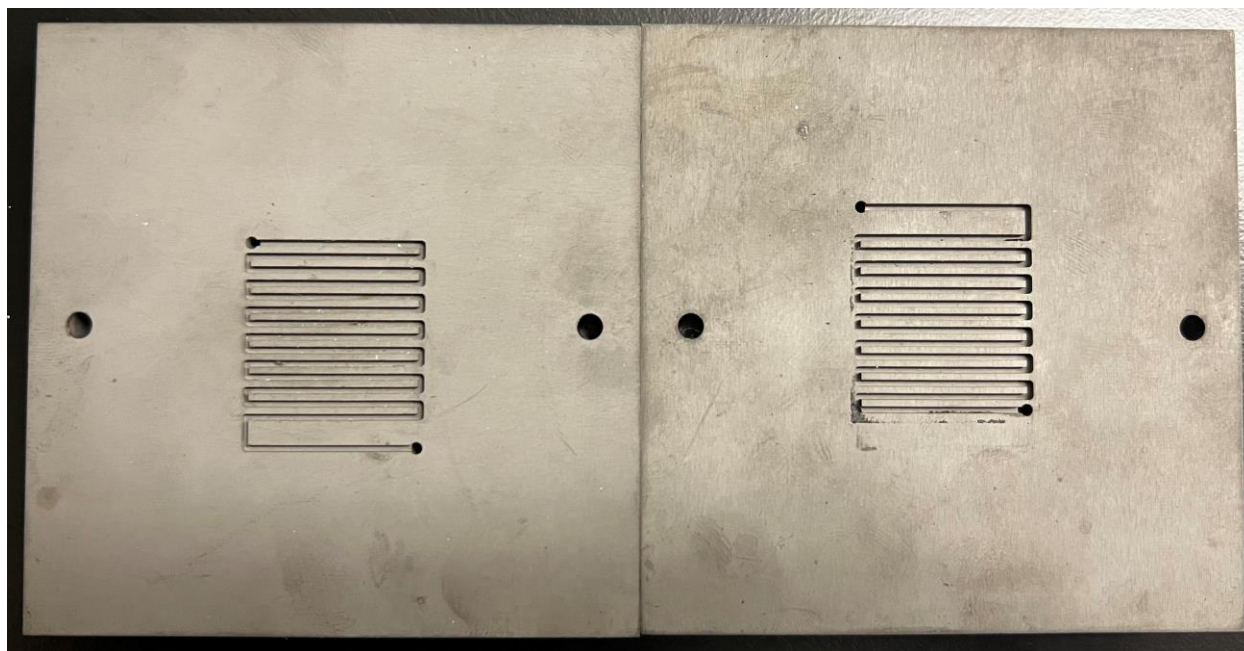
Figure 2.3 A photograph of a 5 cm^2 single serpentine Scribner flow field.

2.2.3 Material in novel ionomer study (chapter 5)

2.2.3.1 CCMs in novel ionomer study

Cathode electrodes were hot pressed onto a N211 membrane and the resulted half CCMs was

integrated with 0.2 mg cm^{-2} Pt/V anode to make full MEAs. Table 2 shows the cathode sides for

four MEAs used in this study.

Table 2. List of PDD ionomers synthesized at CMS and their physical properties.

Ionomer	Composition	Estimated PDD content (mole%)	EW (g/mole)	Intrinsic Viscosity (dL/g)
PDD 1	PDD/PFSVE/M	62 – 68	754	0.20

PDD 2	PDD/PFSVE/M	67 – 73	863	0.31
PDD 3	PDD/PFSVE/M	67 – 73	859	0.31
PDD 4	PDD/PFSVE/M	70 – 76	953	0.20

2.2.3.2 Gas diffusion layers (GDLs) and flow-fields (FFs) used in novel ionomer study

In this work, the 50 cm^2 14 channel serpentine flow-fields with channel and land width of 0.5 mm x 0.5 mm were used in a second configuration where 6 cm x 6 cm gaskets with 180 μm thickness were used on both sides between the MEA and flow-field plate. Between the catalyst layer and GDL, a 4.8 cm x 4.8 cm sub-gasket with 12 μm thickness was used to prevent gas cross-over and mask the active area. This configuration's MEA active area was 23 cm^2. A 5.8 cm x 5.8 cm Freudenberg H23C6 carbon paper was used as a gas diffusion layer for this configuration with a total cell compression of 25 %.

2.2.4   Material in ionomer interfacial properties impact factors study (chapter 6)

2.2.4.1 CCMs used in ionomer interfacial properties impact factors study

In this study, catalyst coated membranes (CCMs) with various Pt loadings, ionomer to carbon (I/C) ratios and different types of carbon support manufactured by 3M were investigated. In all of the MEAs the ionomer was 3M 800 EW PFSA. The anodes for all the CCMs consisted of 0.10 mg Pt/cm^2 loading, 50 wt% Pt on graphitized carbon (TKK 10EA50E, ~200 m^2/g carbon surface area), 3M 800 EW I/C = 0.8 ionomer. 3M 800 EW 20 µm membrane was used in all these CCMs. Table 3 shows cathode electrodes for four cells and their specifications.

Table 3. Cathode side for four cells used in Pt/ionomer properties study.

	Cathode I/C ratio	Cathode Pt loading (mg/cm^2)	Cathode carbon support	Ionomer type
cell 1	1	0.24	High-surface area (HSA) carbon	3M800 PFSA
cell 2	0.9	0.19	Vulcan XC72, medium surface area (MSA) carbon	3M800 PFSA
cell 3	0.9	0.35	Vulcan XC72, medium surface area (MSA) carbon	3M800 PFSA
cell 4	0.3	0.2	Vulcan XC72, medium surface area (MSA) carbon	3M800 PFSA

2.2.4.2 Gas diffusion layers (GDLs) and flow-fields (FFs) used in ionomer interfacial properties impact factors study

5 cm x 5 cm Freudenberg H23C6 with micro porous layers (MPLs) were used as the GDLs. The 50 cm^2 14 channel serpentine flow-fields with channel and land width of 0.5 mm x 0.5 mm were masked off by using a 5 cm x 5 cm Teflon fiberglass sheet layers of 180 μm thickness on both sides between MEA and bipolar plate as hard-stop gaskets also to achieve a 20 % compression of the GDLs on both anode and cathode side. The cell active area was further masked off to 20.25

cm^2 by using a 4.5 cm x 4.5 cm polyester film of 12.7 µm thickness as a sub-gasket on both sides between CCMs and GDLs to prevent reactant gas crossover.

2.2.5   Material in carbon corrosion study (chapter 7)

2.2.5.1   CCMs in carbon corrosion study

Catalyst inks and MEAs were made at IRD company. For all membrane electrode assemblies (MEAs), PFSA membranes with thickness of 18µm were used. The anodes and cathode for all MEAs consisted of same Pt loadings of 0.1 mg/cm^2 and 0.5 mg/cm^2, respectively. In this work, HSAC and graphitized carbon supports were used on cathode sides and compared.

2.2.5.2   Gas diffusion layers (GDLs) and flow-fields (FFs) used in carbon corrosion study

50 cm^2 14 channel serpentine flow-fields with channel and land width of 0.5 mm x 0.5 mm were masked off by using a 5 cm x 5 cm Teflon fiberglass sheet layers of 180 µm thickness on both sides between MEA and bipolar plate as hard-stop gaskets also to achieve a 20 % compression of the GDLs on both anode and cathode side. The cell active area was further masked off to 20.25 cm^2 by using a 4.5 cm x 4.5 cm polyester film of 12.7 µm thickness as a sub-gasket on both sides between CCMs and GDLs to prevent reactant gas crossover. In this work, 5 cm x 5 cm Freudenberg H23C6 with micro porous layers (MPLs) were used as the GDLs.

2.3 In-situ testing protocols

2.3.1 Voltage cycling break-in.

The break-in protocol is fundamental for the correct activation of the MEA. Voltage cycling break-in process was performed by using 0.8/1.5 standard liter per minute (SLPM) ultra-high purity (UHP) H_2 and compressed air at anode and cathode, respectively at 80 °C and 100 % RH with an absolute backpressure of 150 kPa. A series of constant voltages holds with 200 repeated cycles were performed by applying constant voltages to the cells at 0.8 V, 0.5 V and 0.2 V for 30 seconds, respectively.

2.3.2 Voltage recovery

Voltage recovery process is considered as a valuable step for the removal of sulfate, resulting in improved electrochemical performance [48]. In this work, it involved holding the cell at 0.1 V for 7200 seconds using 0.45/0.25 SLPM UHP H_2 and air at the anode and cathode, respectively at 40 °C and 150 % RH with an absolute backpressure of 150 kPa. Previous study also showed recovery process was an effective way to remove the surface contaminants and increased the electrochemical surface area (ECSA) [49].

2.3.3 Carbon corrosion accelerated stress test

Carbon corrosion ASTs for PEFC components were developed by U.S. Department of Energy (DOE), the U.S. Drive Fuel Cell Tech Team (FCTT) [50]. It involved CV measurements cycling from 1-1.5 V at 500 mV/s under H_2/N_2. Specifications, as suggested by DOE, are shown in Table 4.

Table 4. DOE carbon corrosion testing protocol

Cycle	Triangular wave between 1.0 V and 1.5 V. Scan rate of 500 mV s^{-1}
Total number of cycles	1,000 cycles for HSAC and 10000 cycles for GrC
Reactant gases	H$_2$/N$_2$ with flow rates of 0.2/0.3 SLPM respectively
Cell temperature	80 ˚C
Gas inlet temperature	80 ˚C
Relative humidity	100 %
Outlet Pressure	Atmospheric

2.3.4 H$_2$/Air polarization curves

Polarization curve is the most common way to measure fuel cell performance, and it displays the voltage output of the fuel cell for a given current density. Typically, the result of H$_2$/air polarization curve provides information regarding the chemical and physical reactions when at given current loading and operation condition. The result of the curve shown in **Figure 2.4** shows different shapes since it experiences different voltage losses when current sweep was applied.

- Region I represents the voltage loss dominated by activation (kinetic) overpotential at the electrodes.

- Region II represents the voltage loss dominated by ohmic loss of the fuel cell, which includes all electrical and ionic resistance through the electrolyte, catalyst layers, cell interconnects, and contacts.

- Region III represents the voltage loss dominated by mass transport loss of the fuel cell, since porous medias are occupied by generated liquid water at high current region, which causes reactant gases transport limitation.

- Region IV represents the voltage difference from Nernst thermodynamic equilibrium potential caused by cross over H_2, and contaminants on the electrode surfaces.

- Region V represents the voltage difference from the thermal neutral voltage, which is calculated by the entropy of H_2 combustion.
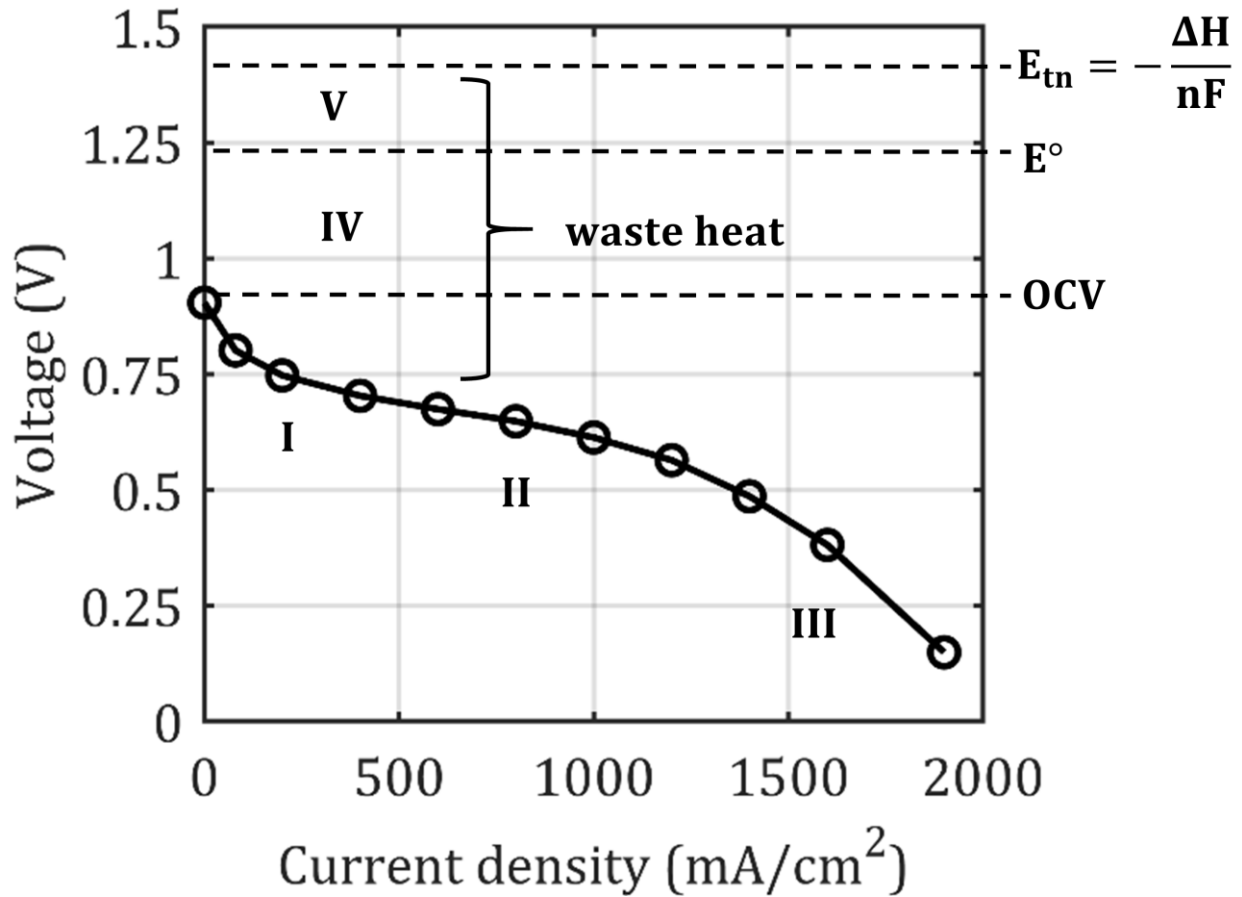
Figure 2.4 Polarization curve of polymer electrolyte fuel cell, where five regions are identified.

For novel ionomer performance testing, H_2/Air polarization curves were measured at 80 °C, 100 % RH, using 1.5/3 SLPM fixed flows at 150 kPa. The cell voltage was measured between open circuit voltage and 0.2 V with a potential step of 0.05 V and a 30 s with a dwell time at each point. During the polarization curve measurements, high frequency resistance (HFR) was measured. Specifications are collected in Table 5

Table 5. Polarization curve testing protocol using 1.5/3 SLPM H_2/Air fixed flow rate

Current	Dwell time	Cell	Gas	RH	Back

| density | [s] | temperature | temperature | [%] | pressure |
[A cm^{-2}]		[°C]	[°C]		[kPa]
3	180	80	80	100	150
2.75	180	80	80	100	150
2.5	180	80	80	100	150
2.25	180	80	80	100	150
2	180	80	80	100	150
1.75	180	80	80	100	150
1.5	180	80	80	100	150
1.25	180	80	80	100	150
1	180	80	80	100	150
0.75	180	80	80	100	150
0.5	180	80	80	100	150
0.25	180	80	80	100	150
0.1	180	80	80	100	150
0	180	80	80	100	150

In carbon support corrosion study. The polarization curve protocol involved I-V curves measurements using constant current mode from 2 to 0 A/cm^2 at 80 °C, 100 % RH with an absolute backpressure of 150 kPa. The polarization curve measurements were conducted in anodic direction with the stoichiometry factors of 2/2 on anode/cathode respectively. During the polarization curve measurements, high frequency resistance (HFR) was measured. Specifications are shown in Table 6.

Table 6. Polarization curve testing protocol using H$_2$/Air with 2/2 stoichiometry flow rate

Current density [A cm^{-2}]	Dwell time [s]	Cell temperature [°C]	Gas temperature [°C]	RH [%]	Back pressure [kPa]
2	180	80	80	100	150
1.75	180	80	80	100	150
1.5	180	80	80	100	150
1.25	180	80	80	100	150
1	180	80	80	100	150
0.75	180	80	80	100	150
0.5	180	80	80	100	150
0.25	180	80	80	100	150
0.1	180	80	80	100	150
0	180	80	80	100	150

2.3.5 H$_2$/H$_2$ DC and AC methods

For H$_2$ pump DC method, ultra-high purity (UHP) hydrogen gas was used as the feed gas at both anode and cathode at a flow rate of 0.75 LPM. For each RH potentials were set from OCV to -0.4 V, held for 10 min per voltage point at 80 ℃ with 150 kPa back pressure, and current density was recorded. At each point, an EIS was conducted so called H$_2$ pump AC method with 10 mV amplitude and the frequency range of 500 kHz to 100 mHz. The measurements were recorded at the rate of 6 points per decade and a total of 36 points (total about 10 min per potential). Both HP

and EIS measurements were repeated three times for each PCL, one after another, to account for repeatability and standard error measurements. These consecutive HP and EIS measurements also ensured that PCLs are completely in equilibrium with gas in flow-channel. Each HP and EIS pol curve took 100 min to complete per RH, so it took 300 min (5 hours) to complete three HP and EIS curves. The experiments were repeated at RH conditions from 50 – 120 % RH with step-size of 10 % RH. Specifications are collected in Table 7.

Table 7. Constant voltage hold at different RHs for pseudo catalyst layer ionic conductivity using DC HP method

DC voltage hold	OCV, -0.1 V, -0.2 V, -0.3 V and -0.4 V
RH	50 %, 60 %, 70 %, 80 %, 90 %, 100 %, 110 % and 120 %
Reactant gases	H_2/H_2 with flow rates of 0.75/0.75 SLPM respectively
Cell temperature	80 ˚C
Cell area	5 cm^2
Frequency range	500 kHz to 100 mHz
AC perturbation amplitude	10 mV
Recording rate	6 points per decade, 36 points total
Outlet Pressure	150 kPa

2.3.6 Cyclic voltammetry

Cyclic voltammetry (CV) is perhaps the most widely used electrochemical technique and is frequently applied for the initial characterization of a redox system. CV provides quantification

of redox potentials of the electroactive species and convenient evaluation of the effect of different materials, morphology, or operating environments upon the redox process.

CV can provide comprehensive information regarding:

1. electrochemical surface area (ECSA) of the cell

2. absorbed ion species on the catalyst surface

3. electrochemical characterizations of crystal lattice structure of catalyst material

4. catalyst and support material degradation

In PEFC research, due to two electrodes set up configuration, the reference electrode (RE) and counter electrode (CE) are the same. Normally CV uses hydrogen at counter electrode and nitrogen at working electrode under constant temperature, flows and RH to eliminate background noise from hydrogen adsorption in addition to the hydrogen evolution/oxidation reaction.

A typical CV in acid solution using Pt as catalyst material is shown in **Figure 2.5**:

For anodic scan:

- At low voltage (0.05-0.4 V), hydrogen oxidation occurs:

$$Pt - H + H_2O \rightarrow Pt + H_3O^+ + e^- \qquad (1)$$
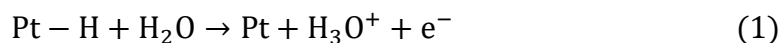
- At medium voltage (0.4-0.6 V), Pt oxidation occurs:

$$Pt + H_2O \rightarrow Pt - OH + H^+ + e^- \tag{2}$$
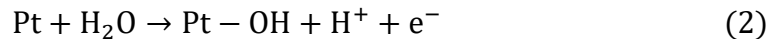
- At high voltage (0.65-1.05 V), Pt further oxidation occurs:

$$Pt - OH + H_2O \rightarrow Pt - O + H_3O^+ + e^- \tag{3}$$
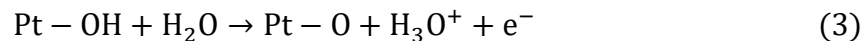
For cathodic scan:

- At high voltage (1.05-0.65 V), Pt oxide reduction occurs:

$$Pt - O + H_3O^+ + e^- \rightarrow Pt - OH + H_2O \tag{4}$$

- At medium voltage (0.65-0.4 V), Pt oxide further reduction occurs:

$$Pt - OH + H^+ + e^- \rightarrow Pt + H_2O \tag{5}$$
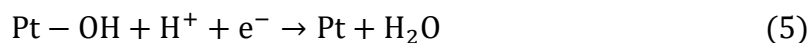
- At low voltage (0.4-0.05 V), Pt further oxidation occurs:

$$Pt + H_3O^+ + e^- \rightarrow Pt - H + H_2O \tag{6}$$
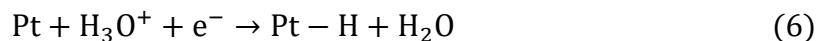
- At extreme low voltage (0-0.05 V), hydrogen evolution occurs:

$$2H_3O^+ + 2e^- \rightarrow 2H_2O + H_2 \qquad (7)$$
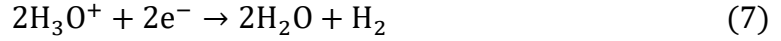
- At extreme high voltage (1.05-1.2 V), oxygen evolution occurs:

$$2H_2O \rightarrow O_2 + 4H^+ + 4e^- \qquad (8)$$
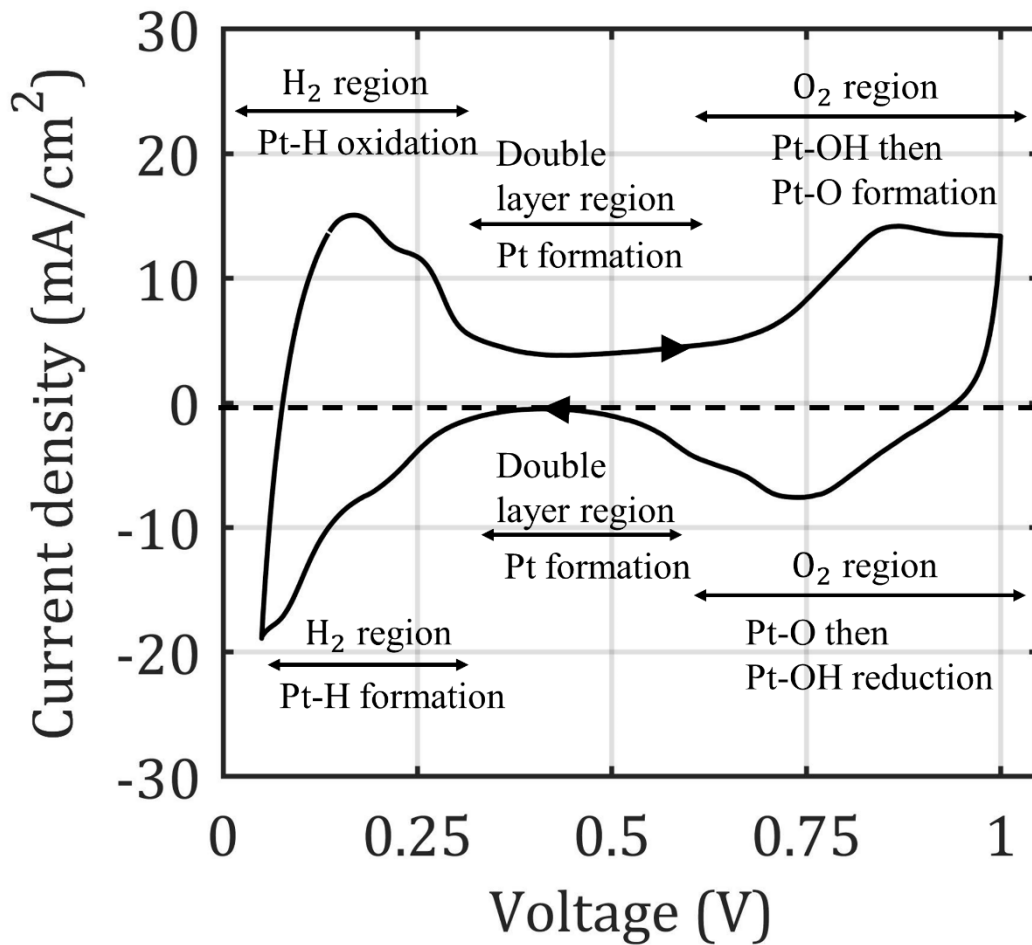
Figure 2.5 Cyclic voltammetry for PEFC using Pt/C catalyst, where various regions are identified for redox-activity of Pt.

In this work, the cell was humidified by purging 0.5/0.5 SLPM pure N_2 without back pressure at 60 °C and 100% RH for 1 hour. A cathode surface cleaning step was performed by conducting a

repeated cyclic voltammetry (CV) under 0.2/0.3 SLPM H_2/N_2 with a swap range from 0.05 V to 1.05 V at 200 mV/s scan rate for 30 cycles. Subsequently, CVs measurements with 20 mV/s, 40 mV/s, and 100 mV/s with the same voltage range and gas flow rates were conducted. Specifications are collected in Table 8.

Table 8. Cyclic voltammetry testing protocol

Cycle	Triangular wave between 0.05 V and 1.05 V. Scan rate of 20 mV s^{-1}, 40 mV s^{-1}, 100 mV s^{-1}
Total number of cycles	10
Reactant gases	H_2/N_2 with flow rates of 0.2/0.3 SLPM respectively
Cell temperature	80 °C
Gas inlet temperature	80 °C
Relative humidity	100 %
Outlet Pressure	Atmospheric

2.3.7 CO displacement and CO stripping methods

In PEFC, anion especially SO_3^- located at the end of the side chains in ionomer leads to a loss of Pt activity [47,51]. CO displacement and CO stripping method is the most effective way to quantify the ion species absorbed on the catalyst surface. Feliu and co-workers [52–55] first developed the technique of CO displacement/CO stripping to quantify anion adsorption within electrolyte at the Pt surface. Subbaraman et al. [44] extended the method to study the Nafion SO_3^- adsorption using a three-electrode setup in liquid electrolyte. Garrick et al. [56] was the first

31

study to use CO displacement study in both rotating disk electrode (RDE) and membrane electrode assembly (MEA) setups.

The testing protocol involves: after 60 mins N_2/N_2 purge with flow rates of 0.5/0.5 SLPM respectively (RH saturation process), prior to CO displacement, a surface cleaning CV step with 200 mV/s scan rate repeated 20 cycles using 1/1 SLPM of 5% H_2 on anode and pure N_2 on cathode was performed. After that, the cell was held at 0.4 V for 7 min without any changes of gas flows and flow rates. After first 2 min N_2 purge on cathode, the gas was instantly switched to 2% CO. After that, the cell was held under the same constant voltage with 2% CO gas purging continued for the rest 5 min to establish another constant current baseline. Since the residual air gas within the system, the first CO displacement measurement was interrupted by ORR of the air. Hence the result of first measurement was discarded. After that, CO displacement experiments were conducted from 0.1 V to 0.4 V in increments of 0.1 V. After CO displacement, 1 SLPM pure N_2 was purged at cathode side for 20 min to remove the residual CO gas in the cell. Subsequently, a CV under 1/1 SLPM 5% H_2 and N_2 with a potential sweep range from 0.05 V to 1.05 V at 100 mV/s scan rate using was performed and repeated 5 times. Testing protocol is summarized as the following **Figure 2.6**:

RH saturation, 0.5/0.5 SLPM N_2/N_2 purge for 60 mins

CV cleaning, 1/1 SLPM 5% H_2/N_2, 200 mV/s, 20 cycles

CO displacement, 1/1 SLPM 5% H_2/N_2 or 2% CO,
0.1, 0.2,0.3,0.4 V constant voltage hold for 7 mins
(2 mins in N_2 and 5 mins in 2% CO)

Residual CO gas removal, 1/1 SLPM 5% H_2/N_2 for 20 mins

CO stripping, 1/1 SLPM 5% H_2/N_2, 40 mV/s, 5 cycles
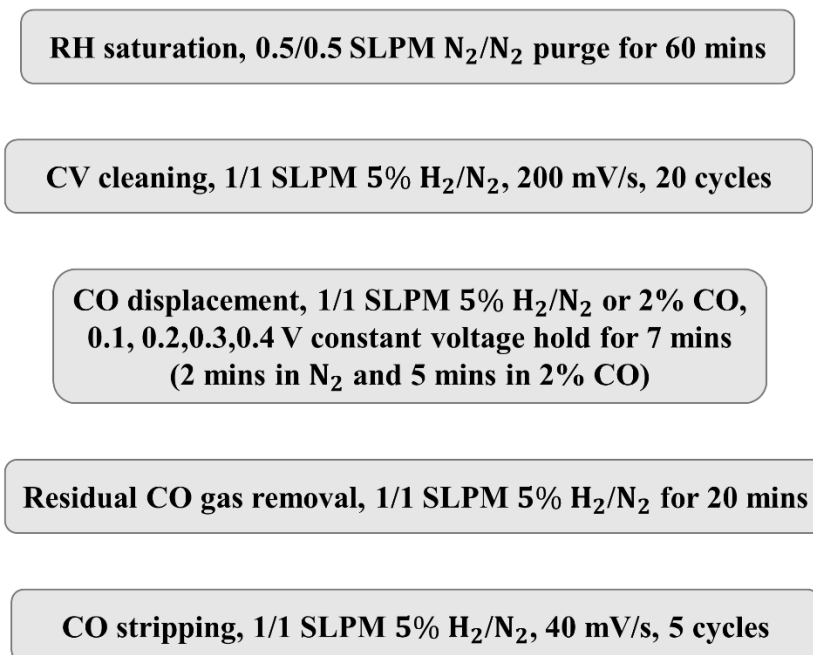
Figure 2.6 Flow chart of CO displacement and CO stripping testing protocol

2.3.8 Electrochemical impedance spectroscopy (EIS) method

In PEFC, due to ohmic loss and nonohmic loss such as mass transport loss, kinetic loss at the electrode, and ion species adsorption, etc, cell voltage losses according to current generation. EIS method is an effective way to study the nonohmic contribution since those contributions normally have frequency-dependent response times which make them ideal for study using alternating current (AC) techniques.

Nyquist plot is the most representative plot when study EIS, which consists of imaginary component of the impedance against the real component for any frequency. In this work, to study ion transport property, especially ionic conductivity, H_2/N_2 EIS was used since it ignored the faradic reactions, which will be discussed in the later section. Using H_2/N_2 EIS, Nyquist plot can

33

be easily to read and understand (**Figure 2.7**). At high frequency, H^+ vibrates and measured impedance is the intercept on the real impedance axis and considered as high frequency resistance, which includes all the ohmic resistances in the system (i.e., the contact losses, the ionic losses in the electrolyte, and electronic resistances). With frequency decreases, H^+ starts to be transported in the electrolyte, and it shows both resistive and capacitive effects. Then a 45° segment is shown in the Nyquist plot. At low frequency, H^+ charges double layer and it shows fully capacitive behavior in the Nyquist plot, which is a straight line with keeping increasing imaginary impedance to the infinite. Sometimes the straight line is not vertical in the Nyquist plot due to the side reactions such as ion species adsorption and cross-overed H_2 oxidation.
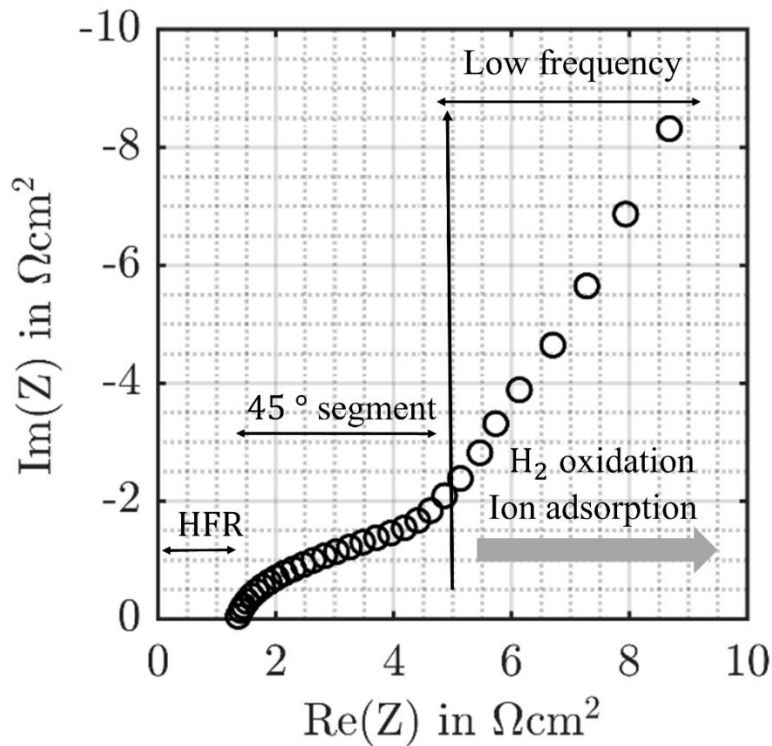
Figure 2.7 H_2/N_2 electrochemical impedance spectroscopy of PEFC

In this work, prior to EIS measurement, cell RH was allowed to equilibrate for 60 min by only purging gases at open circuit voltage (OCV). For the chosen potential range (>0.2 V), the H_2 crossover currents will not influence the AC impedance signal significantly. [57] In other works, potentials were set to 0.45–0.5 V to collect EIS data. [58,59] Here, for ionic conductivity study, after RH equilibration, the impedance was measured at 0.2 V using 0.2/0.3 SLPM of pure H_2 on anode and pure N_2 on cathode without back pressure at 80 °C and 100 % RH. After 5 min hold at the selected voltage, an AC perturbation was applied to perform EIS. The AC perturbation potential with an amplitude of 10 mV was applied over a frequency range from 500 kHz to 100 mHz. Recording rate was set at 8 points per decade. AC impedance measurements at each RH were repeated three times to ensure reproducibility. To study double layer capacitance, 0.4 V was chosen as DC voltage hold since H^+ oxidation was eliminated, and the chosen voltage was in the range of double layer region. For the testing specifications, they are collected in Table 9.

Table 9. H_2/N_2 EIS testing protocol

Frequency range	500 kHz to 100 mHz
DC voltage hold	0.2 V for ionic conductivity study 0.45 V for double layer capacitance study
AC perturbation amplitude	10 mV
Recording rate	8 points per decade
Reactant gases	H_2/N_2 with flow rates of 0.2/0.3 SLPM respectively
Cell temperature	80 °C
Gas inlet temperature	80 °C

Relative humidity	100 %
Outlet Pressure	Atmospheric

2.3.9 Electrochemical characterizations during carbon corrosion AST

For Pt/HSAC, above electrochemical characterizations were measured for beginning of life (BOL), after 100 AST cycles, after 500 AST cycles and after 1000 AST cycles which was considered as end of life (EOL) of the cell. For Pt/graphitized carbon, due to the lower carbon corrosion rate [60], more AST cycles were performed. Electrochemical characterizations were measured for beginning of life (BOL), after 100 AST cycles, after 500 AST cycles, after 1000 AST cycles, after 2500 AST cycles, after 5000 AST cycles and after 10000 AST cycles which was considered as EOL of the cell.

2.4 Ex-situ testing protocols

2.4.1 Scanning electron microscope (SEM) sample preparation and imaging

Cross-sectional MEAs samples using HSAC and graphitized carbon supports were embedded in epoxy resin and imaged with a FEI Magellan 400 scanning electron microscope detector operating at 3.00 kV accelerating voltage. SEM measurements were repeated for BOL and EOL for each carbon support type, and catalyst layer thicknesses were measured after SEM measurements.

2.4.2   Scanning transmission electron microscopy (STEM)

At BOL, a JEOL Grand ARM300F microscope, equipped with two spherical aberration correctors, was used to perform the aberration-corrected scanning transmission electron microscopy (AC-STEM) characterization for both Pt/HSAC and Pt/graphitized carbon MEAs. The TEM imaging was performed at 300 kV.

2.4.3   Transmission electron microscopy (TEM)

After cycling, the catalyst layers were scraped from the MEA to make powders. The powders were then dispersed in ethanol by sonication. A few drops of the suspension were deposited onto holey carbon-coated copper grids. The images were obtained using a JEOL JEM-2800 microscope at 200 kV.

2.4.4   X-ray fluorescence (XRF)

XRF was performed on a Horiba XGT9000 with a 10 µm capillary and 50 keV energy for the X-rays. The area that was investigated was 3x3mm, with a resolution of 12 µm per pixel. Information about the loading was obtained through the building of a calibration curve in the XRF software using Pt standards of different loadings (Micromatter Technologies inc.) between 20 and 1000 µm/cm^2. The scale bars of XRF maps were built by attributing the average loading calculated by the instrument from to the average of the distribution of the intensity in the grey-scale image (Imagej, histogram function).

2.4.5 X-ray photoelectron spectroscopy (XPS)

XPS was performed on a Kratos AXIS Supra spectrometer with a monochromatic Al Kα source. CasaXPS software was used to analyze the data. The fitting was based on our previous calculations and publications [61,62]. For the C1s, a linear substation was used. The graphitic C spectra were fitted with an asymmetric modified 20% Gaussian/80% Lorentzian line shape, and other spectra were fitted with a 70% Gaussian/30% Lorentzian line shape. For the Pt 4f, a Shirley substation was used, and all spectra were fitted with an asymmetric modified 70% Gaussian/30% Lorentzian line shape. Atomic concentrations of different elements were calculated based on their intensities and relative sensitivity factors.

2.5 Calculation methods

2.5.1 Double layer capacity (C_{dl})

Double layer capacity (C_{dl}) is considered as the capacity summation of the four different interfaces within the catalyst layer, which is shown in **Figure 2.8**: 1). Pt/ionomer, 2). Pt/water, 3). Carbon/ionomer and 4). Carbon/water [59]. Investigating in C_{dl} change during the carbon corrosion AST provides more insights on interfacial properties change between solid/ionic phase materials. In carbon corrosion study, C_{dl} was calculated using the following equation:

$$I = C_{dl} \times \frac{dV}{dt} \tag{9}$$

Where I denote the upper/lower current difference in double layer region (0.4-0.5 V) from CV measurements. $\frac{dV}{dt}$ represents the voltage sweep rate of CV measurement, here it is 100 mV/s.

In novel ionomer and sulfonic acid group study, double layer capacity was calculated from the collected EIS data according to Iden and Ohma's study [59], which utilized the relationship among double layer capacity, frequency and imaginary impedance:

$$-\frac{1}{\omega \times Z_{img}} = \frac{1}{\omega^2 \times R_{ct}^2 \times C_{dl}} + C_{dl} \qquad (10)$$

where ω is the angular frequency, Z_{img} is imaginary part of impedance, R_{ct} is corresponding to the charge transfer resistance, which is a consequence of hydrogen crossover through the membrane resulting in parasitic reactions and C_{dl} is a double layer capacitance. In this paper, $-\omega^{-1} \times Z_{img}^{-1}$ was plotted as a function of ω^{-2}, and C_{dl} was then obtained by extrapolating to $\omega^{-2} = 0$. Iden et al.'s calculation are shown below as **Figure 2.8**:
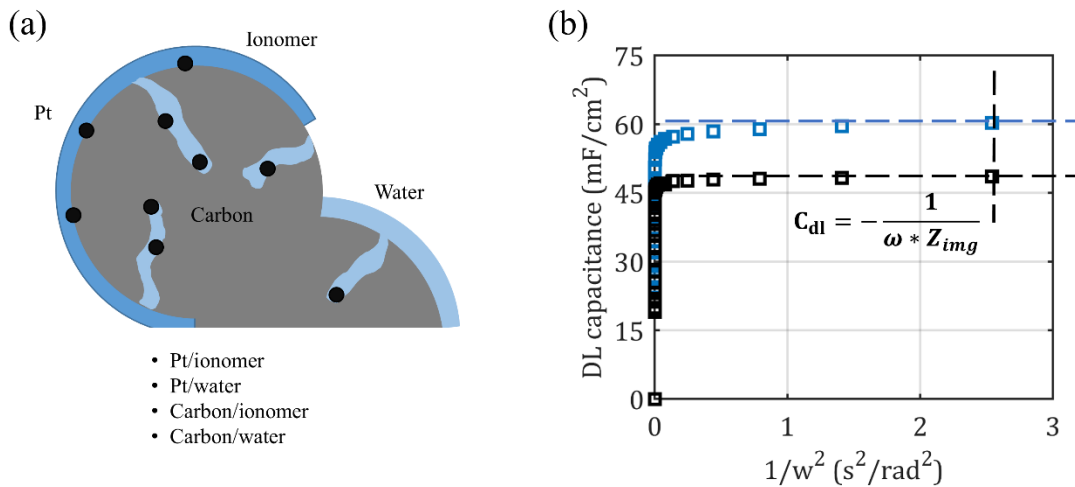
Figure 2.8 a) Four different interfaces with the catalyst layer and b) example calcualtion of double layer capacitance

2.5.2 Effective ionic conductivity

Effective ionic conductivity was derived by using a H_2/N_2 EIS fitting model according to Qi et al.'s work [63]. The model is based on Obermaier et al.'s model [58] which modeled the equivalent circuit of catalyst layer based on transmission line model. In this work, catalyst layer ionic conductivity was derived by inputting the frequency, cell active area, catalyst layer thickness, imaginary impedance and real impedance etc. into the fitting model. Fitting model will be discussed in next chapter.

2.5.3 Tortuosity factor

In chapter 3 and chapter 4, ionic conductivity of catalyst layer was investigated. To study ionic conductivity, specially H^+ transport conductivity, averaged tortuosity of H^+ pathways is very valuable to study. Tortuosity factor is the ratio of the total length of the distance that species transport, L_{eff} over a geometric distance, L. Tortuosity, shown in **Figure 2.9** is defined as a square of tortuosity factor [64]:

$$\tau = \left(\frac{L_{eff}}{L}\right)^2 \tag{11}$$
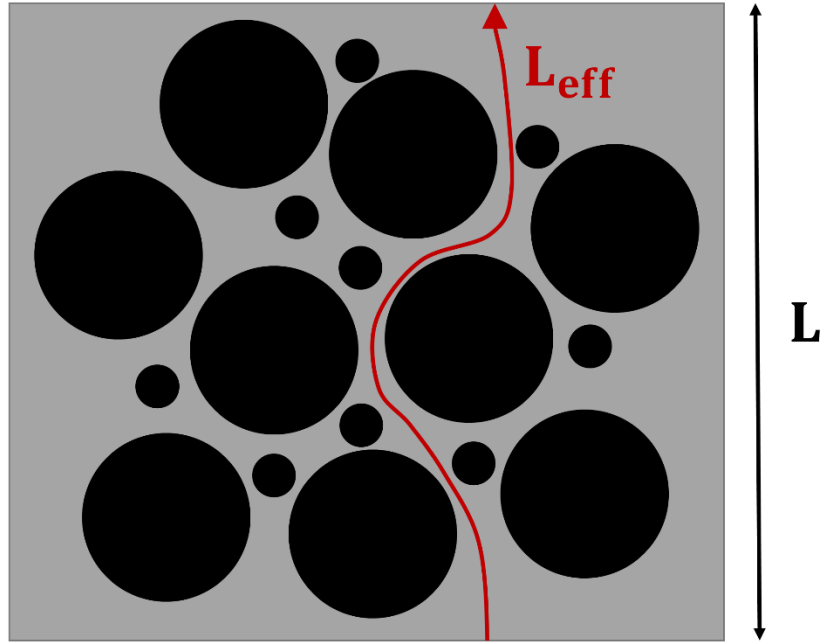
Figure 2.9 Tortuosity of ionic pathway in a porous media

Tortuosity factor can also be calculated as:

$$\tau = \left(\frac{\sigma_{mem} \times \epsilon_{ion}}{\sigma_{CL}}\right)^{0.5} \tag{12}$$

where σ_{mem} is bulk membrane or ionomer conductivity, ϵ_{ion} is ionomer volume fraction within the layer and σ_{CL} is effective proton conductivity obtained with either HP or AC experiments.

Ionomer volume fractions calculations at a range of relative humidity were reported previously by Liu et al. [65] in Appendix of their article. Here we show their final formula result for calculating ionomer volume fraction, for full derivation refer to their publication.

$$\epsilon_{ion} = \left(\frac{I}{C}\right)\frac{10}{f_t d_{I,dry}}\left(1 + \frac{M_w d_{I,dry}\lambda}{d_w EW}\right) \tag{13}$$

where I/C is ionomer to carbon ratio, f_t is 28 μm/(mg$_C$/cm^2). For I/C ratio < 3, $d_{I,dry} =$ 2 g/cm^3, which is density of dry ionomer; $d_w = 0.97$ g/cm^3, which is density of water; $M_w = 18$ g/mol, which is molecular weight of water; EW $= 825$ g/mol, which is equivalent weight of ionomer; λ is ionomer water content, which is a function of RH and is obtained from Ref. [66]

2.5.4 CO displacement charge

During CO displacement measurement, due to the strong absorbability of CO, it displaced the adsorbed ion species at the Pt surface, for example H^+ and SO_3^- group, which resulted in charge transfer and current flow. According to Eqn. (14) and Eqn. (15), positive current signal was recorded when constant potential which was lower than the potential of zero charge (PZC) of Pt was applied. Negative current signal was recorded when constant potential which was greater than PZC was applied. CO displacement charge was the integration of CO displacement peak in the Current-time plot **Figure 2.10a**.

$$Pt - Ca + CO \rightarrow Pt - CO + Ca^+ + e^- \tag{14}$$

$$Pt - An + CO + e^- \rightarrow Pt - CO + An^- \tag{15}$$
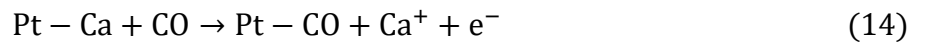
Where Pt-Ca is cation adsorbed on Pt surface and Pt-An is anion adsorbed on Pt surface. Here at 0.1 V H^+ is absorbed cation and at 0.4 V SO_3^- group of ionomer is absorbed anion species, which follows convention of Garrick et al. [56].

2.5.5 CO stripping charge

CO stripping charge was calculated by integrating the CO stripping peak from CO stripping measurement then divided by the scan rate of 100 mV/s **Figure 2.10b**. CO stripping contained multiple steps for example the formations of OH_{ads} and $COOH_{ads}$ which followed Langmuir-Hinshelwood mechanism [67].

$$H_2O + \ast \leftrightarrow OH_{ads} + H^+ + e^- \tag{16}$$

$$CO_{ads} + OH_{ads} \rightarrow COOH_{ads} \tag{17}$$

$$COOH_{ads} \rightarrow CO_2 + H^+ + e^- + \ast \tag{18}$$
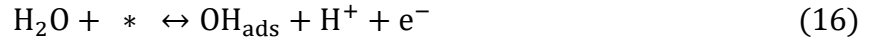
Where $\ast$ denotes the free surface site.
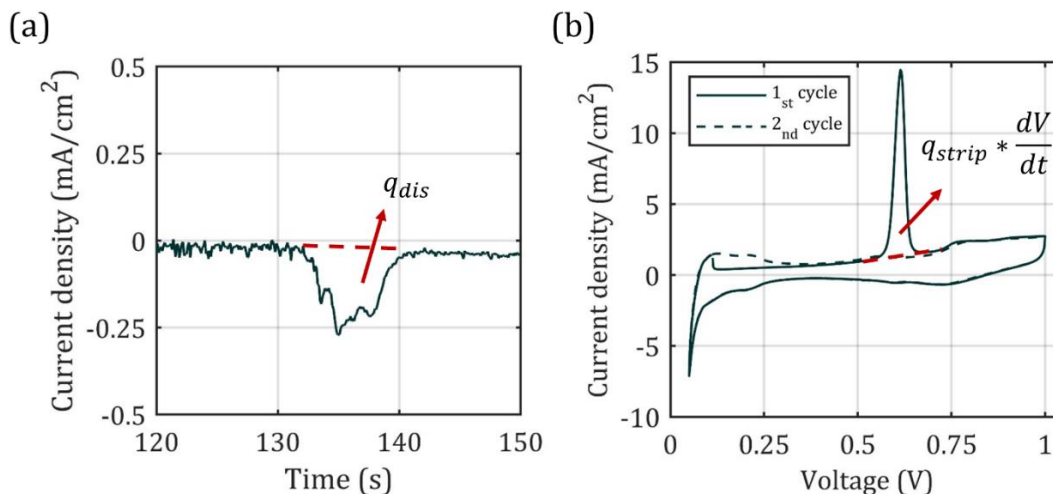
Figure 2.10 a) Integration of CO displacement charge, b) integration of CO stripping charge.

2.5.6 Electrochemical surface area (ECSA)

Electrochemical surface area (ECSA) is considered as loading normalized efficiency. ECSA is the most common parameter when compare loading normalized efficiency between two electrodes. It can also show the electrode degradation during catalyst and support AST.

To calculate ECSA of an electrode, one assumption must be achieved: each Pt site can only be absorbed by one H^+. In this work, ECSA was calculated and averaged from the H_2 under potential deposition (H_{upd}) region of CV and CO stripping peak integration from CO stripping (**Figure 2.11**), respectively:

$$ECSA_{H_{upd}} \ (m^2/g) = \frac{Q_{H_{upd}}(C)}{210 \ \frac{\mu C}{cm^2} \times Area \ (cm^2) \times L_{pt} \ (\frac{mg}{cm^2})} \times 10^5 \qquad (19)$$

44

$$ECSA_{CO} \ (m^2/g) = \frac{Q_{CO}(C)}{420 \ \frac{\mu C}{cm^2} \times Area \ (cm^2) \times L_{pt}(\frac{mg}{cm^2})} \times 10^5 \qquad (20)$$

where $Q_{H_{upd}}$ (C) is charge integration over the H_{upd} region and Area denotes the cell active area

(cm^2). L_{pt} denotes the Pt loading (mg/cm^2). 210 and 420 $\frac{\mu C}{cm^2}$ are the charges per H_{upd}

monolayer and CO monolayer, respectively [68]. In the ECSA calculations, a conversion factor

of 10^5 is required. ECSA calculations regarding CV method and CO stripping method are shown

below:

(a)

(b)
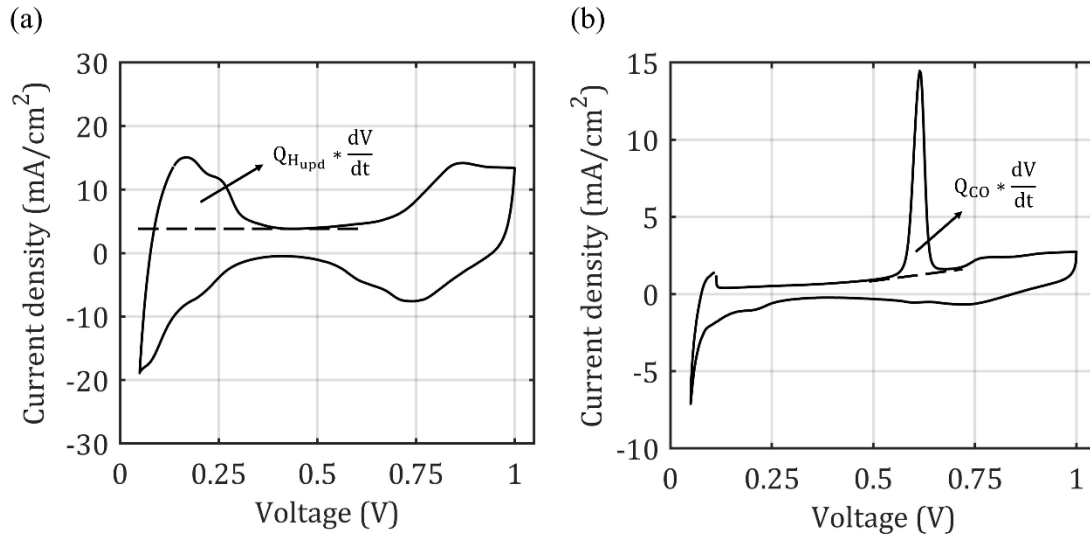
Figure 2.11 a) Integration of Hydrogen under potential deposition, b) integration of CO stripping charge

2.5.7 SO_3^--group coverage

SO_3^- group coverage was calculated using the following equation [56]:

$$\theta_{SO_3^-} = \frac{2 \times q_{dis}}{q_{strip}} \times 100\% \tag{21}$$

where q_{dis} is the CO displacement charge, q_{strip} denotes the CO stripping charge. There is a multiplier 2 in the numerator since CO requires two electrons to oxidize CO to CO_2. The coverage is an averaged and the SO_3^- group coverage corresponds to an average amount of Pt atoms that are covered by SO_3^- groups for one Pt particle, as shown in **Figure 2.12**.
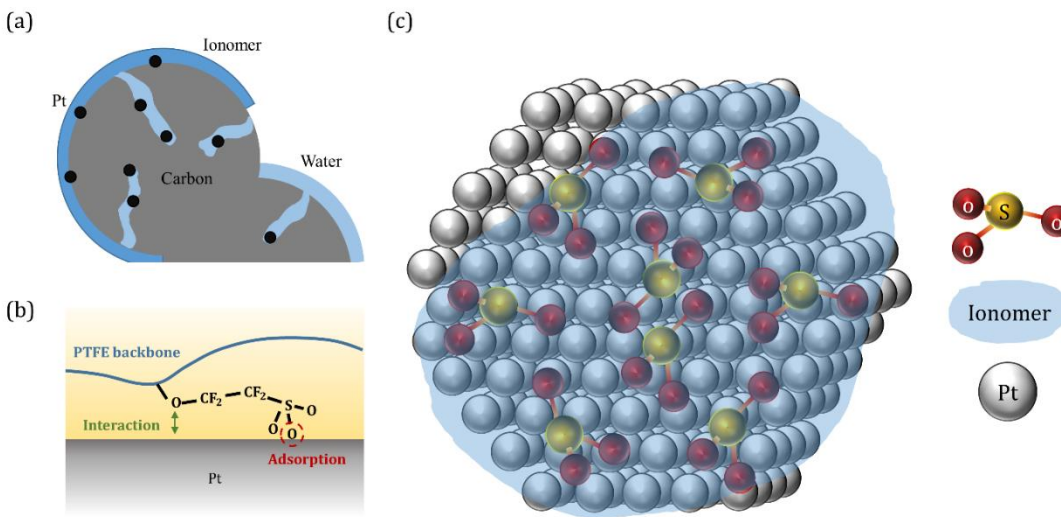
Figure 2.12 a) A schematic of all the interfaces present for Pt/C interfacing water or/and ionomer, b) a schematic of Pt/ionomer interface showing the SO_3^- adsorbing on the Pt surface adopted from Kodama et al. [47], c) a schematic of averaged SO_3^- group coverage on one Pt particle

2.5.8 Ionomer on Pt surface coverage

The relative ionomer and water coverages on Pt and carbon support were calculated using the method developed by Iden et al. [59]:

$$\theta_{Pt/i} = \frac{C_{Pt/i}}{C_{Pt/w} + C_{,Pt/i}} \tag{22}$$

$$\theta_{Pt/w} = \frac{C_{Pt/w}}{C_{Pt/w} + C_{Pt/i}} \tag{23}$$

$$\theta_{C/w} = \frac{C_{C/i}}{C_{C/w} + C_{C/i}} \tag{24}$$

$$\theta_{C/w} = \frac{C_{dl,C/w}}{C_{dl,C/w} + C_{dl,C/i}} \tag{25}$$

where, $C_{Pt/i}$, $C_{Pt/w}$, $C_{C/i}$ and $C_{C/w}$ are double layer capacitances between Pt/ionomer, Pt/water, carbon/ionomer, and carbon/water, respectively. The coverages were calculated from the ratio of capacities at different interfaces. These are relative coverages, where water and ionomer coverage sum up to 100 %.

C_{dl} consists of four different interfacial capacitances: (i) Pt/ionomer ($C_{Pt/i}$); (ii) Pt/water ($C_{Pt/w}$); (iii) carbon/ ionomer ($C_{C/i}$); and (iv) carbon/water ($C_{C/w}$). All of them contribute to C_{dl} under a wet condition without the CO treatment.

To quantify each interfacial capacity. EIS measurements at four different operation conditions are required:

- EIS measurement at 100% RH without CO treatment:

$$C_{dl,100\% \, RH, without \, CO} = C_{pt/i} + C_{pt/w} + C_{C/i} + C_{C/w} \qquad (26)$$

- EIS measurement at 100% RH with CO treatment:

$$C_{dl,100\% \, RH, with \, CO} = C_{C/i} + C_{C/w} \qquad (27)$$

- EIS measurement at 50% RH without CO treatment:

$$C_{dl,50\% \, RH, without \, CO} = C_{pt/i} + C_{C/i} \qquad (28)$$

- EIS measurement at 50% RH with CO treatment:

$$C_{dl,100\% \, RH, without \, CO} = C_{C/i} \qquad (29)$$

By doing subtractions, each interfacial capacitance can be derived. **Figure 2.13** shows an example of calculations of each interfacial capacitance.

The plot on the left shows DL capacitance (mF/cm²) versus 1/w² (s²/rad²). The diagram on the right shows a Carbon particle with Pt, Ionomer, and Water labeled.

Legend:
- □ 50% RH without CO
- ○ 50% RH with CO
- ◁ 100% RH without CO
- ▷ 100% RH with CO

- Pt/ionomer
- Pt/water
- Carbon/ionomer
- Carbon/water

100% RH without CO: $C_1 = C_{dl,Pt/w} + C_{dl,Pt/i} + C_{dl,C/w} + C_{dl,C/i}$

100% RH with CO: $C_2 = C_{dl,C/w} + C_{dl,C/i}$

50% RH without CO: $C_3 = C_{dl,Pt/i} + C_{dl,C/i}$

50% RH with CO: $C_4 = C_{dl,C/i}$

Figure 2.13 Example calculation of four different interfacial capacitances by applying EIS at 1) 100 % RH without CO treatment, 2) 100 % RH with CO treatment, 3) 25% RH without CO treatment, 4) 25 % RH with CO treatment

Chapter 3. Determining Proton Transport in Pseudo Catalyst Layers Using Hydrogen Pump DC and AC Techniques

3.1   Introduction

In this chapter, catalyst layer ionic conductivity is investigated. A promising alternative method has been previously reported, a so-called hydrogen pump (HP) method, where a pseudo CL (PCL) is sandwiched between two membranes in a standard PEFC setup [69,70]. Hydrogen oxidation reaction (HOR) occurs on anode, protons are transported through membrane, PCL and another membrane to recombine with electrons in hydrogen evolution reaction (HER) on the cathode. In Iden et al. [69] work a single PCL was used, where membrane and contact resistances were either directly measured without PCL or extrapolated from high frequency resistance (HFR). The disadvantage of this method is that Pt cannot be used in the sandwiched layer because hydrogen that crosses through the membrane will react and transport the current electrically. Furthermore, there may be local HOR and HER in the PCL that will also short the circuit, which will inhibit measurements of ionic conductivity. The exact mechanism needs to be explored with modeling study, but the experiments show that the PCL cannot have an electrocatalyst that is active towards HOR and HER.

In this work HP method was extended to PCLs with varied ionomer to carbon (I/C) ratios and present an alternative method for measuring proton conductivity within HP set-up. The EIS method, here referred as AC method is based on effective transport properties measurements within gas diffusion layers, reported by Kramer et al. [71] AC method to measure ionic conductivity in PCLs and compare it with the conventional HP method, here referred to as the DC method. The advantages and disadvantages of the AC method as compared to DC method are discussed in this study, as well. AC method has similar limitations to DC method, as at low frequencies that are of interest in this study AC essentially becomes a DC method. However, it presents an advantage of requiring less experiments compared to a DC method. We apply the methods to study ionic conductivity of PCLs with three I/C ratios for 50 – 120 % RH. Our approach is to stack PCLs and to extrapolate membrane and contact resistances from the plot of overall resistance vs. PCLs thickness. Using the AC and DC techniques we report effective ionic conductivity and also ionomer tortuosity for the three PCLs.

According to chapter 2, which introduces testing protocol of each measurement. The testing series is shown as following Table 10:

Table 10. Testing series used in pseudo catalyst layer ionic conductivity study using H_2 pump set up

Experiment	Conditions
Conditioning	H_2/ N_2 - 0.25 slpm /0.25 slpm, No backpressure, 1 hour at 60°C , 100% RH

Preliminary polarization curve	H$_2$/Air – 0.2 slpm/ 0.5 slpm, 80°C, corresponding RH
	Backpressure - 100 kPa/ 100 kPa
	1 mV/s sweep rate until V=0.1 V from OCV
Hydrogen Pump	H$_2$/ H$_2$ – 0.75 slpm/ 0.75 slpm
	Backpressure - 100 kPa/ 100 kPa
	0 V to -0.4 V, 10 minute hold, EIS at 10 mV ac impedance from 500 kHz to 100 mHz at each voltage step, repeated 3 times
Hydrogen cross over correction	H$_2$/N$_2$ – 0.2 slpm/ 0.5 slpm, 80°C, corresponding RH
	Backpressure - 100 kPa/ 100 kPa
	2 mV/s sweep rate until V=0.8 V from OCV
Ending polarization curve	H$_2$/Air – 0.2 slpm/ 0.5 slpm, 80°C, corresponding RH
	Backpressure - 100 kPa/ 100 kPa
	1 mV/s sweep rate until V=0.1 V from OCV

3.2 Cell equivalent circuits and Modeling fitting

3.2.1 DC HP

Figure 3.1a shows a schematic of the HP set-up, where HOR occurs on the anode side and HER on the cathode side. The potential difference between cathode and anode is the driving force for proton transport. The set-up can be approximated as several resistors in series. These include membrane resistance, R_{mem}, contact resistances on anode and cathode, R_{cnt} and resistance of the PCLs, R_{PCL}. **Figure 3.1b** shows an equivalent circuit with these three resistances in series, where the total resistance in this circuit, R_{TOT} is the summation of all the resistances:

$$R_{TOT} = 2R_{cnt} + 2R_{mem} + R_{PCL} \quad [\Omega] \tag{30}$$

Figure 3.1b also shows an equivalent circuit, when there are no PCLs present in the set-up, where the total resistance is R_1 and can be expressed as:

$$R_1 = 2(R_{mem} + R_{cnt}) \quad [\Omega] \tag{31}$$

The effective resistance of the PCLs can be calculated as the difference between R_{TOT} and R_1. **Figure 3.1c** shows the plot of resistance as a function of the PCL thickness. The thickness of the layers can be increased by increasing the number of PCLs. The intercept where the thickness of the PCLs is 0 should correspond to R_1, or the case with no PCLs. The slope of the plot is:

$$\text{Slope} = \frac{(R_{TOT} - R_1)}{t_{carb}} \quad [\Omega/cm] \tag{32}$$

Where the effective conductivity of the PCLs can be calculated as:

$$\sigma_{Eff} = \frac{t_{carb}}{A \times (R_{TOT} - R_1)} = \frac{1}{A \times \text{Slope}} \quad [S/cm] \tag{33}$$
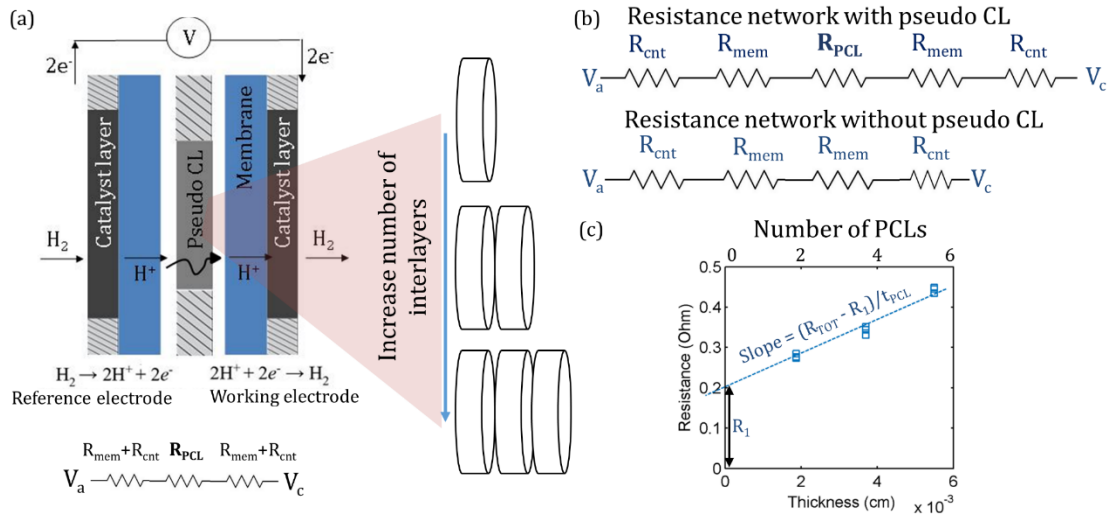
Figure 3.1 a) Schematic of the HP set-up, b) Equivalent circuit for the DC measurement, c) Resistances vs number of layers and interpretation of slope and intercept, R1.

3.2.1 AC HP

After each potential hold for HP DC measurements, the EIS study was performed at the same potential hold. At high frequencies (>20 kHz), the penetration depth of protons into the PCL is very small (10s of nm) and the impedance is only the resistance of proton conduction in the two

54

membranes and electric contact resistances. In this case, the internal double layer (DL) capacitors at the interface between ionomer and carbon supports are virtually shorted and the impedance only contains the real portion as shown in **Figure 3.2b**. As the frequency decreases, protons start to transport into the PCL. The DL capacitance leads to the increase of the imaginary portion of the impedance. Meanwhile, as the proton penetration depth increases, the real portion of the impedance is also increasing. Assuming an ideal behavior of the internal DL capacitors, it first forms a 45° degree line in the Nyquist plot as shown in **Figure 3.2b**. With the further decrease of the frequency, it forms a suppressed semi-circle. When the frequency approaches zero the protons conduct through the whole PCL. At this low frequency (< 1 Hz), the DL capacitors become open circuit and the transport is purely resistive in the ionomer phase. As a result, the low-frequency end of the impedance spectra lies on the real axis in the Nyquist plot as shown in **Figure 3.2b**. The distance between the two intercepts on real axis is the effective resistance of proton conduction in the PCL [71]. In the real experiments, the capacitive behavior of the DL capacitors can be non-ideal due to the porous and heterogeneous nature of the material. A constant phase element (CPE) is applied to study this non-ideal capacitive impedance as shown in **Figure 3.2c** [72]. The CPE is in parallel with the ion conduction resistor and its impedance is calculated as [72]:

$$Z_{CPE} = \frac{1}{T \cdot (\omega j)^{\phi}} \tag{34}$$

where T is the distributed capacitive term, ω is the angular frequency of the impedance signal and $\phi \leq 1$ accounts for the non-ideal behavior of the capacitance. When $\phi = 1$, T becomes the DL capacitance C and the impedance becomes the ideal capacitor impedance $\frac{1}{\omega C j}$. At high I/C

55

ratios and high RHs, the ionomer phase is connected through the entire PCL and the impedance spectra is a single semi-circle in the mid-frequency range (**Figure 3.2b**). The Nyquist plot fitting for PCLs with I/C 1 and 1.4 for RH 60 % and higher was done with a single CPE with a resistor connected in parallel. However, at low I/C ratios (here at I/C = 0.6), especially at low RHs, the ionomer phase can become disconnected and the impedance of the PCL is separated into two parts. Each part consists of a resistor and a CPE as shown in **Figure 3.2c**. In this case, the impedance spectra become two semi-circles in the mid-frequency range (an example is **Figure 3.16** Nyquist plot for 4 PCLs of I/C = 0.6 and a range of RH from 50 to 120 %. The vertical lines show calculated frequencies for a current penetration dept of 32 µm.). The total impedance is calculated as:

$$Z_{total} = R_{mem} + \frac{1}{\frac{1}{R_a} + \frac{1}{Z_a}} + \frac{1}{\frac{1}{R_b} + \frac{1}{Z_b}} + R_{else} \tag{35}$$

where R_{mem} is the resistance of the two membranes and R_{else} accounts for all of the other resistances, including the contact resistances. The two resistances, R_a and R_b, are the most important parameters to be fitted as they determine the distance between the two intercepts on the real axis, which is inversely proportional to the effective ionic conductivity of the PCL [71], where similar to HP DC method:

$$\sigma_{Eff} = \frac{t_{carb}}{R_{eff}} \quad [S/cm] \tag{36}$$

56
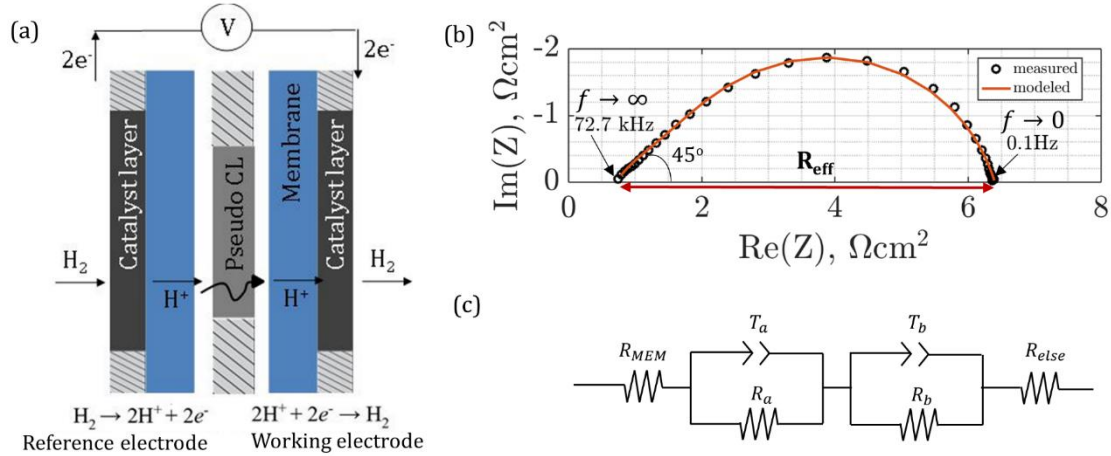
Figure 3.2 a) Schematic of the HP set-up, b) fitted AC data and physical interpretation, c) equivalent circuit.

3.3 HP result

3.3.1 DC HP result

Figure 3.3 shows HP polarization curves when no PCLs are present (only two stacked membranes) and when 2, 4, 6 and 10 layers are stacked between two membranes. In a potential regime from 0 to -0.2 V for most of the polarization curves, voltage shows linear dependency on current density, indicating ohmic regime. From -0.2 and sometimes from -0.3 to -0.4 V some polarization curves shown downward sloping, especially at RH above 100 %, this might be due to hydrogen transport limitations due to local flooding. As relative humidity increased from 0 to 120 % current densities increase too, due to higher ionic conductivity of the PCLs. Furthermore, for two Nafion layers with no PCLs (**Figure 3.3a**) the polarization curves do not change beyond RH of 120 %, as at this RH liquid water is already present and increasing further RH will just increase water content in the cell. The same polarization curves are seen for the RH range of 120 -150 %. Thus, we chose to set 120 % RH as a maximum RH for the measurements with PCLs.

As number of PCLs stacked between two membranes increases the current density decreases at a given potential and RH. For example, for no PCLs, the cell with two Nafion membranes can achieve 1000 mA/cm^2 at 120 % RH and -0.4 V, whereas the cell with 2 layers achieves 750 mA/cm^2 and the cell with 10 layers produces less than 250 mA/cm^2. Polarization curves were fit with linear trends in the potential region from 0 to -0.3 V, however if the linear fit shows R^2 values below 0.9 only the range from 0 to -0.2 V was selected for linear fitting. The deviation of R^2 below 0.9 was mostly happening with polarization curves at 100 % and higher RH.
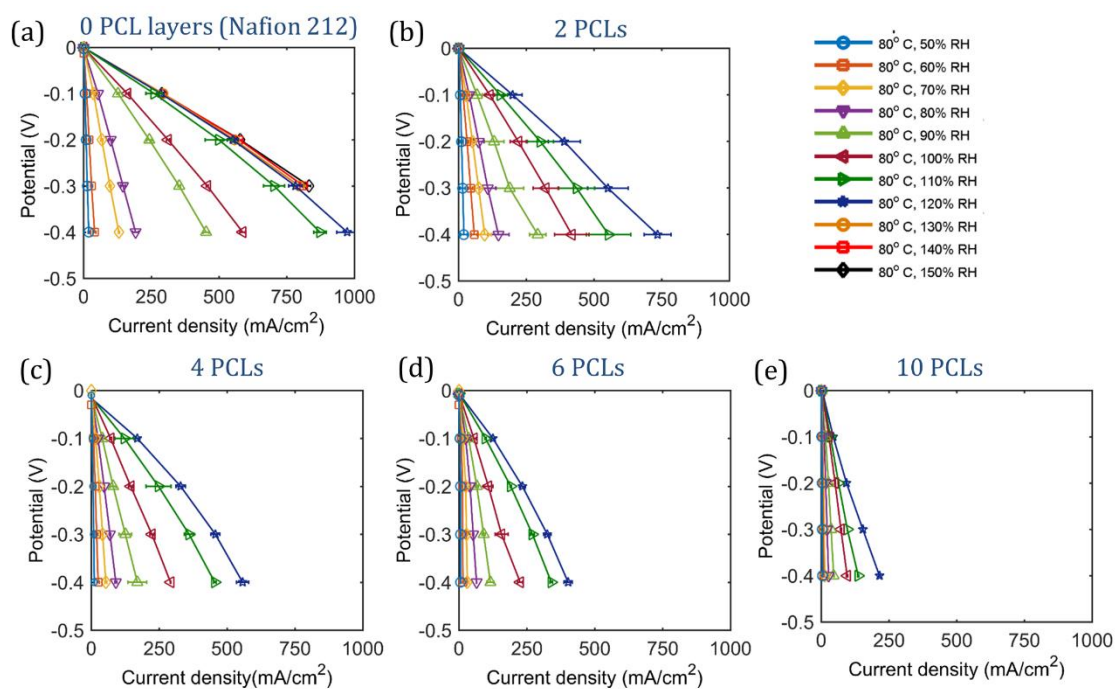
Figure 3.3 Polarization curves of HP experiments for PCL PFSA I/C 1.0 for stacks with 2, 4 and 6 carbon ionomer interlayers at various RH% and 80 °C and 100 kPa backpressure. The PCLs consist of PFSA 825 EW I/C = 1 and Vulcan XC-72.

3.3.2 System total resistance, contact resistance and membrane resistance

Figure 3.5a and **b** show the slopes of the fits from as functions of PCL thicknesses for low and high RH ranges, respectively. Membrane resistance is also shown for the case when PCL thickness is 0. Table 11 shows the measured individual and hot-pressed PCL thicknesses. These measurements were used for x-axis of **Figure 3.5a** and **b**. As already discussed in **Figure 3.2** the slope of the resistance vs. carbon layer thickness is needed to calculate effective conductivity, whereas the y-intercept when x = 0 corresponds to membrane and contact resistances. When using the data set for 2, 4, 6 and 10 layers we observe that linear fit will result in negative y-axis intercept, which is not physical, as intercept R_1 cannot be negative. One can clearly observe that 10 layer (PCL thickness 90 µm) measurements are not aligned with the rest of the thicknesses onto a straight line. After eliminating 10 PCL measurements from analysis, all fits produce positive y-intercept. Higher resistance for 10 PCLs is to be possibly due to accumulated contact resistances between the layers that did not scale linearly. These contact resistances are most likely due to misaligned ionomer domains, especially at low RH, when ionomer swelling is minimal.

Table 11. Averaged thickness of PCLs used in hydrogen pump study

Number of pseudo CLs	1 layer	2 layer	4 layer	6 layer	10 layer
Mean (µm)	9.29	18.17	37.50	56.67	92.67
Std. Dev. (µm)	0.136	2.03	1.12	1.97	0.94

Figure 3.5c shows the contact and membrane resistances, which is R_1 value as a function of RH. The plot compares three measurements: 1) direct measurements from HP experiment with two Nafion membranes and no PCLs, 2) extrapolated values from y-intercept at 0 PCL thickness from linear fits of **Figure 3.5a** and **b**) values calculated as HFRs. HP membrane and HP extrapolated values should in theory produce the same results as both rely on DC measurements, as shown from the circuits drawn in **Figure 3.4** shows relative difference between the two DC R_1 measurements. Relative difference of effective conductivity between DC and AC methods was calculated using the following:

$$Relative\ Difference = \frac{|\sigma_{DC} - \sigma_{AC}|}{\sigma_{DC}} \times 100\ (\%) \tag{37}$$
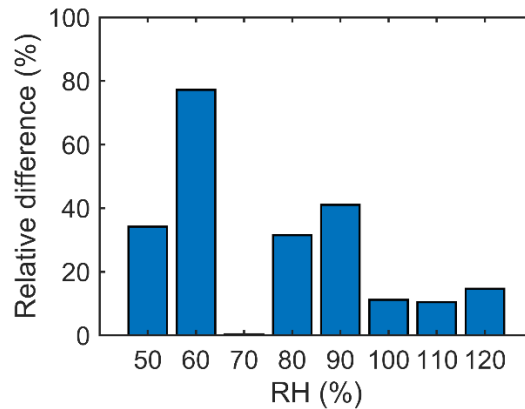
Figure 3.4 Relative difference between contact and membrane resistances measured with two membranes and extrapolated as R1 value from hydrogen pump pseudo CLs thicknesses study.

At 70 % RH and above the two measurements agree well, where the values at 70, 100, 120 % RH are less than 18 % apart. Largest differences are observed at 50 and 60 % RH. One possibility is that lower HP extrapolated values are due to ability of PCLs to retain water in

micro and meso-pores thus locally increasing RH and lowering contact and membrane resistances. However, comparing the length of the experiment to the characteristic water diffusion time, it is clear that RH in PCL should be close to that in the channel. Another possible explanation is the misalignment of ionomer phase between the PCLs, which is exacerbated at low RH, when ionomer volume fraction is low. Thus, contact resistances are recorded as bulk PCL resistances and the membrane and contact resistance from HP extrapolated are underapproximated at 50 and 60 % RH. Lastly, for 0 PCLs with two Nafion 212 membranes, at low RH (50 and 60 %) membrane interface can be rough, which increases contact resistance. For the full range of RH the HFR values are below 2 Ohm.cm^2. These values are lower than the other two measurements of R_1 collected with DC method and are only within the range of the two DC measurements at 90 % RH or above. What is important to note is that it is not sufficient to collect a DC measurement of single PCL and subtract HFR, which should account for membrane and contact resistances. The HFR does not accurately account for membrane resistance and under-approximates it. One can use single PCL but will also need HP experiment on membranes without PCLs. As we observe here with the DC measurement at least three PCL configurations are needed to create a linear plot, as was done in **Figure 3.5a** and **b** and only by fitting the slope through resistance vs. carbon layer thicknesses one can get a precise value for effective ionic conductivity.
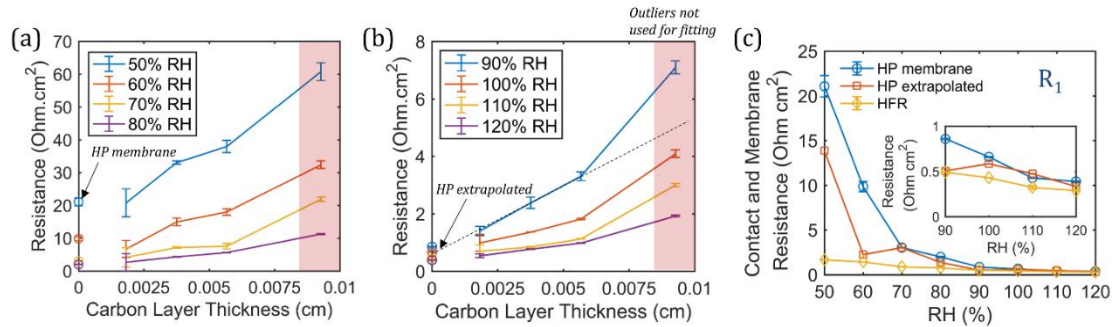
Figure 3.5 Slope of the polarization curves for PCLs of 2, 4, 6 and 10 layers for a) RH 50 – 80 % range and b) RH 90 – 120 % range, where for PCL thickness of zero membrane resistance from DC experiment for the case with no PCLs is shown. c) Values of R_1 calculated from DC measurements of membrane, extrapolation of the linear regression from parts a and b, and obtained from HFR measurements. The PCLs consist of PFSA 825 EW I/C = 1 and Vulcan XC-72.

Values of fitted slopes to **Figure 3.5** (to resistance as a function of catalyst layer thickness) are shown by **Figure 3.6**, where PCL has higher resistance than two Nafion membranes, as expected. For both the resistance values decrease as RH increases. The highest resistance values were 4500 Ohm.cm and 2100 Ohm.cm at 50 % RH, for PCL and membrane, respectively.

Figure 3.6b shows that the area specific HFR decreases with increase in RH and remains approximately invariant to PCL thickness. This is because electrically conductive material within the PCLs shorts the circuit at high frequencies and only contact and short-range membrane resistances are measured at the HFR. For the cases with PCLs, the HFR is about 1 Ohm.cm^2 at 50 % RH and decreases to about 0.3 Ohm.cm^2 at 120 % RH. HFR for two membranes is slightly higher at 50 and 60 % RH compared to when PCLs are present (1.7 vs. 1 Ohm.cm^2 at 50 %). This is most likely due to rough membrane-membrane interface that is better contacted when the PCLs are present. The membrane-membrane HFR is similar to the case when PCLs are present at

70 % and above and we think this is mostly due to membrane swelling and reducing the membrane-membrane interfacial roughness.

Figure 3.6c shows effective ionic conductivity for Nafion membrane, PFSA I/C 1 with Vulcan XC-72 PCL and Nafion membrane computed using HFR, literature values [66,73] for Nafion 212 using various set-ups are shown for comparison. The area-specific HFR data for Nafion 212 shows the highest proton conductivity but this conductivity is short-range (10s of nanometers or less), primarily due to protons transporting in aqueous portion of the ionomer [74]. Kusoglu and Weber [74] have shown Nafion morphology between PTFE backbones to consist of 1-3 nm of water clusters separated by 4- 6 nm of water channels at high degree of hydration ($\lambda > 7$). These clusters form rod-like polymer agglomerates that have crystalline regions on the order of 80 nm. The rod-like aggregates form meso-scale assembly. Nafion morphology is inherently multi-scale and interconnectivity of hydrophilic domains within Nafion depends on RH. HFR of Nafion does not account for a long-range proton transport (10s of micrometers) that is dictated by interconnectivity of polymer agglomerates. HP results are more useful to understand proton transport in actual fuel cell, as protons must transport from anode to cathode under the DC potential and the HP DC measurement is actually simulating that. The Nafion conductivity with HP DC method is about one order of magnitude lower than that estimated with HFR at 50 % RH, this difference decreases at 120 % to less than a factor of two, as when ionomer is fully hydrated, the ionic clusters are well connected within the membrane and long (10s of microns), and short-range (nanoscale) ion transport properties are the same. The HP DC ionic conductivity is mainly due to the transport of coordinated protons along the sulfonic groups via ion-hopping [75] within connected polymer aggregates. Compared to literature data, Nafion conductivity is slightly lower

to what was reported before, although the set-ups from literature were different [66,73].
Soboleva et al. [73] used ex-situ setup where membrane was sandwiched between two Pt
electrodes and EIS spectra was collected and onset of semi-circle was used as an impedance that
determined ionic conductivity.

The PCL effective ionic conductivity with HP DC method is about five times lower compared to
Nafion 212. The conductivity of PCLs of I/C 1 and 3M 825 EW increases from $\mathbf{2.2 \times 10^{-4}}$
S/cm at RH 50 % to $\mathbf{8.62 \times 10^{-3}}$ S/cm at 120 RH. Comparing ionic conductivity in the range of
50 -100 % RH reported here to that reported by Iden et al.[69], which also used HP set-up with a
PCL of I/C of 0.9 and Ketjenblack carbon support, these values are 2-4 times lower. The
conductivity values reported in this study for the PCL cannot be directly compared to Iden et al.
study, as different carbon support and processing were used. Lower effective ionic conductivity
reported here might be due to lower homogeneity of ionomer distribution and will depend on ink
formulation and processing. [76–78]
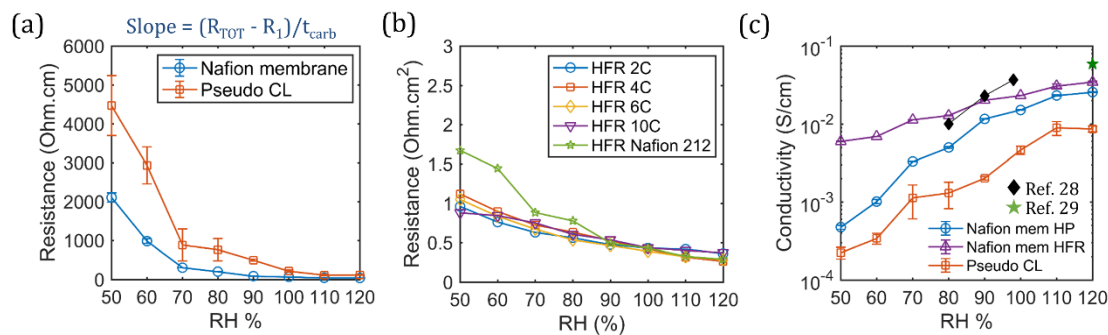
**Figure 3.6 a) Values of resistances that represent slope from Figure for a range of RH
from 50 to 120 %, b) HFR as a function of RH for 2, 4, 6, 10 PCLs and Nafion membrane,
c) effective conductivity values for Nafion membrane from DC measurement and HFR, and**

that of PCL of PFSA EW 825 I/C = 1 and Vulcan XC-72. Temperature is 80 °C and 100 kPa backpressure. Literature references are from [66,73].

3.3.3   Comparison of DC and AC methods for measuring ionic conductivity

The DC method is lengthy and requires at least two to three cell builds to extrapolate membrane and contact resistances from actual ionic conductivity. The fitting procedure for the DC method is straight-forward but lengthy. An alternative method is to fit the AC impedance spectra, as previously was outlined by Kramer et al. [71] and outlined here in the AC Method Section. The low-frequency real resistance from the spectra should correspond to the DC measurement. **Figure 3.7** shows Nyquist plots for no PCLs (just two Nafion membranes), and a set-up with 2, 4 and 6 PCLs with I/C of 1 and RH of 50 to 120 %. Here we also discarded the measurement of the 10-layer samples for the reasons outlined in the previous section. As can be seen in **Figure 3.7**, as RH increases, the real-axis intercept at low frequency decreases, indicating a decrease in overall ionic resistance. **Figure 3.7** describes the equivalent circuit that was used to fit the Nyquist plots of the AC HP data.
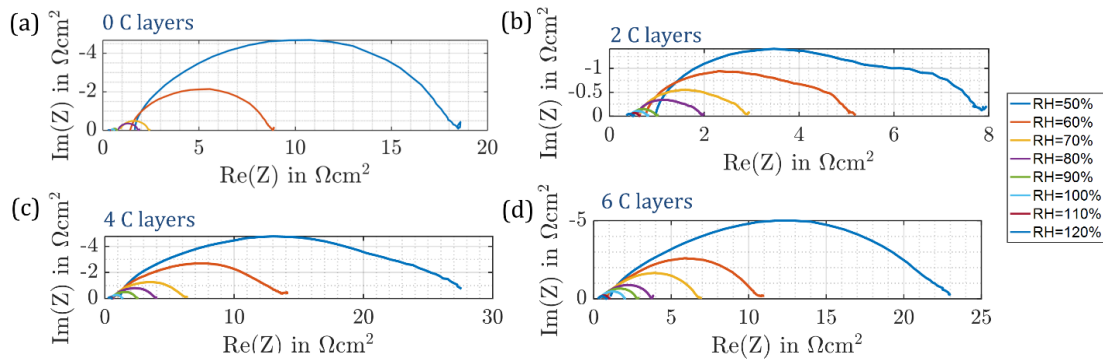
Figure 3.7 Nyquist plots for 0, 2, 4 and 6 pseudo CLs of PFSA I/C = 1 at RH range of 50 to 120 %.

Figure 3.8 shows fitting results for 2 PCLs at -0.1 V and for RH range from 50 to 120 %. **Figure 3.9** shows complete ionic conductivity values from AC HP fitting at every potential (from 0 to -0.4 V) as a function of RH. The effective ionic conductivity values for 2, 4 and 6 PCLs show similar values. We selected ionic conductivity values at 0 and -0.1 V for Nafion and for 2, 4 and 6 PCLs, as at higher potentials there might be additional resistances due to Faradaic reactions. The resulting effective conductivity values are plotted in **Figure 3.11**. For Nafion membranes we observe higher ionic conductivity at high RH for AC method, whereas lower ionic conductivity values for low RH range. We believe the discrepancy between DC and AC method for Nafion membrane at RH > 100 % is due to condensation of water at membrane-membrane and membrane-GDE interfaces, as water content in membranes above 100 % can significantly vary depending on local temperature, interfacial voids etc. In 70- 100 % RH range both methods showed good agreement.
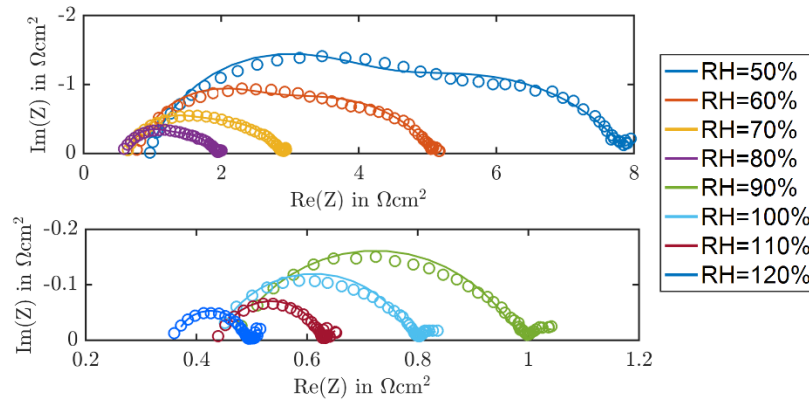
Figure 3.8 Nyquist plot fits for 2 pseudo CLs of PFSA I/C = 1 and RH range of 50 to 120 %.
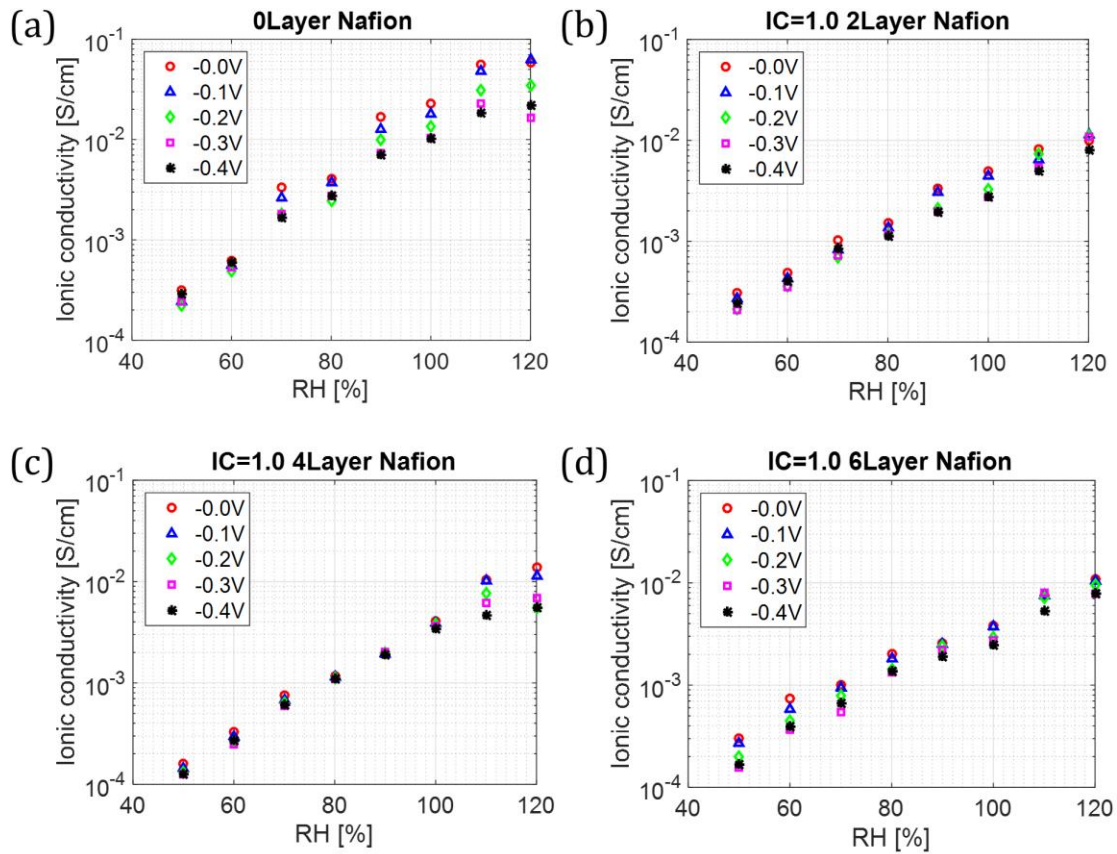
Figure 3.9 Effective ionic conductivity as a function of RH for applied potentials of 0 to -0.4 V and layer with I/C ratio of 1 and also the case of no pseudo CL but just two membranes. Pseudo CLs of 2, 4 and 6 layers are shown.

For the PCLs, extremely close values were obtained between AC and DC measurements for a full potential range. **Figure 3.10** shows relative difference between the DC and AC methods.
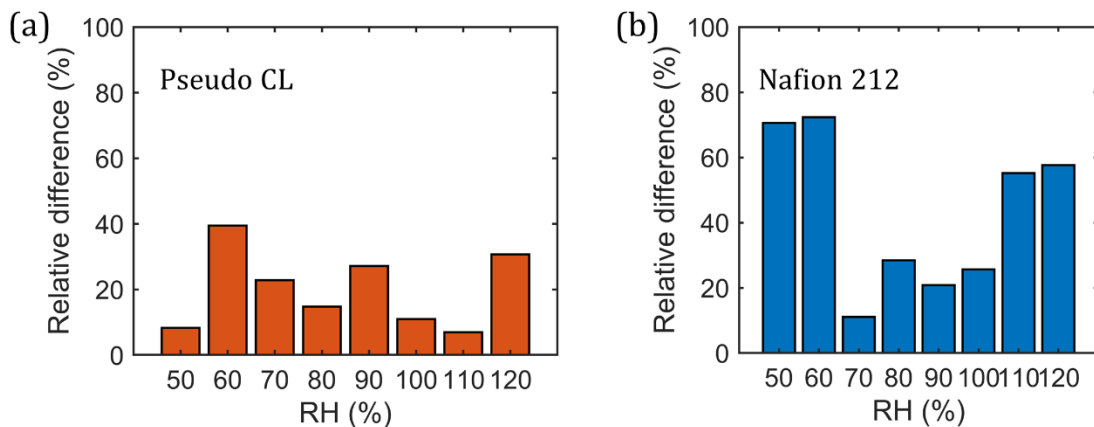
Figure 3.10 Relative difference between DC and AC measurements for a) pseudo CL and b) Nafion 212 membrane.

For PCLs, all of the effective conductivity values from DC and AC measurements are within 40 % of agreement to each other and most of them are within 20 %. Considering the fact that ionic conductivity spans two orders of magnitude from 50 to 120 % these statistics indicate that both methods provide similar values and can be used interchangeably. For the Nafion 212 membrane we observe less precision between DC and AC measurements in high and low RH range but below 30 % deviation in the RH range from 70 to 100 %. Overall, the plots show that the AC method can be used instead of DC method for measuring effective ionic conductivity of PCLs, given the correct AC Nyquist plot interpretation.
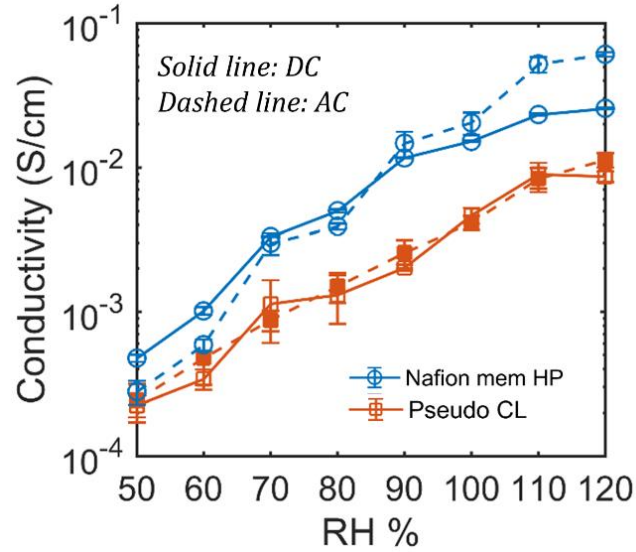
Figure 3.11 Effective ionic conductivity as a function of relative humidity for Nafion membrane and PCL of PFSA 825 EW I/C = 1. Comparison of DC and AC methods within the HP experiment.

3.3.4 Method extension to PCLs with varied I/C ratios

Next, we extend the DC and AC methods to PCLs with PFSA ionomer but varied I/C ratios. **Figure 3.12** shows polarization curves for I/C 0.6, 1 and 1.4 for 2, 4 and 6 PCLs, under 50 – 120 % RH using the DC method. For these experiments 3M 825 EW membranes were used instead of Nafion 212.
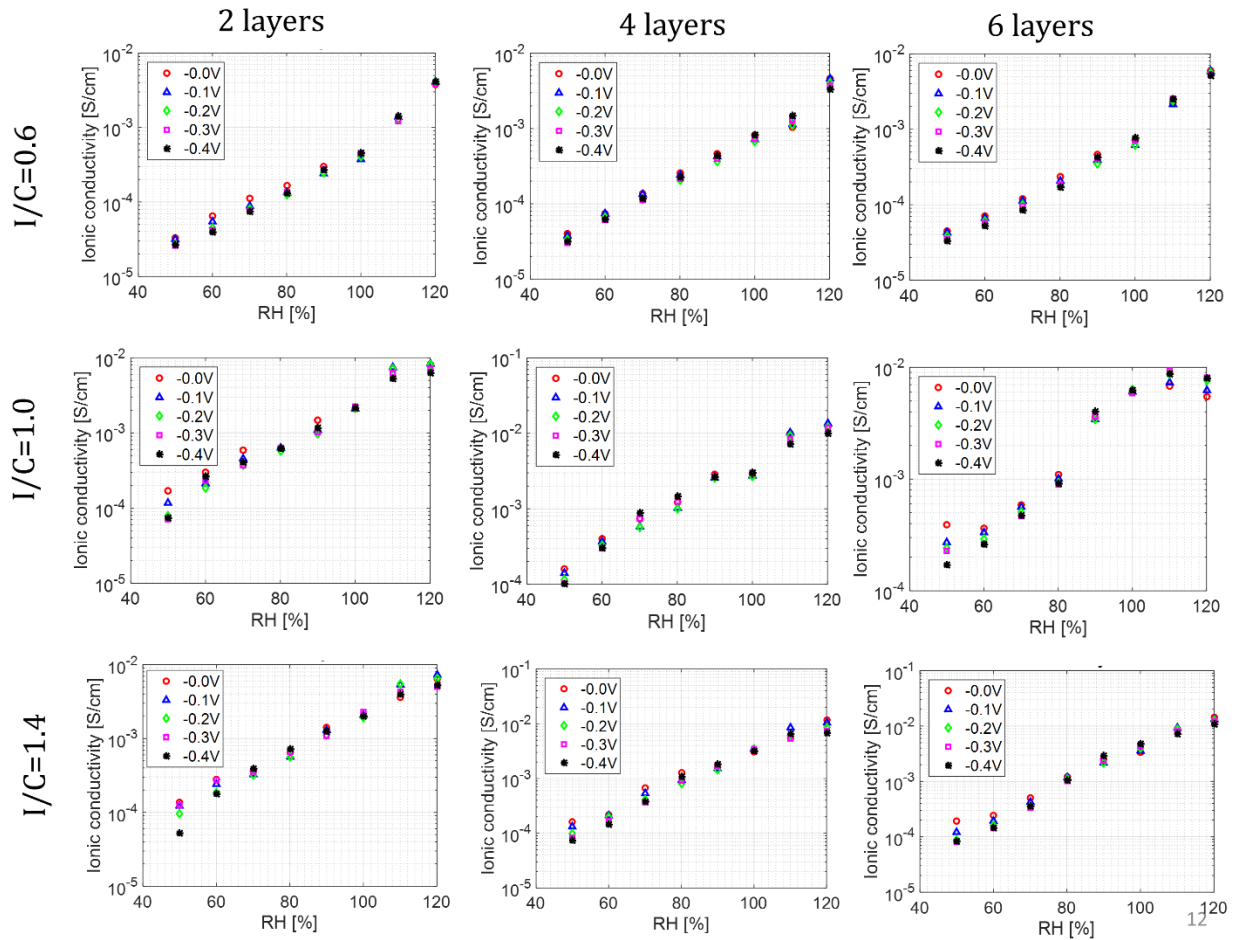
Figure 3.12 Effective ionic conductivity as a function of RH for applied potentials of 0 to -0.4 V and layers with I/C ratios of 0.6, 1 and 1.4 for pseudo CLs of 2, 4 and 6 layers

We fitted linear region from 0 to -0.3 V in **Figure 3.13**Figure polarization curves to obtain **Figure 3.14**, where resistance is plotted as a function of PCL thickness. For all three I/C ratios and RHs, we observe linear fits that produce positive y-intercepts.

70
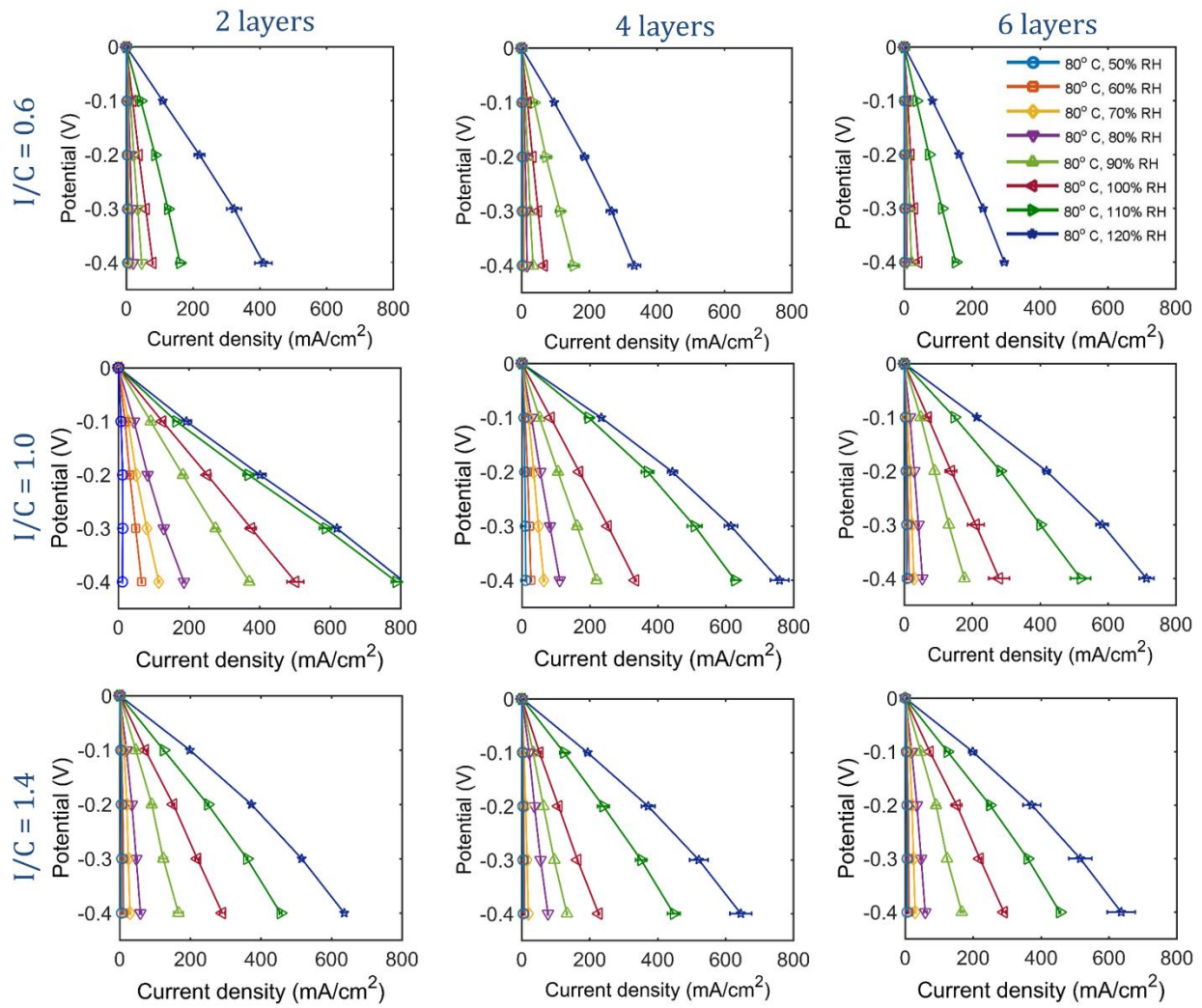
Figure 3.13 Polarization curves of hydrogen pump experiments for pseudo CLs PFSA I/C 0.6, 1 and 1.4 for stacks with 2, 4 and 6 pseudo CLs at various RH and 80 °C and 100kPa backpressure.
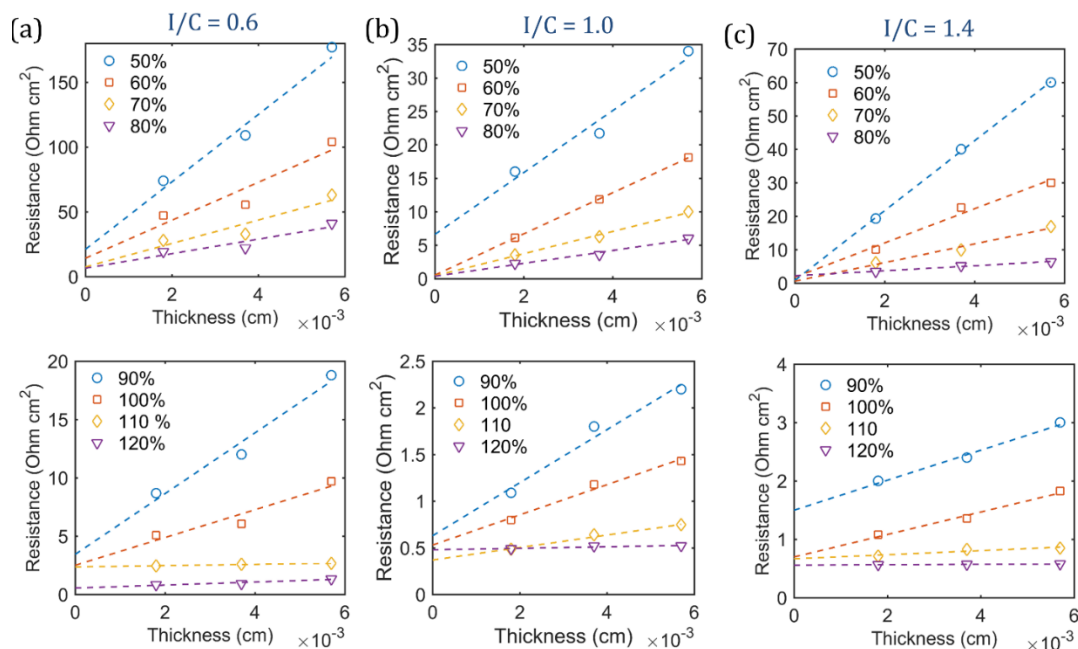
Figure 3.14 Slopes of the polarization curves for PCLs of 2, 4, 6 layers for RH 50 – 80 % range (top) and RH 90 – 120 % range (bottom) for a) I/C = 0.6, b) I/C = 1.0 and c) I/C = 1.4. Fitted lines are used to extrapolate R_1 and calculate slope.

We observe 3-4 times increase in contact and membrane resistance at RH 50-70 % for I/C = 0.6 compared to I/C = 1, as shown by **Figure 3.15**. Since the membrane was the same for all three measurements, the reason for this increase in contact resistance at lower RH range might be due to contact resistance between the layers and the membrane. Layer to layer contact and layer to membrane contact can become important when the ionomer percolation is low, and can be exacerbated at low RH. For layers to bond together during hot pressing ionomer needs to be present at near the surface of the layer to bond to the ionomer in the adjoining layer. With lower I/C ratio there is possibility of ionomer domains mismatch between the layers and this mismatch will be higher at lower RH, where swelling of ionomer is reduced. Slope from **Figure 3.14** or resistance values for all three cases are shown by **Figure 3.15**, where I/C = 0.6 case shows values that are about an order of magnitude higher than I/C = 1 and I/C = 1.4 for the whole range of RH.

The resistance for I/C = 1 and I/C = 1.4 shows similar values. Again, to explain unexpectedly high contact resistance and also higher slope for PCL with I/C = 0.6 we look at a cross-section tomograph with cesium (Cs)-stained ionomer, comparing I/C = 0.6 and I/C = 1.4, as shown in **Figure 3.15c**. The details for nano X-ray computed tomography imaging, and Cs staining have been reported before, in Ref. [79]. For I/C 1.4 when ionomer was ion-exchanged with Cs+, which is a heavy ion, the regions stained with Cs+ will show up as bright under x-rays. This is indicative that Cs diffused throughout ionomer network and that the network is well-percolated within the PCL. However, for PCL with I/C = 0.6 only the surface of the PCL shows up as bright, the middle portion of the layer remained dim, indicating that Cs+ did not diffuse into the center of the layer, showing that ionomer percolation might be an issue.
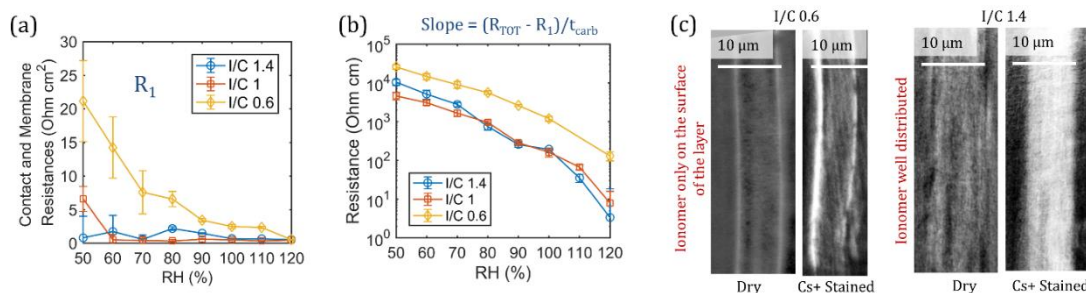
Figure 3.15 a) Contact and membrane resistances (R₁) as a function of RH and b) slope from Figure as a function of RH for I/C 0.6, 1, and 1.4. c) Cross-section tomographs of stained ionomer and PCL of I/C 0.6 and 1.4.

Figure 3.17 shows Nyquist plots for 2, 4 and 6 PCLs for I/C 0.6, 1 and 1.4 and RH range from 50 to 120 %. For I/C 0.6 and RH 50 % for all three configurations we observe two semi-circles on the Nyquist plot. As already discussed in AC Method Section at this relatively low I/C ratio, two time-scales for proton transport are present due to long range of proton hopping and also due to ionomer network having a low degree of percolation at low RH. These two semi-circles are also observed for up to 90 % RH for PCL with I/C = 0.6. Using 4 PCLs, I/C = 0.6 as an example,

we carried back-of-the-envelope calculations of current penetration depth for a frequency at which the semi-circles separated and reported them in here.

As the frequency decreases, protons transport into the PCL and the penetration depth of the AC current increases. At low I/C ratio of 0.6, especially at low RHs, the ionomer phase can become disconnected at some locations within the layer, or in-between the layers and the impedance of the PCL is separated into two parts as shown in **Figure 3.17c**. A Nyquist plot example of this case is the I/C = 0.6, 4 layers case in **Figure 3.16** at low RHs (50 % - 80%). The Nyquist plots are clearly separated into 2 parts, each corresponding to different time constant. For the same PCL sample, at different RHs, the position of the ionomer disconnection should keep unchanged. This can be verified by calculating the corresponding penetration depth at the frequency at which the curve in the Nyquist plot separates into two parts, i.e. the intersection of the two semicircles. The current penetration depth at this intersection is the position of the ionomer disconnection. An equivalent way to verify this, is to calculate the ionomer disconnection position at one RH (i.e. 50 %), then calculate the corresponding frequencies at different RHs for the same penetration depth. Then, one can compare the calculated frequencies to the measured frequencies at the intersection of the two semicircles.

In the model shown in **Figure 3.2**, the constant phase element is used to account for the non-ideal behavior of the distributed double layer capacitance. We first transform the fitted CPE parameter T into the capacitance C by using the following equation

$$C_1^\phi = T_1 / \left(\frac{1}{R_{mem}} + \frac{1}{R_1} \right)^{1-\phi} \tag{38}$$

The subscript 1 denotes the part that has been penetrated by current. The penetration depth at frequency f can be calculated as:

$$\delta = \sqrt{\frac{4\sigma_{eff}}{aC_1 f}} \tag{39}$$

From the Nyquist plot in **Figure 3.16**, we can read the value of the real portion of the impedance at the semi-circles intersection, and then from the experimental results, we can look up the corresponding frequency. For I/C = 0.6, 4 layers, the frequency at the intersection is ~103 Hz at 50 % RH. For a reasonable estimated specific area of $a \approx 3 \times 10^8 \, m^{-1}$, the current penetration depth at this frequency is around 33 µm. This corresponds to the position of the ionomer disconnection of around 33 µm depth.

We transform Eq. (2) to calculate the corresponding frequency for a fixed penetration depth:

$$f = \frac{4\sigma_{eff}}{aC_1\delta^2} \tag{40}$$

For the same sample, the position of the ionomer disconnection should keep unchanged at different RHs. From Eq. (S4), we can calculate the corresponding frequencies at different RHs when protons penetrated to the ionomer disconnection position. With these calculated frequencies, we can look up the experimental data to find the corresponding impedances. In the following **Figure 3.16**, for 60 % - 80 % RH, the vertical lines show the locations corresponding to the calculated frequency for current penetration depth of 33 µm. We can see that they have very good agreement to the intersections of the two semicircles. Therefore, we successfully verified that for different RHs, the position of the ionomer disconnection keeps unchanged. This

75

verification confirms our theoretical model that the separation of the Nyquist plot into two part is due to ionomer disconnection at low I/C and RHs. On the other hand, for a reasonable estimation of specific area, the calculated penetration depth, i.e. 33 μm, is right within the PCL thickness (the total thickness of 4 layers is ~37 μm). Thus, this confirms the length and time (frequency) scales of the proton penetration until the ionomer disconnection.
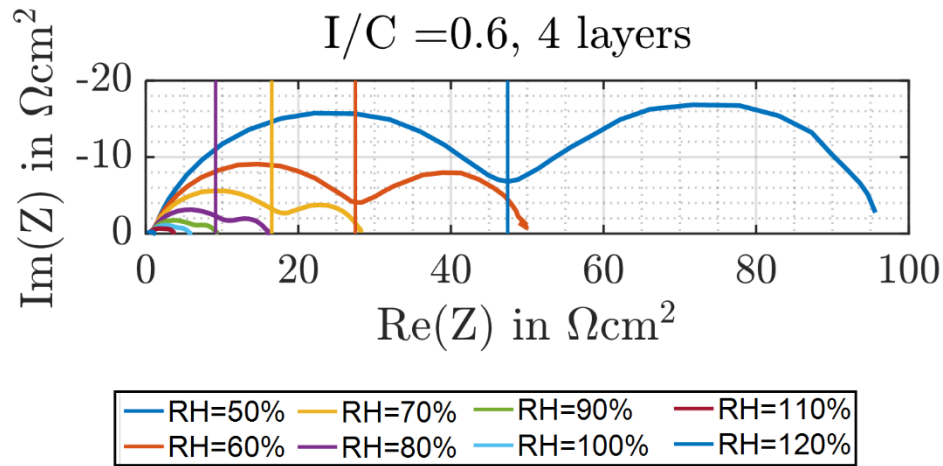
Figure 3.16 Nyquist plot for 4 PCLs of I/C = 0.6 and a range of RH from 50 to 120 %. The vertical lines show calculated frequencies for a current penetration dept of 32 μm.

The semi-circles on the Nyquist plot separated at around 103 Hz for a RH range of 50 -90 %. This frequency corresponded to effective current penetration distance of 32 μm, which is within the PCL thickness range. The calculations used approximate specific area and can be only approximate, however, they show that ionomer discontinuity or lack of percolation is long-range phenomena. Single semi-circle is observed for I/C = 1 and 1.4, even at 50 % RH.
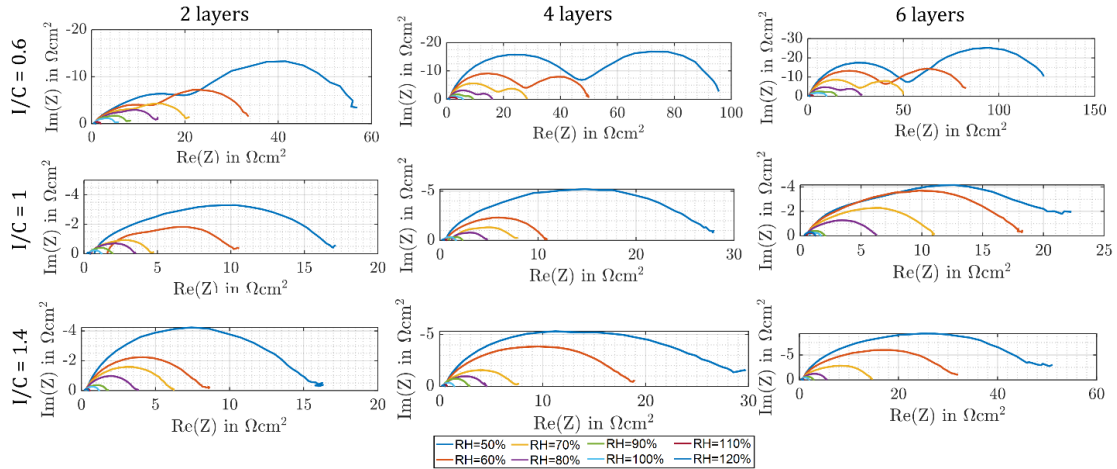
Figure 3.17 Nyquist plot for 2, 4, and 6 PCLs (columns) in hydrogen pump set-up and I/C 0.6, 1, and 1.4 (rows). Impedance spectra is shown for RH range of 50 to 120 %.

Ionic conductivity for I/C 0.6, 1 and 1.4 for a range of RHs from 50 to 120 % is compared for AC and DC methods. **Figure 3.20** shows that both methods predict lower effective ionic conductivity for I/C of 0.6 compared to I/C 1 and 1.4, since lower I/C ratio will have lower volume fraction of ionomer and also perhaps more tortuous ionomer. Ionic conductivity is a strong function of RH, as about 2.5 order of magnitude in ionic conductivities is observed when RH increased from 50 to 120 % RH. PCLs with I/C 1.0 and 1.4 had very similar conductivities with AC method for the whole range. With DC method, I/C 1.4 had higher conductivity at 110 and 120 % RH than I/C 1 but lower at 50-70 % RH. **Figure 3.18** shows a good agreement for PCL I/C = 1 ionic conductivity measured with set-up having Nafion 212 thicker membranes (taken from **Figure 3.4**) and that with set-up having 3M 825 membranes that are 20 µm in thickness.
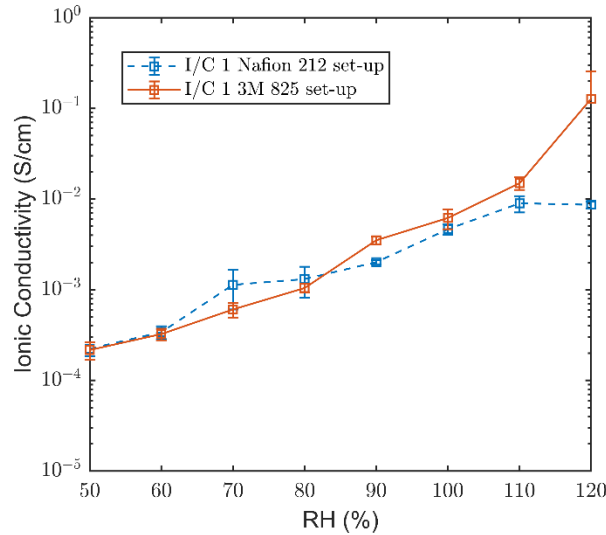
Figure 3.18 Comparison of ionic conductivity for PCL of I/C = 1 for the set-up with Nafion vs that of 3M 825 EW membrane

For I/C = 0.6 AC and DC methods have excellent agreement up to 100 % RH, both values overlap within the error bars. At 110 and 120 % RH we observe DC method showing slightly higher effective ionic conductivity, compared to AC method. **Figure 3.19**Figure 3.19 shows the relative difference between DC and AC methods, as defined by Eq. (S1).
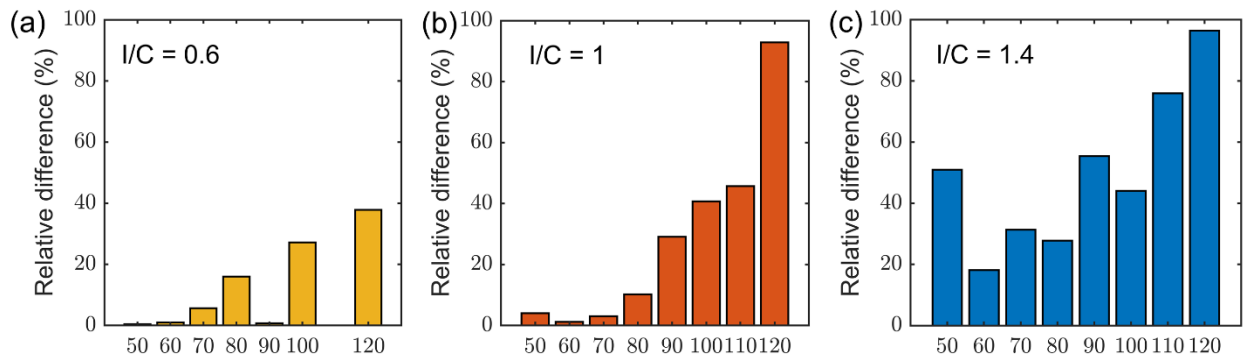
Figure 3.19 Relative difference between DC and AC effective conductivity measurements for I/C of a) 0.6, b) 1, and c) 1.4.

For I/C = 0.6 both methods agree within 40 % for the whole RH range and within 20 % for up to 90 % RH, which is a very good agreement considering the span of values having two orders of magnitude. For I/C = 1 the agreement between DC and AC is within 40 % for RH 50-90 % and higher than that at 100 -120 %. Below 30 % agreement between DC and AC method is observed for I/C = 1.4 and RH range from 60 - 80 %. For 110 and 120 % RH it seems that DC method for both I/C = 1 and I/C = 1.4 shows an order of magnitude increase in ionic conductivity compared to AC method. Again, values above 100 % RH generally have large error bars as these values will depend on the presence of liquid vs vapor water, condensation in micro pores etc.
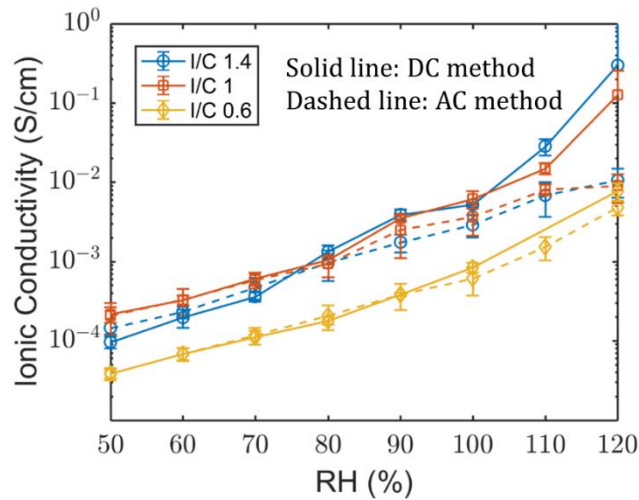
Figure 3.20 Effective ionic conductivity as a function of RH for PFSA I/C = 0.6, 1 and 1.4. Comparison of the AC and DC methods.

3.3.5 Tortuosity factor calculated using HP method

Lastly, using both DC and AC effective conductivity values we calculate tortuosity factors for three PCLs with I/C 0.6, 1 and 1.4 using Eq. (9) and ionomer volume fractions obtained with Eq. (10). Membrane conductivity values from DC measurements are reported in **Figure 3.21**.
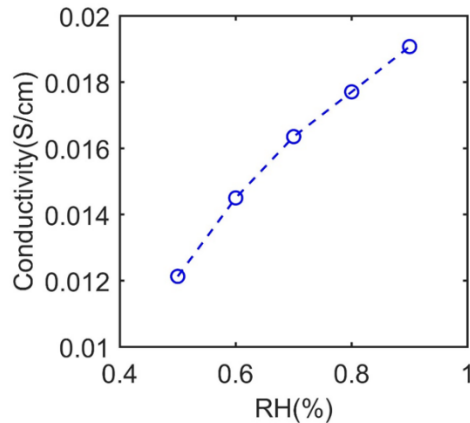
Figure 3.21 Membrane 3M 825 EW conductivity measured with DC hydrogen pump method.

For I/C = 0.6 tortuosity value with both methods was 6.1 for RH of 50 % and decreased to 3 at RH 90 %. I/C = 1 had lower tortuosity than I/C 1.4 for the range of 50 – 70 % RH and ranged from 3.5 to 1.5 in this range. Based on these findings it is evident that increasing I/C ratio from 1 to 1.4 does not increase ionic conductivity at RH below 100 % because additional ionomer came at expense of ionomer tortuosity. Ink processing and preparation play key roles in the PCL preparation and impact ionomer dispersion and its tortuosity.

DC method showed higher tortuosity factor for I/C = 1.4 at 50 % RH compared to AC method, 6 vs. 5, respectively. For both I/C = 1 and I/C = 1.4 tortuosity factors decreased to 1.5 at RH 90 %. For I/C = 0.6 and 1 AC and DC methods showed very similar tortuosity values, indicating that either method can be used. Tortuosity values reported here in the range of 50 - 80 % RH are higher than previously reported by Liu et al. [65,80], as effective proton transport resistance is higher in this work. Liu et al. [65,80] used H_2/N_2 EIS technique for measuring effective proton transport resistance, whereas here DC/AC method in HP configuration was used. These two methods deviate at low RH, which is the subject of our follow-up study. Furthermore, PCLs and

actual CLs that contain Pt will have different ionomer distribution due to additional ionomer- Pt interaction, and thus tortuosity and film conformity will change.
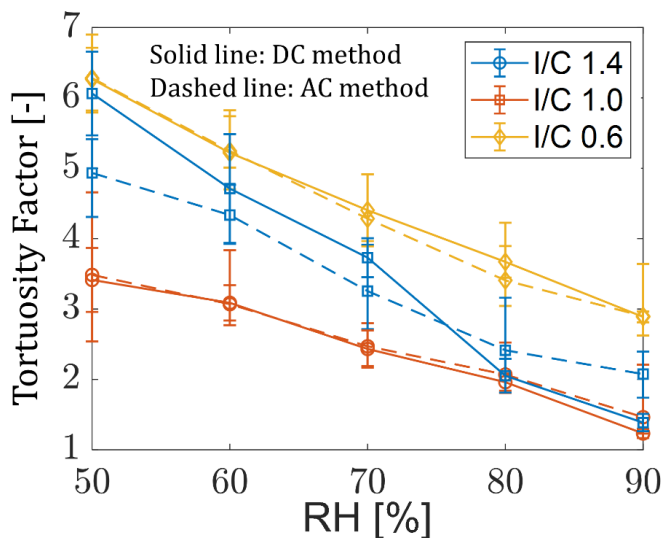
Figure 3.22 Tortuosity factor as a function of RH for PCLs with PFSA I/C 0.6, 1 and 1.4 and Vulcan XC-72.

3.4 Conclusion

We developed an alternative AC ion conductivity method that we compared against the conventional DC method for measuring proton conductivity in pseudo catalyst layer (PCLs) of PEFCs. Hydrogen pump (HP) method was used to measure ionic conductivity of PCLs. In the HP set-up PCLs were sandwiched between two membranes and pressed between anode and cathode GDEs. The number of layers varied between 2, 4, 6 and 10. DC method was used to apply potential between 0 and -0.4 V to record polarization curves for a RH range from 50 to 120 %. After which the slopes of the polarization curves were plotted as functions of PCL thickness. Again, the slope of the line of resistance vs. PCL thickness was effective proton resistance and is inversely proportional to the PCL effective ionic conductivity. Additionally,

EIS spectra was collected for each applied potential, where the resistance between real values of the HFR and low frequency x-axis intercept is effective proton resistance. The DC and AC methods were compared for Nafion 212 membrane, and PCLs with I/C 0.6, 1 and 1.4. Both methods show good agreement up to 100 % RH, whereas above 100 % RH in several instances DC method shows higher effective ionic conductivity. Using these effective ionic conductivity values we extract ionomer tortuosity factors for the three layers at 50 to 90 % RH, where at 90 % RH tortuosity factors for I/C 1 and 1.4 were close to 1, whereas tortuosity factor for I/C 0.6 was 3. Tortuosity factors increased linearly with decrease in RH, where at 50 % RH PCL with I/C 0.6 had the highest tortuosity factor of 6.1, as predicted by both DC and AC methods. HP method allows determination tortuosity factors for ionomers within PCL. Optimizing ionomer content, ink composition and processing can help reduce ionomer tortuosity and increase effective conductivity, which directly will impact electrode polarization behavior.

AC method requires single potential (0 V or -0.1 V) for measurements and single PCL. The AC data interpretation is straight-forward, as only real component of Nyquist plot is considered and does not involve several steps of linear regression fitting to the slopes as in DC method. Therefore, AC method within the HP set-up measures through-plane effective proton conductivity, and has all the advantages of the HP DC method but is easier to implement and to interpret. It can be a high throughput method for ionomer conductivity and tortuosity determination within the PCL.

Chapter. 4 Investigation of catalyst layer ionic conductivity using H_2/N_2 electrochemical impedance spectroscopy and transmission line model.

4.1 Introduction

In last chapter, hydrogen pump methods were investigated, and ionic conductivity of catalyst layer was study. Several methods except HP method have been developed to understand ionomer distribution and ionomer conductivity during fuel cell operation. In 1980s Gottesfeld et al. [81] used electrochemical impedance spectroscopy (EIS) technique to measure ionic conductivity in catalyst layer using equivalent circuits to interpret the measurements. Later, Eikerling and Kornyshev first showed that the EIS impedance response in the catalyst layer can be described by a one-dimensional transmission-line model (TLM) [82]. Then Mark C. Lefebvre and has co-workers [83] discussed the TLM operated in H_2/N_2 condition. Baker and collaborators included the catalyst layer thickness and relative humidity (RH) to investigate proton resistivity using a TLM [65,84,85]. Jiang et al expanded and tested a TLM capable of isolating and quantifying the resistance contributions from the membrane, the electronic components, and the membrane–electrode interfaces using EIS measurements [86]. EIS measurements in combination with the TLMs have further increased in precision and capability [87]. Obermaier et al. developed a one-

dimensional TLM with additional elements of adsorption and side reactions making the model more comprehensive but at the same time requiring catalyst layer morphology as an input [58].

In this work, effective ionic conductivity of pseudo catalyst layers (PCLs) with several ionomer to carbon (I/C) ratios are measured using H_2/N_2 EIS technique over a relative humidity (RH) range of 50–120 %. In our previous study, effective ionic conductivities were measured for same PCLs using hydrogen pump (HP) technique [88]. Since it is critical and unique that a comparison between EIS and HP techniques can be made. We believe the comparison between different techniques regarding configurations, mechanisms and results would bring insights and inspirations in PEM fuel cell catalyst layer investigations.

HP and EIS have obvious difference regarding configurations, for HP set up, multiple PCLs were placed between two membranes. A typical fuel cell anode and cathode components were used on the outer side of each membrane. Then the DC potentials were applied to transport protons through the "membrane sandwich" from the anode to the cathode. We also developed an alternating current (AC) method with the same HP set-up and found that effective ionic conductivities of HP DC and HP AC agree very well. The disadvantage of DC or AC HP methods is that Pt cannot be used in the PCLs because hydrogen that crosses through the membrane will react and transport the current electrically. For EIS set up, we use a conventional fuel cell set-up with the PCLs and Pt/C as cathode layers. Pt/C catalyst layers were measured and compared in this work since HP method could not be used to measure the real catalyst layer effective ionic conductivities. Comparisons of mechanisms and results bring thoughts in PEM fuel cell modeling research. In this work, 2D models using two effective ionic conductivities

measured by EIS and HP are discussed and compared to determine which method is more practical, and it is shown in later sections.

Furthermore, a detailed study was conducted to investigate possible factors that can affect effective ionic conductivity, including RH, Pt presence, and ionomer content.

4.2 Data analysis and equivalent circuit model fitting methods

Figure 4.1 shows a schematic of the PEFC set-up and two equivalent circuits. **Figure 4.1b** represents the TLM of one single pore completely filled with ionomer, and it is considered as consisting of many parallel capacitors C_i connected with proton transport resistors R_{H^+} between each capacitor. According to deLevie's model, the impedance of each pore (**Figure 4.1b**) in the catalyst layer can be considered as:

$$Z_{deLevie} = (R_0 Z_0)^{1/2} coth(l\sqrt{\frac{R_0}{Z_0}}) \tag{41}$$

where, R_0 is the electrolyte resistance for unit length, Z_0 is the interfacial impedance for unit length, and l is the length of each pore [87].

In contrast to Obermaier et al. [58], which considers the pore size distributions, and specific TLM for each pore, we simplify the entire catalyst layer to be represented by the TLM of a single cylindrical pore with representative parameters. Hence the impedance of the catalyst layer can be represented as:

$$Z_{CL} = (R_0 Z_0)^{1/2} coth(l\sqrt{\frac{R_0}{Z_0}}) \qquad (42)$$

$$R_0 = \frac{1}{\sigma_{eff}*A} \qquad (43)$$

$$Z_0 = \frac{1}{A_S*A*\omega*C_{DL}*j} \qquad (44)$$

where A is the active area of the cell, A_S is the specific surface area, i.e. $1.5 * 10^7$ 1/m [89], σ_{eff} is the effective ionic conductivity of the catalyst layer, ω is the angular frequency, C_{DL} is the double layer capacitance and j is the unit of imaginary number.

Figure 4.1c shows the equivalent circuit adopted from Obermaier et al. [58]. The model neglects the impedance response of anode catalyst layer, as it is shorted by the fast hydrogen oxidation reaction. Also because of the absence of the reactive gas and hence there are no Faradaic resistances in cathode. Z_{cl} represents the impedance of the cathode catalyst layer which can be determined using TLM. The capacitors in TLM represent the contacts between ionic phase and electronic phase, i.e. the contact between electrolyte and Pt/C surfaces. In view of these, ion species adsorption and side reactions which can affect the measurements should be taken into account. Hence, the resistor and capacitor of ion species adsorption, specifically sulfonic acid group adsorption, and resistor of side reaction, specifically hydrogen crossover are added into the cathode equivalent circuit are added in equivalent circuit. In **Figure 4.1c**, the adsorption capacitor, C_{ads} and adsorption resistor, R_{ads} are connected in series. They represent the sulfonic

86

acid groups adsorption of ionomer on Pt electrocatalyst and other species adsorptions. Side reactions term R_{SR} represent impedance caused by hydrogen crossover through membrane and possible presence of trace amounts of oxygen.

Overall, the modeled equivalent circuit of the cell in this paper is shown in **Figure 4.1c**. It consists of three components in series: membrane resistance, the impedance of cathode catalyst layer and the electrical resistance of the diffusion media R_{DM}. The equivalent circuit of cathode catalyst layer is a sum of parallel connections of impedance of proton transport Z_{CL}, adsorption resistance R_{ads} and capacity C_{ads} in series, and the side reaction, R_{SR}. R_{mem} denotes the sum resistance of membrane ion transport resistance and contact resistances.

Based on the total equivalent circuit shown (**Figure 4.1c**), total impedance and impedance of the cathode catalyst layer is considered as:

$$R_{tot} = R_{mem} + R_{cath} + R_{DM} \qquad (45)$$

$$\frac{1}{R_{cath}} = \frac{1}{Z_{cl}} + \frac{1}{R_{ads} + Z_{ads,C}} + \frac{1}{R_{SR}} \qquad (46)$$

Fitting code was written in MATLAB. For the fitting, the input parameters include cell area A, specific area A_S, angular frequency ω, real resistance from Nyquist plot Z_{real}, imaginary resistance from Nyquist plot Z_{img}, and the length of catalyst layer l. Effective ionic conductivity was obtained by fitting the impedance spectroscopy.
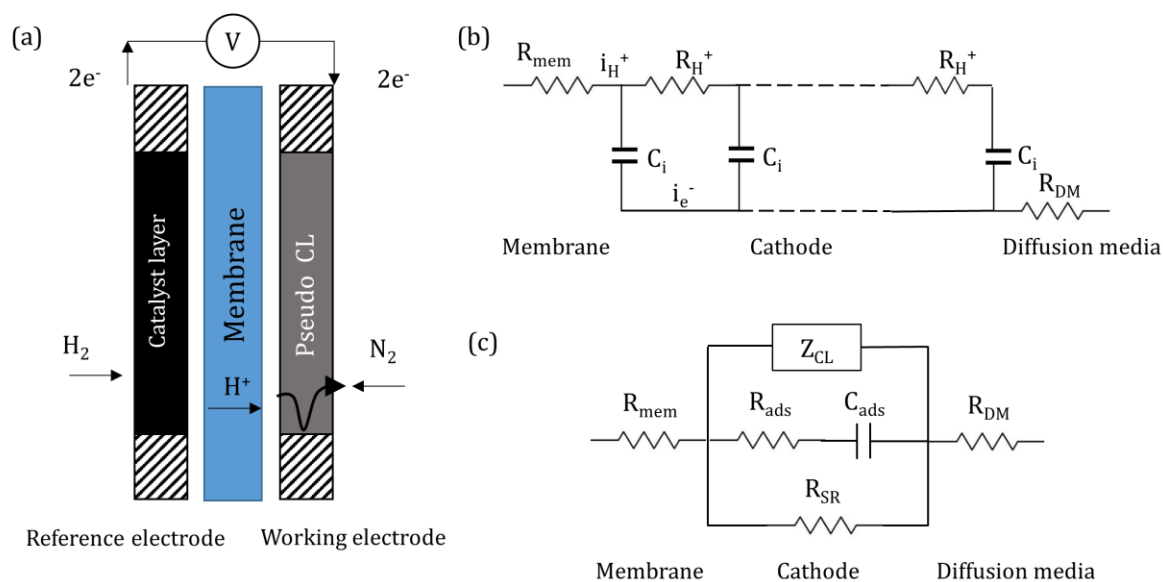
Figure 4.1 a) Schematic of the set-up for H_2/N_2 EIS, b) conventional TLM for a single pore and c) the total equivalent circuit used in this study, which is adopted from Ref 19.

4.3   Results

4.3.1   SEM results

Figure 4.2 shows SEM cross-section of the PCL, where good adhesion between PEM and a PCL was observed after hot press. We observed a PCL to be of uniform thickness. EDS results show distribution of platinum (Pt) and carbon (C) within the catalyst layer and PCL, respectively. Pt particles are seen in anode catalyst layer region above membrane, and we confirm that in the cathode PCL there is carbon but no Pt.
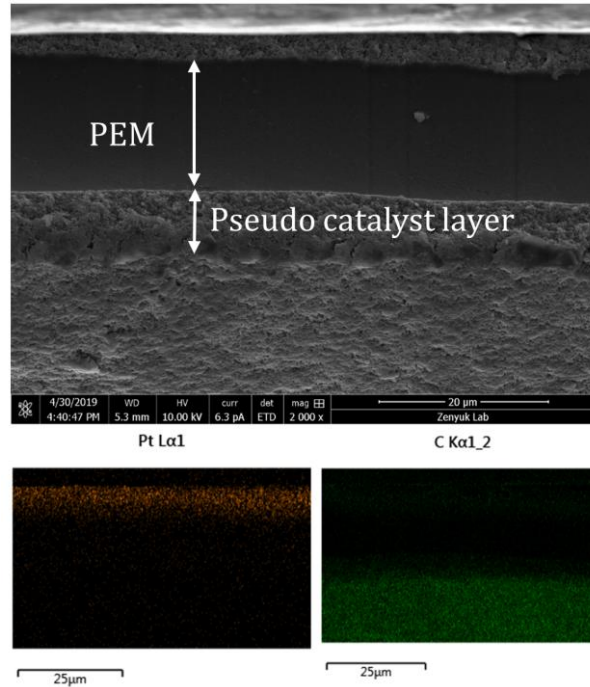
Figure 4.2 Cross section SEM image of a PCL coated CCM with I/C ratio of 0.6 where PCL is hot pressed onto a PEM (top), Pt and C EDS mapping (bottom).

It is critical to know the influence of the interface between PCLs and membrane on effective ionic conductivities. In **Figure 4.3**, we compare the effective ionic conductivity of PCLs that were physically pressed and hot pressed onto the membranes for both low and high I/C ratios. From the results, the effective ionic conductivities of hot-pressed PCLs are much higher than the PCLs without hot-pressing. However, the PCL effective ionic conductivities are independent to the hot press conditions.
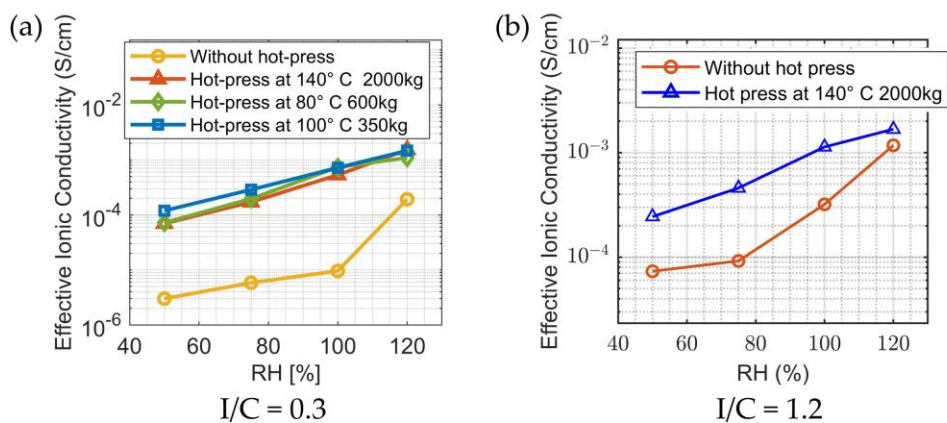
Figure 4.3 a) Hot press effect on ionic conductivity of PCLs with I/C ratio of 0.3 for a range of RH from 50 to 120 %, b) hot press effect on ionic conductivity of PCLs with I/C ratio of 1.2 for a range of RH from 50 to 120 %.

4.3.2 PCLs ionic conductivity

Figure 4.5 shows the Nyquist plots for the PCLs with I/C ratios of 0.3, 0.6, 1.0 and 1.4 at RHs of 50, 75, 100 and 125 %. An example of the fitting of the PCL Nyquist plot is shown in **Figure 4.4**Figure .
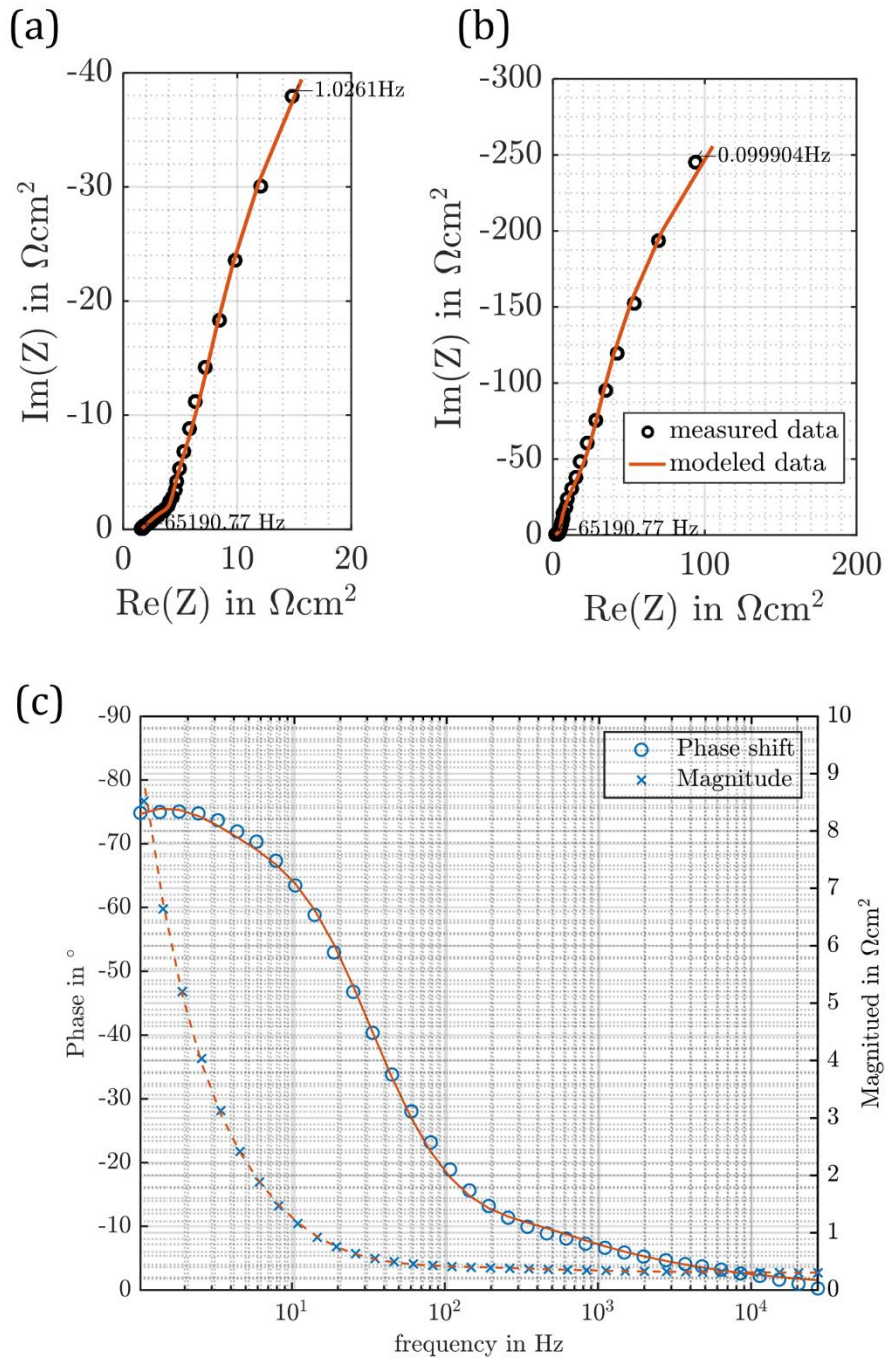
Figure 4.4 a) Nyquist plot for PCLs using TML model for frequency larger than 1Hz, b) Nyquist plot for PCLs using TML model for full frequency range. C) bode plot.

Overall, a good fit was obtained for Nyquist plots using TLM. The HFR shown in Nyquist plots is the summation of the contact resistance and membrane ion transport resistance. The HFR decreased with increasing RH for all four I/C ratios, which is due to the increased conductivity of a more hydrated membrane and decreased contact resistance between membrane and catalyst layer. We see a decreased length of the 45° segment at intermediate frequencies with increased RH and I/C ratio. Qualitatively, a 45° segment on Nyquist plot represents one-third of proton transport resistance, $R_{CL}/3$ [83]. Decrease in length of a 45° segment is due to proton transport resistance decreasing and proton conductivity increasing with increased ionomer and water content. HFR is smaller when PCL I/C ratio is higher due to better contact between the PCL and membrane. An outlier is the PCL with I/C ratio of 1.4, which has higher HFR. It could be resulted from some large contact resistance between the GDL and flow fields.
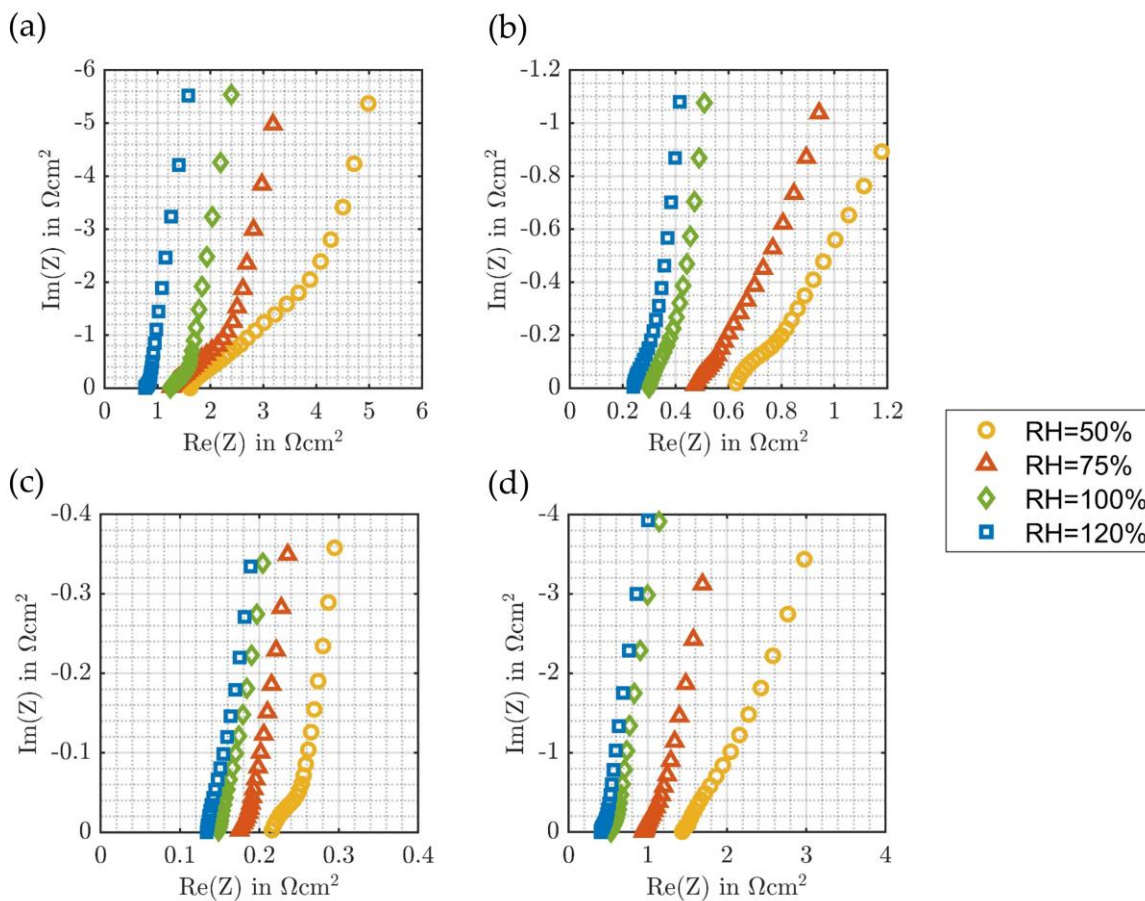
Figure 4.5 Nyquist plots over the RH range of 50 − 120 % at an applied potential of 0.2 V for PCLs with an I/C ratio of : a) I/C=0.3, b) I/C=0.6, c) I/C=1.0, and d) I/C=1.4.

4.3.3 PCLs effective ionic conductivities and comparison of EIS and hydrogen pump setup.

The effective ionic conductivity of PCLs with different I/C ratios is plotted in **Figure 4.7a**. A clear trend is observed, where effective ionic conductivity increases with increase in ionomer content and RH. Effective ionic conductivity increased 3.5-21 times when RH increased from 50 % to 120 %. The largest increase in conductivity was observed for I/C of 0.3, where effective ionic conductivity was 7×10^{-5} S/cm for RH of 50 % and increased to 1.5×10^{-3} S/cm for RH

of 120 %. For I/C of 1.4, a smaller increase in effective ionic conductivity was observed, from 8.96×10^{-3} S/cm at 50 % RH to 3.29×10^{-2} S/cm at 120% RH. For a constant RH the largest increase in effective ionic conductivity was observed at 50 % RH, where effective ionic conductivity increased form 7×10^{-5} to 8.96×10^{-3} S/cm when I/C increased from 0.3 to 1.4.

Figure 4.5b displays the effective conductivities measured by EIS data fitting with TLM and that measured with AC hydrogen pump (HP) set-up reported by our earlier study, here referred as AC HP [90]. In that study, as shown by **Figure 4.1a**, the PCLs were sandwiched between two membranes and hydrogen pump experiment was conducted where hydrogen is reacted on the anode to form protons which are transported across the membrane-PCLs-membrane assembly, and finally recombined into H_2 on the cathode side. Both DC and AC methods were used to fit the data in the HP set-up and they showed good agreement. Here we replot only the AC data from our earlier work, Sabarirajan et al. [90] and omit DC HP data, for the purpose of being concise. A large discrepancy between EIS and AC HP results is observed at low RH, and the effective ionic conductivity measured by EIS is 10 - 65 times higher than that measured by AC HP. At high RH condition, EIS measured conductivity is about 0.5 - 3 times that of AC HP measurements. For example, for PCL with I/C of 0.6, with RH increased from 50 % to 120 %, EIS measured effective ionic conductivity increased from 4.26×10^{-4} S/cm to 2.46×10^{-3} S/cm. In contrast, AC HP measured effective ionic conductivity increased from 3.83×10^{-5} S/cm to 4.82×10^{-3} S/cm. For the highest I/C of 1.4, EIS measured effective ionic conductivity increased from 8.96×10^{-3} S/cm to 3.29×10^{-2} S/cm with RH increased from 50 % to 120 %. And AC HP effective conductivity increased from 1.45×10^{-4} S/cm to 1.06×10^{-2} S/cm.

Figure 4.7c shows the ratio between the EIS and AC HP effective conductivity values. **Figure 4.6** shows this ratio on the logarithmic scale.
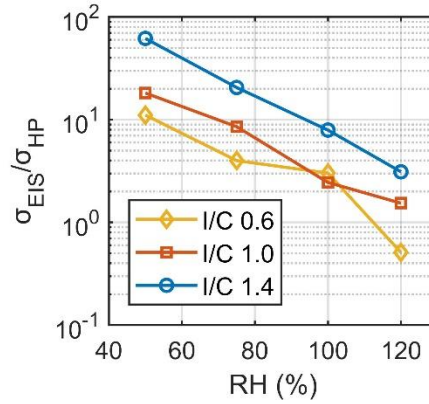
Figure 4.6 The ratio of effective ionic conductivities as a function of RH on the log-scale.

At high RH the ratio approaches the value of 0.5-3. This is indicative that the two methods converge at high RH. However, as RH is decreased the ratio between the two conductivity measurements increases, for example, at 75 % RH for I/C 0.6, 1.0 and 1.4 the conductivity ratios are 4, 8.56 and 20.6, respectively. Whereas for RH of 50 % the effective ionic conductivity ratios were 11.1, 18.2 and 61.9, respectively.

The definition of effective ionic conductivity is as following:

$$\sigma_{eff} = \frac{\epsilon}{\tau}\sigma \tag{47}$$

where, σ is the bulk conductivity, ϵ is the volume fraction of ionomer in PCL which can be determined according to A. Gasteiger et al's work [85] and τ is the tortuosity factor. The same

95

type of ionomer was studied, i.e. bulk conductivity σ is the same for EIS and HP, therefore, we can represent the ratio between the two effective ionic conductivities as:

$$\frac{\sigma_{EIS}}{\sigma_{HP}} = \frac{\epsilon_{EIS}}{\epsilon_{HP}} \frac{\tau_{HP}}{\tau_{EIS}} \tag{48}$$

where, $\frac{\epsilon_{EIS}}{\epsilon_{HP}}$ is equal to 1, as in both HP set-up and in this conventional set-up the equilibration time was sufficiently high for ionomer RH to be at equilibrium with the inlet gas RH. As we will explain in the next paragraph, the HP technique captures only transport in ionomer that is effectively connected through the full thickness of the PCL. The ratio of tortuosity factors, $\frac{\tau_{HP}}{\tau_{EIS}}$ again is related to the degree of ionomer connectivity and we will explore this next.

Figure 4.7d, **Figure 4.7e**, and **Figure 4.7f** showed the tortuosity factors calculated by using the effective ionic conductivities measured by EIS and AC HP under 50% RH and 100% RH for I/C=0.6, I/C=1.0 and I/C=1.4 respectively. At low RH, tortuosity factors of AC HP were much greater than those of EIS since the dead-end ionomer segments were not detected by AC HP method, and only the ionomers connected through the whole layer provide effective ion transport pathways. In contrast, all the ionomer segments in contact with the membrane are able to transport ions and thus detected by the EIS method (**Figure 4.8**). At high RHs, water helps to increase the connectivity of ionomers and results in a decreased tortuosity. As a result, the discrepancy in effective ionic conductivity between the two methods becomes smaller. The results suggest that increasing the ionomer connectivity is crucial to achieve low tortuosity of ion

transport pathways and thus to reach higher effective ionic conductivities. The connectivity of ionomers increases with I/C ratio and RH.
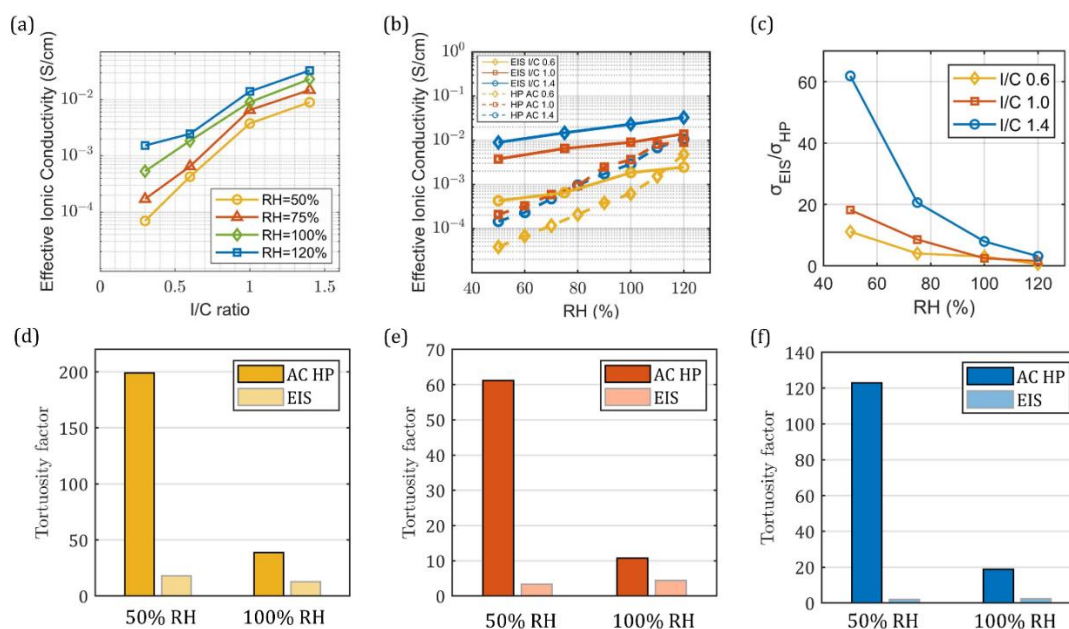
Figure 4.7 a) Effective ionic conductivity for PCLs for a range of I/C ratios and RH from 50 to 120 %, b) comparison of PCLs effective ionic conductivity measured by EIS (solid line) and AC HP (dash line), where the AC HP data is reproduced from our earlier study [90], c) the ratio between the PCLs effective ionic conductivities measured by EIS and HP as a function of RH. Tortuosity factors calculated by using effective ionic conductivities of PCLs measured by EIS and AC HP under 50% RH and 100% RH for d) I/C=0.6 e) I/C=1.0 f) I/C=1.4

Figure 4.8 shows the schematic of experimental set-ups for AC HP and EIS measurements. In the AC HP measurement (**Figure 4.8a**), hydrogen was used on both the anode and cathode sides, and a DC voltage from OCV to -0.4 V was applied across the cell. In the HP DC set-up, for protons to be measured as current they must completely cross the PCL from the anode to

cathode. Therefore, as shown by **Figure 4.8a**, if the ionomer pathways are not effectively connected through the PCL then protons will not readily conduct through these sections, then those ionomer segments will not be detected. These dead-end pathways will increase the tortuosity factor in the DC method. The loss of connectivity is especially pronounced at low RH and low I/C ratios, where ionomer regions are no longer connected by liquid water. Gostick and Weber [91] have shown that in a typical resistor network model of ionomer mixed with non ionically conductive support, ions flow through only very few preferential ionomer pathways. In the EIS measurement set-up (**Figure 4.8b**), protons will be transported through all of the ionomer in contact with the membrane. In the EIS measurement the ionomer does not need to be effectively connected through the whole thickness of the catalyst layer. As the schematic shows, the difference between the HP and EIS methods is most pronounced at low RH, and it has been confirmed by effective ionic conductivity measurements.
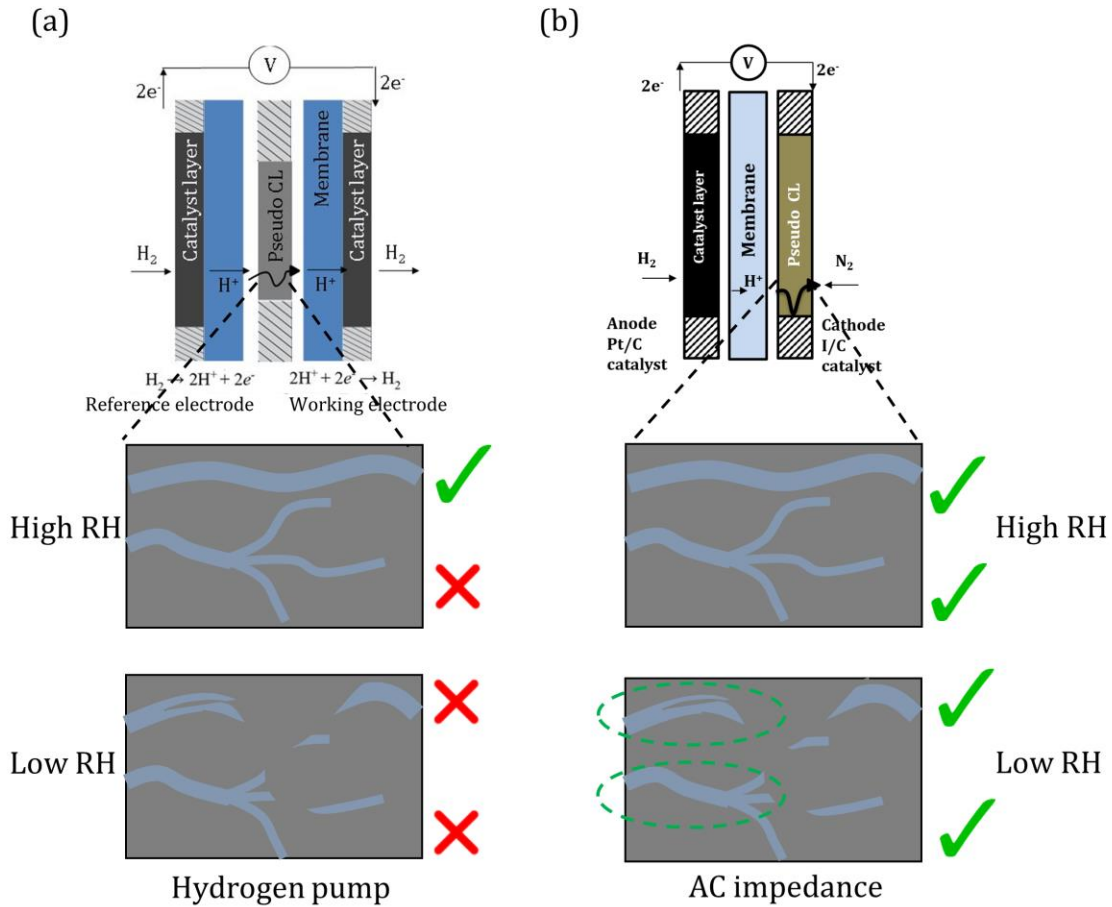
Figure 4.8. Schematics of a) AC or DC HP and b) EIS experimental set ups and a representative schematic of ionomer percolation through the PCLs at low and high RH.

Thus, the question arises: which tortuosity and effective ionic conductivity should be used within the fuel cell models to accurately represent catalyst layer properties? Recent computational work by Cooper and co-authors [92] similarly compared equivalent to our HP DC method (called restricted diffusion method eRDM) and AC method (called symmetric cell method (eSCM)) using battery electrodes. They similarly pointed out the difference between the two methods is mostly in counting or not counting dead-ended pores in their case and ionomer segments in our study. They concluded that the AC method (eSCM in their study) is more accurate, as for battery

to function one does not need pores (filled with electrolyte) connectivity through the layer. Fuel cell catalyst layers need both protons and oxygen reactants that come from different sides of the catalyst layer for the ORR to occur, thus the conclusion of which tortuosity factor to use or which method is more precise is not as straight forward.

4.3.4   2D cross-section Multiphysics model

Here, we used a 2D cross-section multiphysics model of PEFC reported previously [77] to simulate PEFC polarization behavior for 10 µm thick catalyst layer with I/C of 1 and RH of 50 and 75 %. As shown in **Figure 4.9**, at both RHs, the current density is higher when σ_{EIS} was used in the model. For example, at 50 % RH, it increases from 0.74 A/cm^2 to 1.08 A/cm^2 at 0.4 V when σ_{HP} and σ_{EIS} were used in the model, respectively. The only difference in the models is the effective ionic conductivity of the cathode catalyst layer. Therefore, the increase in the current densities is due to the lower ohmic loss in the cathode catalyst layer when σ_{EIS} was used. Similarly, the current density increases from 50 % RH to 75 % RH for both methods due to the increased effective ionic conductivity. At 50 % RH, σ_{HP} is very low and the current density is primarily limited by ion transport in the cathode catalyst layer. As a result, when RH increases from 50 % to 75 %, the current density increased significantly. As a comparison, when σ_{EIS} was used in the model, current density only increases a small amount when RH increases from 50 % to 75 %. The reason is that in this case the ion transport is no longer the limiting factor, though the ohmic loss is still reduced when effective ionic conductivity increases.

Volume-averaged models utilize effective ionic conductivity values. These can be either directly fit for different temperatures and RHs, or they can be expressed as inherent ionomer conductivity

adjusted with ionomer volume fraction and tortuosity, which will become effective ionic conductivity. Thus, if the EIS measurement is used, and the appropriate fits are created for the model to use then the model will most likely overapproximate the fuel cell performance because volume-averaged modeling approach does not account for the portion of the catalyst layer, where ionomer did effectively connect through, and hence where Pt will not be connected via ionomer or water domains (especially at low RH operating conditions). The DC method will almost certainly under-approximate fuel cell performance, however, it is a good metric for the through-thickness catalyst layer effective ionomer connectivity. More work is required to properly integrate these effective ionic conductivity measurements into the fuel cell model, here we provided just a very basic illustrations of impact of effective ionic conductivity on polarization behavior of the PEFC. An alternative approach would be to computationally measure the EIS spectra in the model and fit the experiment data.
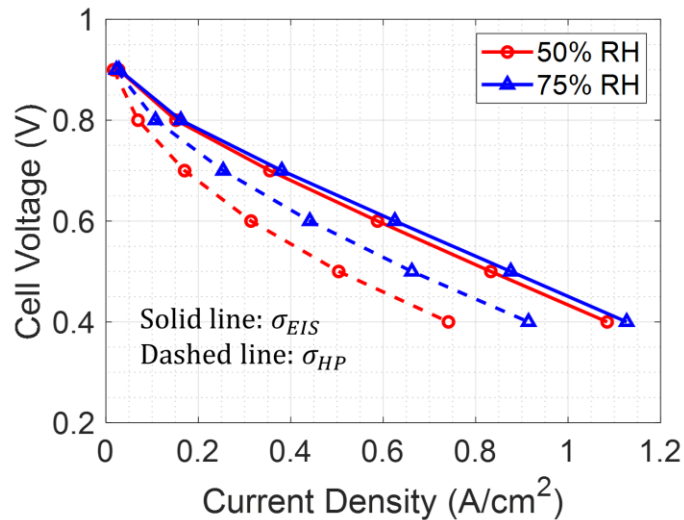
Figure 4.9 Polarization curves from PEFC model for I/C = 1 at 50 % and 75 % RH by using the effective ionic conductivity from EIS and HP AC measurements. A significant

difference in current density is observed, which is due to the much higher effective ionic conductivity.

4.3.5 Comparison of effective ionic conductivity and double layer capacitances between Pt/C catalyst layers

Effective ionic conductivities for Pt/C catalyst layers were measured. For each MEA, three cells were built and tested, repeated experiments and fittings were conducted. GrC carbon support (MEA 1 and MEA 2) has almost no internal porosity which results in a low total surface area and all the Pt particles distributes on the surface of the support. For MEA 3, according to Nagappan et al. [93], high surface area carbon (HSC) support has around 3-5 times higher total surface area than Vulcan carbon support due to its high internal porosity. **Figure 4.13a** shows the effective ionic conductivities for MEA 1 and MEA 2. The Nyquist plots at 0.2 V and corresponding equivalent circuit fits are shown in **Figure 4.11** and **Figure 4.12**. The error bars in **Figure 4.13a** show the variations of three measurements. MEA 1 and MEA 2 has same GrC support but different I/C ratios and Pt loadings. Effective ionic conductivity measurements for applied potentials from 0.2 to 0.6 V are shown in **Figure 4.10**.
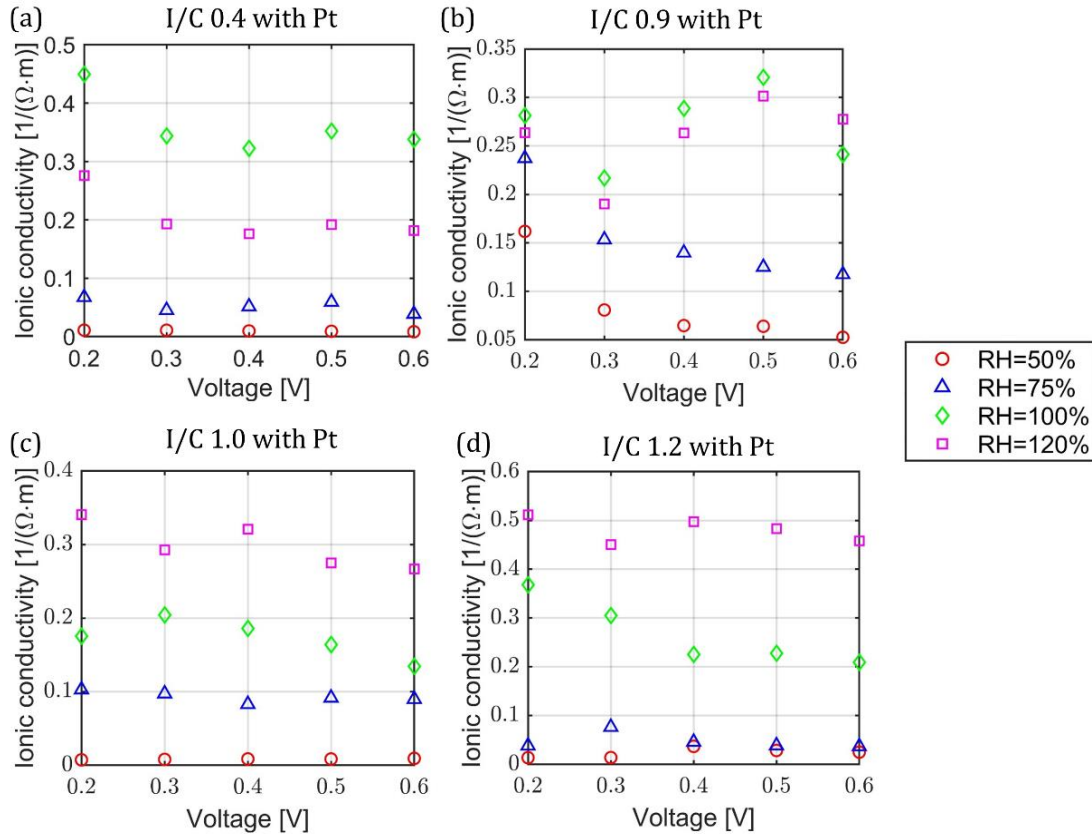
Figure 4.10 Ion conductivity for a) I/C=0.4 b) I/C=0.9 c) I/C=1.0 d) I/C=1.2 at four different relative humidity of 50%, 75%, 100% and 120%

The following trend in effective ionic conductivity is observed: MEA 1 (I/C = 0.4) < MEA 2 (I/C = 0.9). One reason is that the ionomer connectivity is lower at low I/C ratios. Another reason is that at lower I/C ratios, carbon agglomeration was observed using small angle x-ray scattering [30], which increases ionomer tortuosity. The remaining of the trend is dictated by the ionomer distribution disturbance by smaller meso-pores. **Figure 4.13c** shows the double layer capacities calculated by Eq.(7) for MEA 1 and MEA 2 at 100% RH. Double layer capacity at a specific RH depends on both I/C ratio and carbon support. MEA 1 with I/C ratio of 0.4 showed the lowest double layer capacity of 46 mF/cm² due to lower ionomer content and lack of the carbon

support's internal pores. MEA 2 with I/C 0.9 showed slightly higher double layer capacity of 51 mF/cm^2 compared to MEA 1.

Figure 4.13b shows effective ion conductivities for MEA 2 and MEA 3. The Nyquist plots at 0.2 V and corresponding equivalent circuit fits are shown in **Figure 4.11** and **Figure 4.12**.
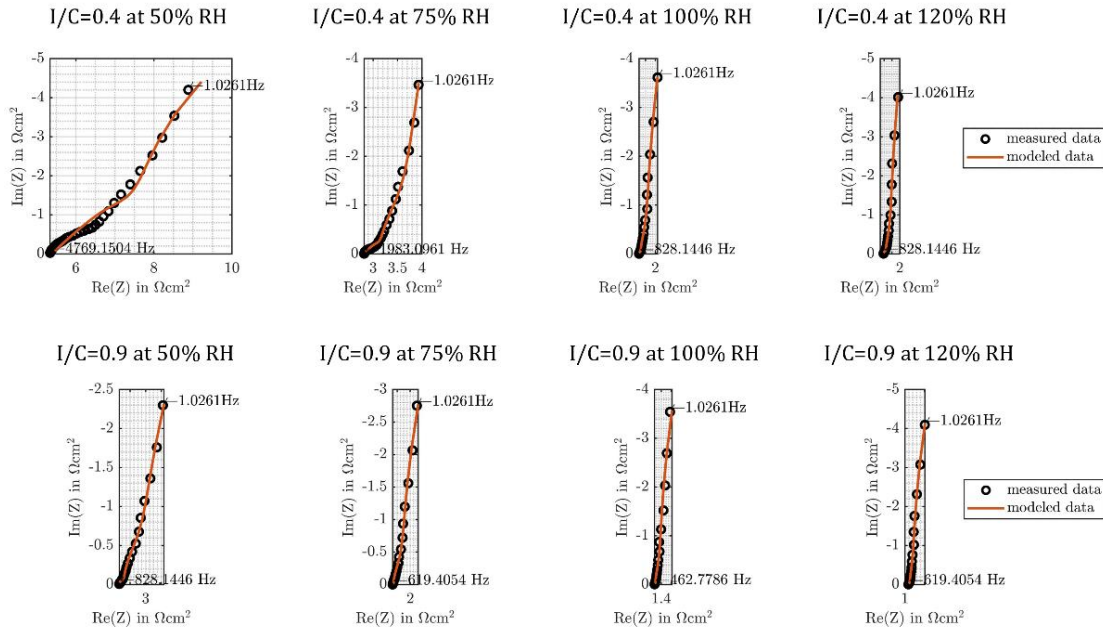
Figure 4.11 TML fitting for I/C=0.4 and I/C=0.9 Pt/C catalyst layer at 50%, 75%, 100% and 120% RH
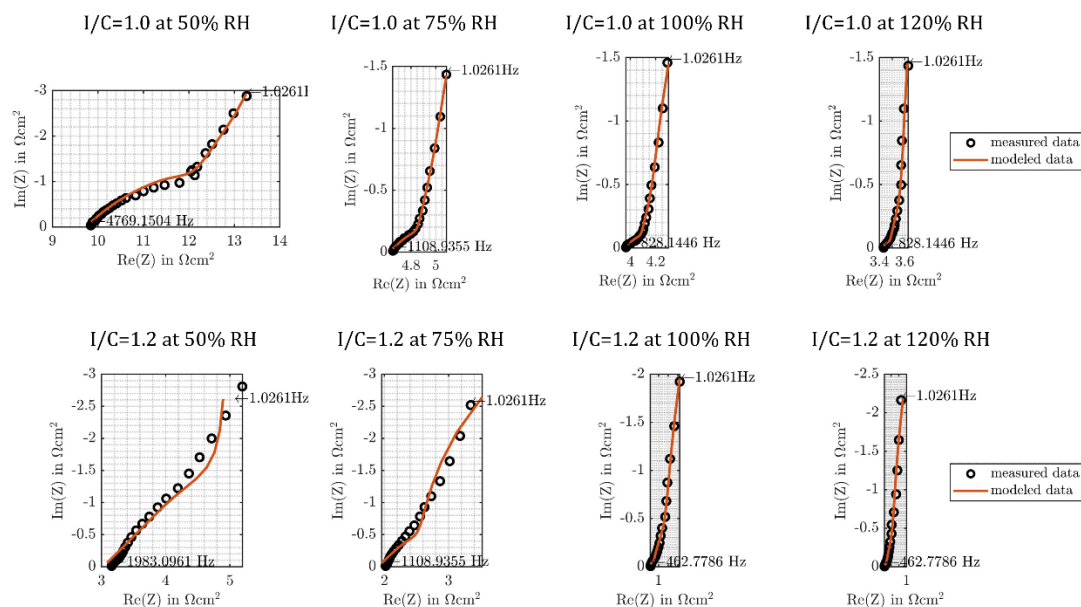
Figure 4.12 TML fitting for I/C=1.0 and I/C=1.2 Pt/C catalyst layer at 50%, 75%, 100% and 120% RH

MEA 2 and MEA 3 have similar I/C ratios around 1 and Pt loadings around 0.21-0.24 mg/cm^2, but different carbon supports. At low RH, MEA3 with HSC showed lower effective ionic conductivity. It was shown recently by Ramaswamy et al. [93] that surface area of smaller meso-pores (> 8 nm) of the carbon support determines the continuity and uniformity of the ionomer distribution in the catalyst layer. The GrC carbon support in MEA2 has less meso-pores comparing the HSC in MEA3, which results in a larger effective ionic conductivity of MEA2. At high RHs, for MEA 3 with HSC support, internal pores filled with water results in a better continuity of ionic pathways and creates more ionic pathways specially for those Pt particles inside of internal pores of HSC support. And a smaller discrepancy of effective ionic conductivity between MEA 2 and MEA 3 was observed. **Figure 4.13d** shows the double layer capacities for MEA 2 and MEA 3 with 100 % RH condition. MEA 3 showed higher double layer capacity of 119 mF/cm^2 at 100 % RH. This is due to a higher accessibility of Pt in the smaller

105

meso-pores also due to contribution of carbon, especially the internal micro- and meso-pores of the carbon support that interface with water. This is due to a higher accessibility of Pt in the smaller meso-pores also due to contribution of carbon, especially the internal micro- and meso-pores of the carbon support that interface with water. This is due to a higher accessibility of Pt in the smaller meso-pores also due to contribution of carbon, especially the internal micro- and meso-pores of the carbon support that interface with water. MEA 2 with GrC support showed lower double layer capacity since the absence of inside pores.
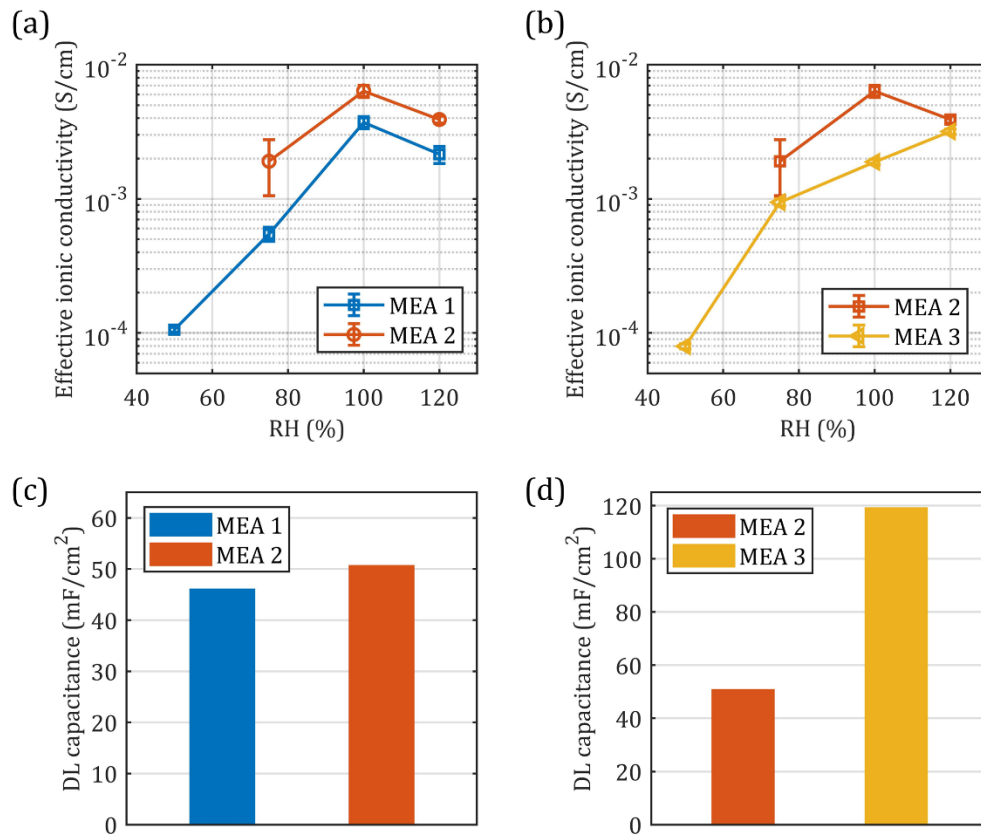
Figure 4.13 a) Effective ionic conductivities for catalyst layers of MEA 1 and MEA 2 in the RH range from 50 % to 120 % b) effective ionic conductivities for catalyst layers of MEA 2 and MEA 3 in the RH range from 50 % to 120 % c) double layer capacitances for catalyst

layers of MEA 1 and MEA 2 at 100 % RH. d) double layer capacitances for catalyst layer of MEA 2 and MEA 3 at 100 % RH.

4.3.6 Comparison of effective ionic conductivity between PCL and Pt/C catalyst layer

Figure 4.14 shows the effective ionic conductivities comparison between PCLs (without Pt) with I/C ratio of 0.3 and 1.2 and Pt/C layer (MEA 1 and MEA 4 in Table 1) with I/C ratio of 0.4 and 1.2 with same Vulcan XC72 support under different RH conditions from 50% RH to 120% RH. For each I/C ratio, three cells were built and tested. Three repeated experiments and fittings were conducted and the variations were evaluated and shown by the error bars. For low I/C ratio of 0.3-0.4 (**Figure 4.14a**), effective ionic conductivity for the PCL increased from 1.18×10^{-4} S/cm at 50 % RH to 1.79×10^{-3} S/cm at 120% RH, whereas Pt/C layer effective ionic conductivity increased from 1.03×10^{-4} S/cm at 50 % RH to 2.26×10^{-3} S/cm at 120 % RH. Above 55 % RH, Pt/C layer has higher effective ionic conductivity because the Pt particles are hydrophilic and the surrounding water helps to increase the connectivity of ionomers.

Figure 4.14b shows the effective ionic conductivities comparison for high I/C radio of 1.2. Effective ionic conductivity of the PCL increased from 5.76×10^{-4} S/cm at 50 % RH to 1.94×10^{-3} S/cm at 120% RH, whereas Pt/C layer effective ionic conductivity increased from 2.11×10^{-4} S/cm at 50 % RH to 4.97×10^{-3} S/cm at 120 % RH. The effective ionic conductivities intersects at around 90 % RH. At 120 % RH Pt/C layer has 2.2 times higher effective ionic conductivity than PCL, whereas at 50 % RH it is 2 times lower. Below 90% RH, PCL has higher effective ionic conductivity than Pt/C layer and this is due to ionomer dispersion

in the ink. The presence of Pt nanoparticles reorients ionomer also changes the size of agglomerates, resulting in the effective ionic conductivity change. And in the full range of RH, effective ionic conductivities of Pt/C layers experience a greater increase compare to PCLs due to hydrophilicity of Pt particles, in other words, more water content is attracted to Pt particles and help proton transport. Which result in between 50% RH to 90% RH, the effective ionic conductivities of Pt/C layers are greater than those of PCLs.
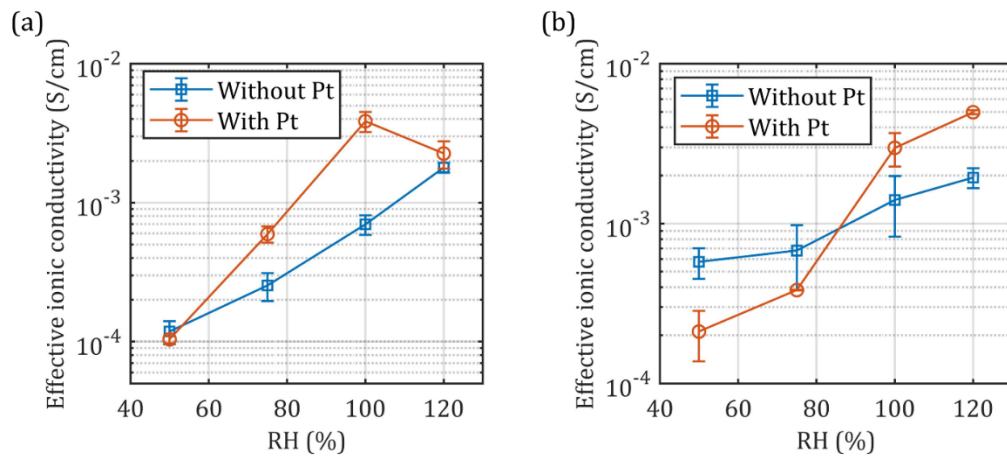
Figure 4.14 Effective ionic conductivity comparison between PCL (without Pt) and Pt/C layer (with Pt) with a) low I/C ratio b) high I/C ratio in a RH range from 50 % to 120 %.

4.4 Conclusion

PCLs ion conductivities were measured in a conventional PEFC set-up, using EIS collected in H_2/N_2 environment and a RH range from 50 to 120 %. The EIS was fitted with the TLM for the PCLs with I/C 0.3, 0.6, 1.0, 1.2 and 1.4. PCLs effective ionic conductivity increased with I/C ratio and RH because ionomer and water provided more ionic pathways for proton transport. Ion conductivities measured using EIS and previously reported with AC HP method were compared for the PCLs with I/C of 0.6, 1.0 and 1.4. In AC HP set-up, only ionomer that is effectively

connected through the full catalyst layer thickness carries proton current. The remaining of the ionomer pathways that are dead-ended increase tortuosity factor but do not carry current. However, for the EIS measurements, ionomer does not need to be connected all the way through the PCL, if ionomer is in contact with membrane it will be proton current carrying. The ratio of the effective conductivities between the EIS and AC HP increased with I/C ratio and decreased with RH. The highest ratio of effective ionic conductivities was found at 50 % RH, which increased from 10 to 65 when I/C increased from 0.6 to 1.4. For RH of 120 %, oversaturated conditions, where liquid water is expected to condense, the ratio between the two effective conductivities differ by a ratio of 0.5 to 3. In fully saturated conditions ionomer connectivity will be high, and the two techniques should show similar results. However, in the low RH condition, more ionomer will be disconnected in both methods, as fewer water bridges exist between the ionomer clusters. Therefore, the difference in effective ionic conductivity and thus ionomer tortuosity are more pronounced at low RHs.

Mathematical modeling of the fuel cell has been conducted by using the effective ionic conductivities from EIS and AC HP methods for 50 % and 75 % RH. We observed the current density at 0.4 V increased from 0.74 A/cm^2 to 1.08 A/cm^2 at 50% RH when σ_{HP} and σ_{EIS} were used, respectively. Therefore, it is critical to input the correct effective ionic conductivity which can be representative of the ion transport process in the catalyst layers as these volume-average approaches apply single effective conductivity through the whole catalyst layer.

Furthermore, we measured double layer capacitances and effective ionic conductivities with the EIS method for Pt/C catalyst layers with HSC and GrC supports and different I/C ratios for RH

range from 50 to 120 % to emphasize the effect of I/C ratio, RH, and carbon support. Overall, with the same carbon support, the higher I/C ratio resulted in the higher double layer capacitance and effective ionic conductivity. Besides, catalyst layer with GrC showed the highest effective ionic conductivity but lowest double layer capacity due to lower internal porosity which results in a lower total surface area. In this case, all the Pt particles are distributed on the surface of the GrC support, and a better ionomer continuity and ionic pathways could be created due to lack of internal pores. In contrast, HSC showed lower conductivity but highest double layer capacity because HSC support had very high internal porosity which resulted in worse ionomer continuity.

The effective ionic conductivities of PCLs were compared to those of Pt/C with the same carbon support for low I/C ratio and high I/C ratio. For both cases, it was shown that at high RH, effective ionic conductivities of Pt/C layer are larger than those of PCLs and it is due to the hydrophilic Pt retains more water which helps proton transport.

Chapter. 5 High O_2 permeability ionomer for improved PEM fuel cell performance and electrochemical characterizations

5.1 Introduction

Development of highly active Pt-alloy nanoparticle catalysts for the oxygen reduction reaction (ORR) has led to low Pt loadings < 0.1 mg cm^{-2} at the cathode.[94–96] At low current densities these catalysts achieve high mass activities > 0.44 A mg$_{Pt}^{-1}$, but may fail to meet the high current density requirements of >1.5 A cm^{-2}. Several studies have shown that local O_2 transport resistance ($R_{O2,local}$) at or near the Pt surface leads to large voltage losses at high current densities for electrodes with low Pt loadings in the cathode catalyst layer. [18,64,97–100] Pressure-independent O_2-transport resistance is believed to be mainly due to parallel alignment of the ionomer backbone next to the Pt, blocking oxygen transport. [47,101,102] Perfluorinated sulfonic acid (PFSA) ionomers form a dense, nanometer thin film around the electrocatalyst in the catalyst layer.[74] As the Pt loading decreases, the local O_2 flux increases per active site of Pt, exacerbating transport losses. [18,103] Furthermore, sulfonic acid groups adsorb onto the electrocatalyst, poisoning it, resulting in lower electrocatalytic activity toward the ORR. [47] Therefore, for PEMFCs to reach their cost and performance targets, new high oxygen permeability ionomer (HOPI) chemistry is required for integration into catalyst layers. Katzenberg et al. [104] used a perfluoro (2-16 methylene-4-methyl-1,3-dioxolane) (PFMMD) backbone showing reduced domain swelling under hydration, significantly improving gas

permeability, but the power density of the fuel cells was not evaluated in greater detail. Shimizu et al. [105] used two types of HOPIs that showed an improvement of 150 mV in cell voltage at 1.5 A cm^{-2}, but the catalyst layers had low durability.

Here, Giner synthesized and integrated novel HOPIs called PDD ionomer into PEMFC catalyst layers to form high power-density membrane electrode assemblies (MEAs). Giner systematically evaluated the ionomer's oxygen permeability and ion conductivity, as well as the ionomer's interaction with Pt and carbon.

Figure 5.1 shows oxygen transport for MEAs with novel PDD ionomer and commercial Nafion ionomer. Oxygen transport is much harder and tortuous in commercial Nafion ionomer due to the extremely low gas permeability and diffusivity of PTFE backbone. However, in MEAs with PDD ionomer, gas transport is much more straightforward because of the porous backbone.
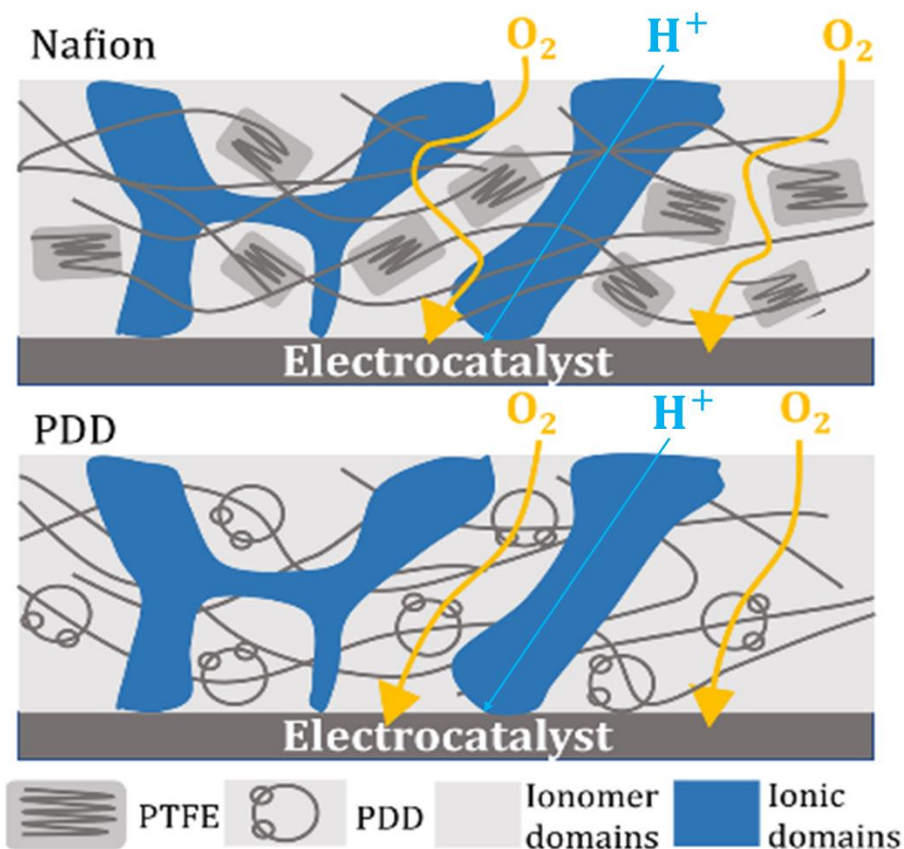
Figure 5.1 Oxygen transport in catalyst layers with different ionomers, a) Nafion, b) PDD

5.2 Results

5.2.1 Polarization curve and power density results

MEA performance were shown in **Figure 5.2**, **Figure 5.2b** showed these MEAs polarization

performance at 80 ℃, 100 % RH and 150 absolute back pressure using fixed 1.5/3 SLPM H_2/air.

All MEAs showed around 0.96-0.97 V at their OCVs due to less oxidation by cross over H_2.

PDD MEAs showed better performance at entire current range especially at high current density

region (2-2.5 A cm^{-2}). At 2.5 A cm^{-2}, PDD 1, PDD 2 and PDD 3 MEAs showed higher

voltages of 0.36 V, 0.491 V and 0.4 V respectively, compared to Nafion MEA's 0.27 V. All

MEAs showed similar HFRs, which had a range from 53 mOhms cm^2 to 64 mOhms cm^2. PDD

2 had the best performance, which was also the only cell can reach 3 A cm^{-2} with a voltage of 0.23 V. According to results shown in **Figure 5.3**, power densities power density were displayed as a function of current density for these MEAs in **Figure 5.2b** All MEAs showed an linear increase of power densities at low current density region (0-1 A cm^{-2}), then the power densities reached highest values at around 0.4-0.6 V. Power densities then dropped at high current density region (2-2.5 A cm^{-2}) due to the mass transport limitation. All PDD MEAs showed higher power densities compared to commercial Nafion ionomer, and for PDD 2, it reached highest power density among these MEAs, around 1.25 W cm^{-2} at 0.56 V. For Nafion ionomer, it had the lower power density of 1 W cm^{-2} at 0.5 V.

Cell performance decreased after adjusting the fixed flow rate to stoichiometry flow rate with stoichiometry factors of 2/2 at anode/cathode respectively. With smaller flow rates, mass transport issue was pronounced for all MEAs. In performance plot shown in **Figure 5.2c**, PDD still shows much better performance at entire current density range. For PDD 2, it showed the best performance with the lowest HFR of 52 mOhms cm^2 and reached 2.5 A cm^{-2} at 0.35 V. PDD 1 and PDD 3 MEAs showed much similar performance, which both reached 2 A cm^{-2} at 0.5 V respectively. However, PDD 3 MEA had higher HFR of 58.5 mOhms cm^2, compared to PDD 1's 48.1 mOhms cm^2. For Nafion ionomer, the mass transport issue was pronounced at high current density, and it reached 2 A cm^{-2} at 0.32 V. Apart from that, it also showed the highest HFR of 58.8 mOhms cm^2. From power density plot shown in **Figure 5.2d**, the MEA with PDD2 ionomer reached a power density of 1.1 W cm^{-2} (using non-iR corrected voltage) compared to 0.8 W cm^{-2} using Nafion ionomer.
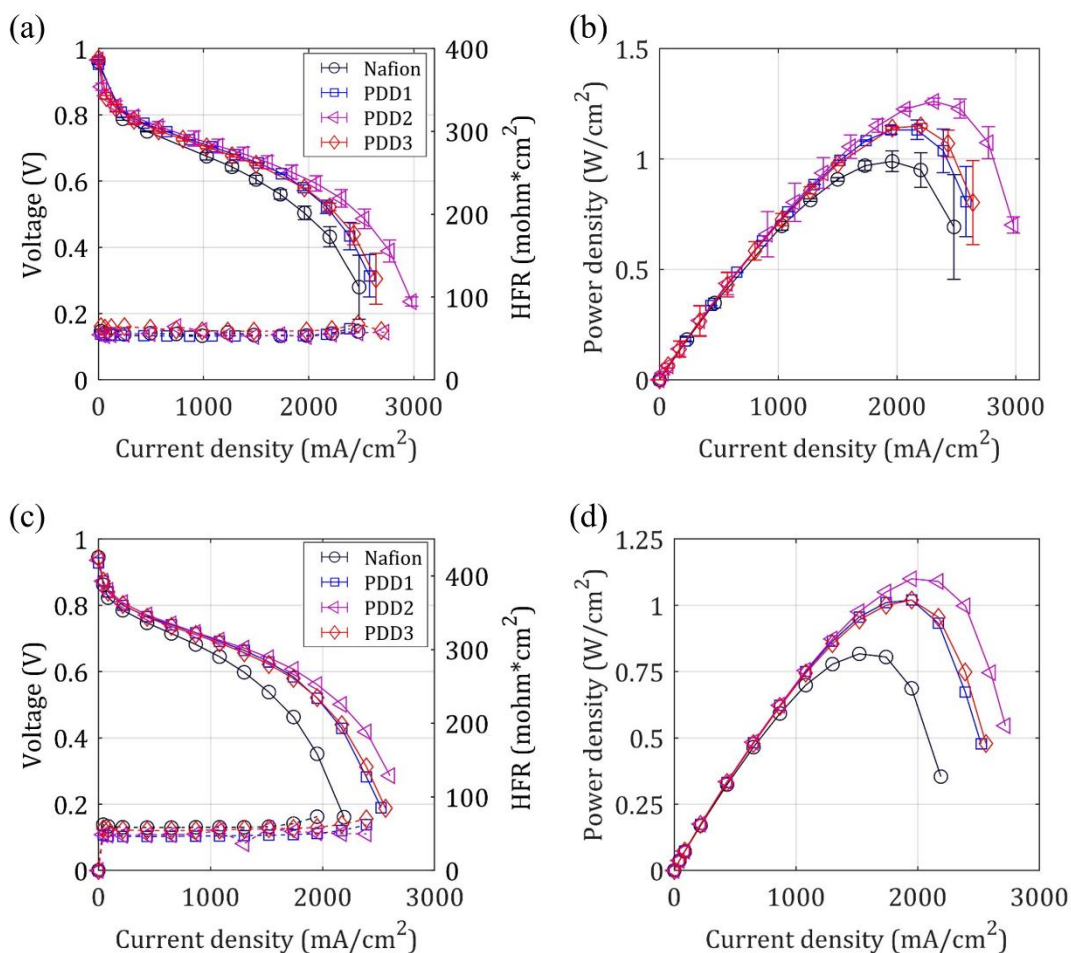
Figure 5.2 Cell performance for MEAs with PDD and Nafion, corresponding to a) polarization curves measurement at 80 °C, 100% RH, 150 kPa in H₂/Air with constant gas flow-rates of 1.5 and 3 SLPM b) power density at 80 °C, 100% RH, 150 kPa in H₂/Air with constant gas flow-rates of 1.5 and 3 SLPM c) polarization curves measurement at 80 °C, 100% RH, 150 kPa in H₂/Air with stoichiometric anode and cathode flows of 2/2. d) power density at 80 °C, 100% RH, 150 kPa in H₂/Air with stoichiometric anode and cathode flows of 2/2.

5.2.2   CO stripping, CV measurements and ECSAs

CV, CO displacement and CO stripping measurements were performed at 60 ℃ and 100 % RH without back pressure. According to CO stripping measurement result shown in **Figure 5.3a**, the

altitudes of CO stripping peaks are similar at voltage range from 0.5-0.75 V. Apart from that, CV measurement results showed similar H_{upd} peaks. With the knowledge of CV and CO stripping measurements results, ECSAs were calculated according to Eqn. (19) and (20) and shown in **Figure 5.3c**. Due to stronger absorbability of CO, ECSA results calculated using CO stripping were more accurate and higher than calculated by using H_{upd} peaks from CV results. Apart from that, ECSA measurement results using CO stripping peaks are usually 0-50 % higher than that calculated by using H_{upd} peaks. In this work, ECSA values for four MEAs showed similar values, and it showed around 35-45 m^2/g from H_{upd} peaks calculations and 50-60 m^2/g from CO stripping peaks calculations. ECSA ratios were also calculated by using $ECSA_{CO\ stripping}/ECSA_{HUPD}$. Nafion MEA showed highest ECSA ratio of around 1.35, while PDD MEAs showed lower ECSA ratios of around 1.15.
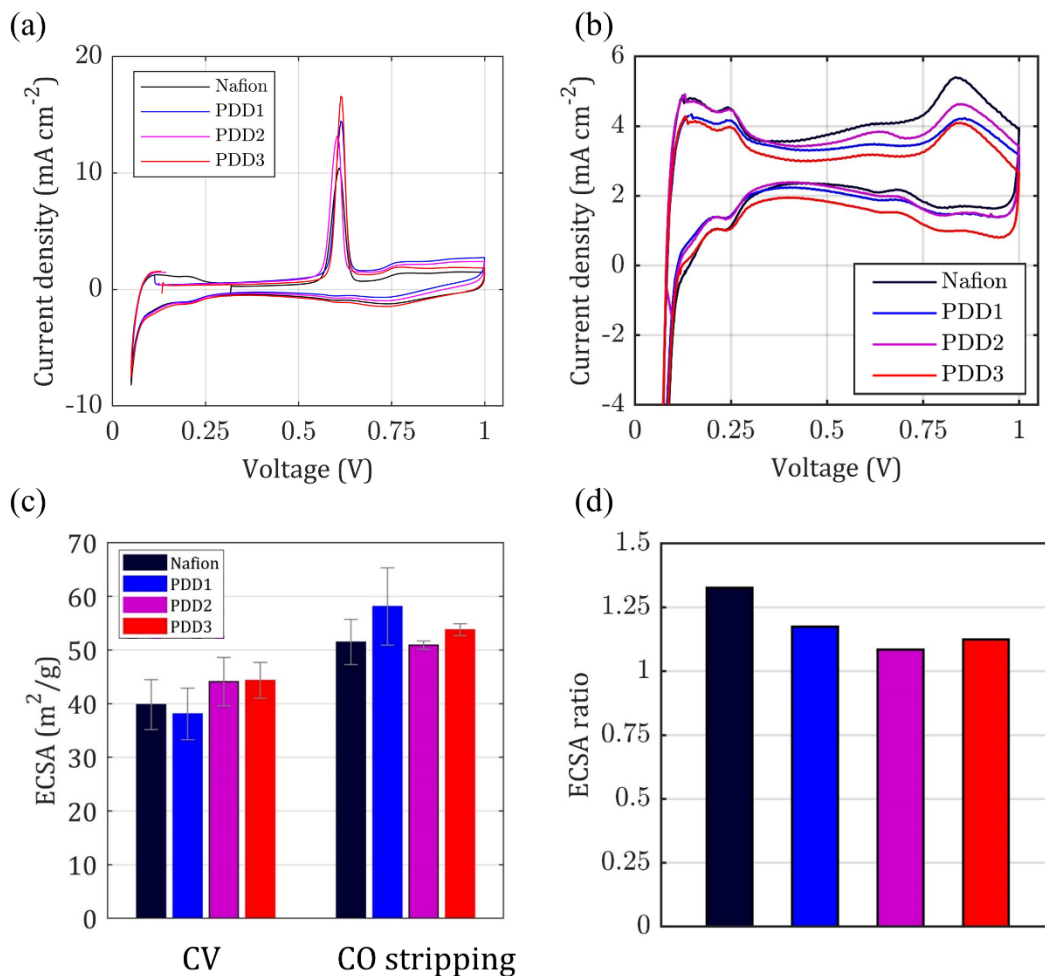
Figure 5.3 a) CO-stripping current (once integrated will become displacement charge for MEAs with PDD and Nafion ionomer, b) cyclic voltammetry current density for the four MEAs at 60 °C, 100 % RH without additional back pressure and c) calculated ECSA using H_{upd} and CO stripping charge d) ECSA ratio

5.2.3 Double layer capacitance, and coverages

Double layer capacitances were calculated according to Iden and Ohma's study at different operating condition, with CO and without CO, dry condition at 25 % RH, and wet condition at 100 % RH. As the result shown in **Figure 5.4**, at 100 % RH, all PDD MEAs showed higher double layer capacitances (48-51 mF/cm^2), which also indicated more surfaces are created at

117

solid/ionic material interface. All MEAs showed lower double layer capacitances (33-35 mF/cm^2) at dry condition due to the elimination of water's contribution. Not only at 100 % RH, Nafion MEA showed the lowest double layer capacitance at 25 % RH as well, which was around 26 mF/cm^2. According to the calculation method shown in previous chapter, four different interfacial capacitances were shown in **Figure 5.4**. All MEAs showed much higher Pt/ionomer interfacial capacitance (17.5-27.5 mF/cm^2) and similarly even capacitances for Pt/water, carbon/ionomer and carbon/water interfaces (5-12 mF/cm^2). PDD 2 showed highest Pt/ionomer contacts due to the highest capacitance value of 28 mF/cm^2, while Nafion ionomer shows lower Pt/ionomer contacts with an interfacial capacitance of 17.5 mF/cm^2. Coverages results are shown in **Figure 5.4**, both high ionomer on Pt coverage (65-88 %) and ionomer on carbon support coverage (59-79 %) were observed for all MEAs. It also turned out that water's contributions were similar for all these MEAs, which consisted of 10-36 % water on Pt coverage and 25-40 % water on carbon coverage. The most significant parameter, ionomer on Pt coverages, are quiet similar for these MEAs. PDD 2 showed the highest ionomer on Pt coverage of 88 %, and MEAs with Nafion, PDD 1 and PDD 3 ionomer showed similar coverages from 70-75 %.
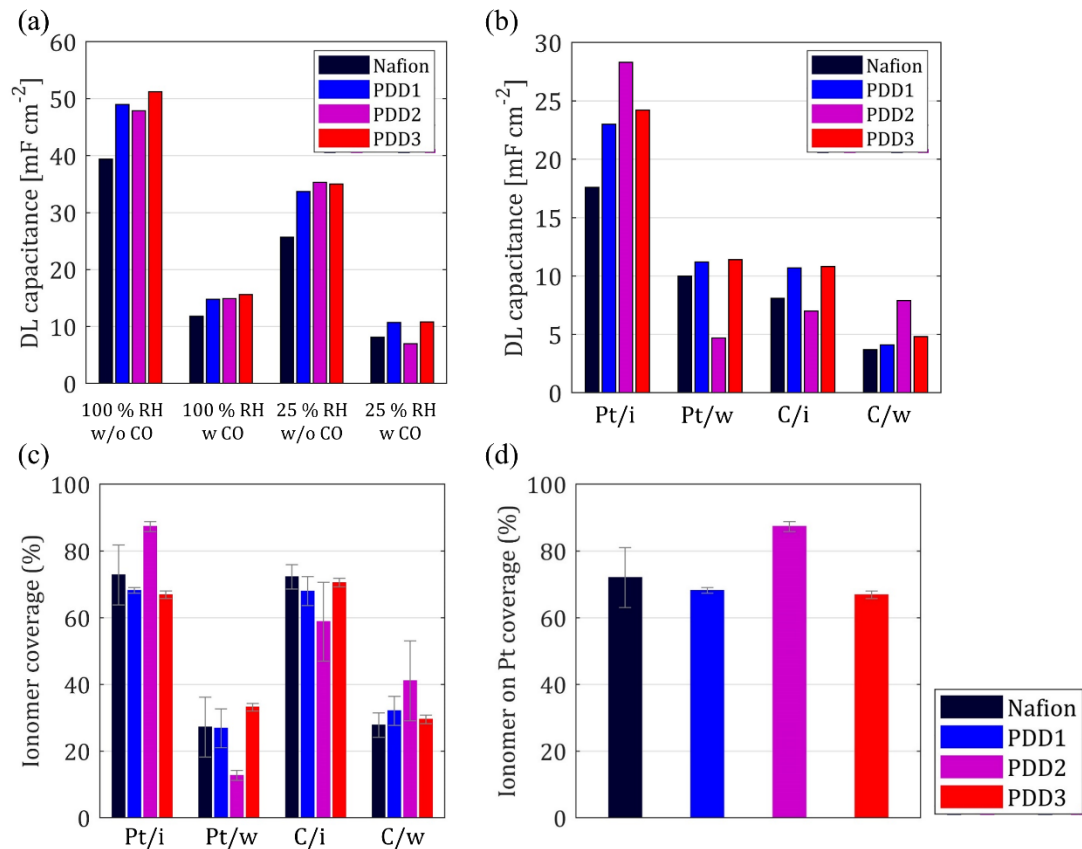
Figure 5.4 a) Double layer capacitance for MEAs with PDD and Nafion for four cases of 100 % RH and 25 % RH and with or without CO. b) Double layer capacitance that corresponds to Pt/ionomer (Pt/i), Pt/water (Pt/w), carbon/ionomer (C/i) and carbon/water (C/w) c) ionomer and water coverage on Pt and carbon d) ionomer on Pt coverage

5.2.4   Ionic conductivity and tortuosity

Catalyst layer ionic conductivities and tortuosity factors for four MEAs were calculated and shown in **Figure 5.5**. Higher tortuosity factor was considered as more tortuous proton pathways, which resulted in lower catalyst layer ionic conductivity and were represented as ohmic loss and higher HFRs in polarization curve plot. Here PDD 1 and PDD 2 MEAs showed lowest catalyst layer ionic conductivities of 0.005 S/cm and 0.0046 S/cm respectively. They also showed relatively higher catalyst layer tortuosity factors, with values of 2.25 and 2.9 respectively.

119

However Nafion ionomer and PDD 3 MEA showed higher ionic conductivities of 0.0063 S/cm and 0.006 S/cm respectively with lower tortuosity factors of 2.2 and 2.4.
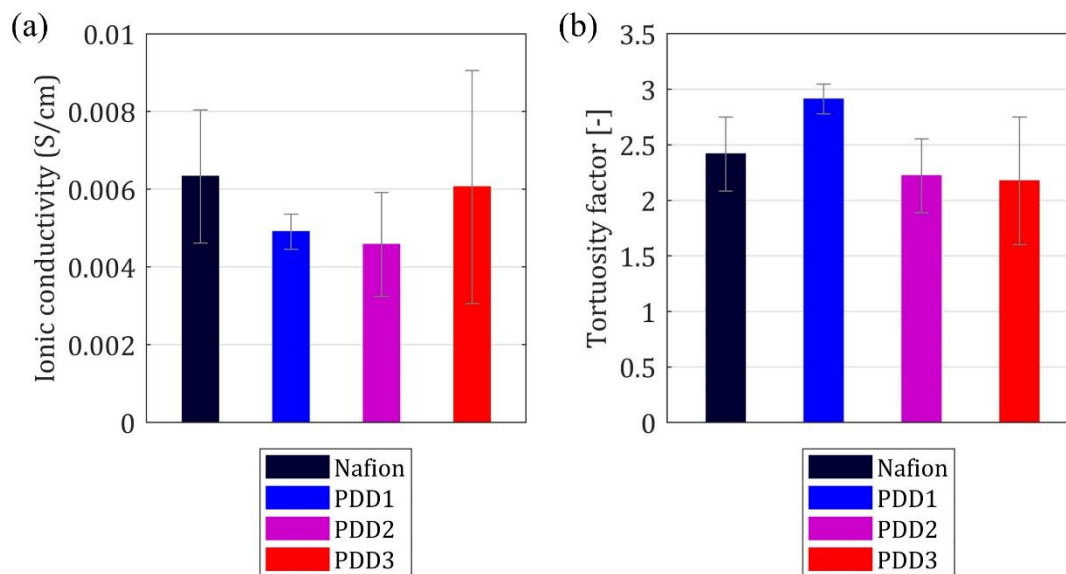
Figure 5.5 a) catalyst layer conductivity and b) tortuosity with PDD and Nafion ionomers at 100% RH.

5.2.5 CO displacement/stripping and SO_3^- coverage

CO displacement and stripping measurements were performed at 60 ℃, 100 % RH without back pressure. From CO displacement and stripping results shown in **Figure 5.6Figure** , all PDD MEAs showed similar CO displacement peak shapes and CO displacement charges around 31.5 mC, while Nafion ionomer showed lower CO displacement charge value of 28.7 mC. For CO stripping charge, PDD MEAs showed around 500 mC and Nafion MEA showed around 460 mC. The resulting SO_3^- group coverages ranged from 11 % to 15 %, and PDD MEAs showed relatively lower SO_3^- group coverage of 11% to 12.5 % and Naion MEA had the highest SO_3^- group coverage of 15 %.
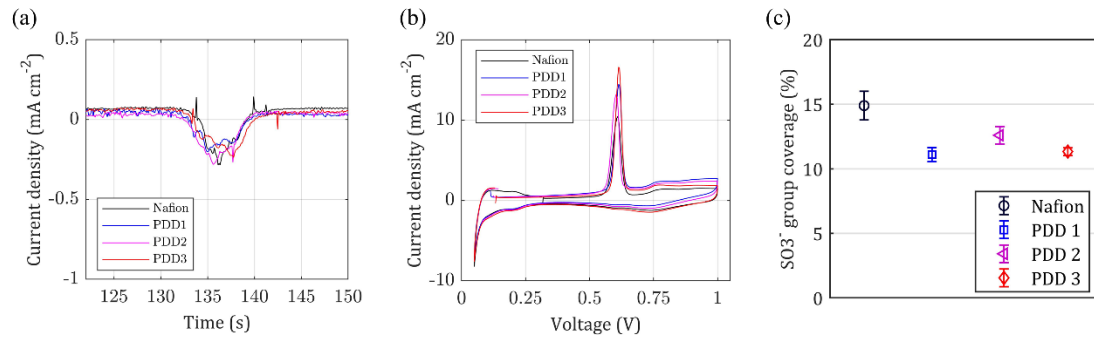
Figure 5.6 a) CO displacement b) CO stripping and c) sulfonic acid group coverage comparisons between MEAs using PDD ionomer and Nafion ionomer at 60 ℃ 100 % RH and without additional back pressure

5.2.6 Link polarization performance with SO_3^- coverage

Polarization performance results were plotted as a function of SO_3^- group coverage shown in **Figure 5.7**. For all PDD MEAs, cell performance at high current density increased with SO_3^- group coverage, which indicates porous PDD backbone mitigate mass transport issue. However for Nafion MEA, it had the highest SO_3^- group coverage but the worst performance since the extremely low gas diffusivity and permeability of PTFE crystals within the backbone.
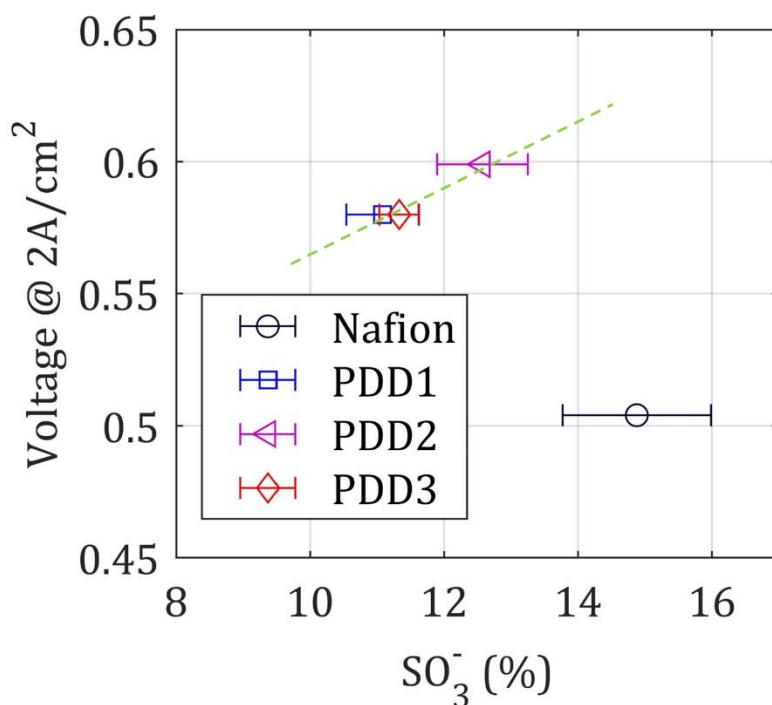
Figure 5.7 Sulfonic acid group coverage as a function of cell performance for MEAs using PDD ionomer and Nafion ionomer

5.3 Conclusion and discussion

PDD MEAs showed similar electrochemical characterizations compared to Nafion MEA. They showed similar ECSA values of 50 m^2/g according to CO stripping results, which were more accurate than results from CV measurements. However, similar ECSA results didn't result in closed polarization performance. With fixed H_2/air flow rates of 1.5/3 SLPM, PDD MEAs showed much better performance especially at high current density. At 2.5 A cm^{-2}, PDD 1, PDD 2 and PDD 3 MEAs showed higher voltages of 0.36 V, 0.491 V and 0.4 V respectively, compared to Nafion MEA's 0.27 V. Performance discrepancy was pronounced with stoichiometry flow rate of stoichiometry factor of 2/2. At 2 A cm^{-2}, PDD 1, PDD 2 and PDD 3

MEAs showed higher voltages of 0.5 V, 0.55 V and 0.5 V respectively, compared to Nafion

MEA's 0.32 V.

Not only ECSA, catalyst layer ionic conductivity results also proved PDD ionomer had good

proton accessibility in porous media with very small thickness. Also, similar HFR results showed

MEAs using PDD ionomer didn't have pronounced ohmic loss issue.

With the knowledge of ionomer on Pt coverage, PDD 2 MEA showed the highest coverage of

88 % and the best polarization performance, compared to Nafion MEA's second highest

coverage of 72 % but the worst cell performance. A clear evidence was shown as novel PDD

ionomer can have both high ionomer on Pt coverage and cell performance since mass transport

issue was mitigated. However for Nafion MEA, cell performance was more significantly limited

by ionomer coverage since the extremely low gas permeability and gas diffusivity of PTFE

backbone.

Chapter. 6 Determine Pt/ionomer interfacial properties using CO displacement/stripping methods.

6.1 Introduction

Reducing Pt use in PEFCs is one of the high-priority tasks for the fuel cell community but significant reduction can cause performance and durability penalties. Higher Pt loadings are currently used in the cathode catalyst layer compared to the anode due to sluggish kinetics of oxygen reduction reaction (ORR). Tafel analysis shows a 65 mV cell voltage loss (in an activation region of polarization curve) when cathode Pt loading is reduced by a factor of 10. [15] These losses are countered by several means: alloying Pt to enhance its activity, optimization of Pt particle size, improving ionomer conductivity, limiting ionomer poisoning of catalyst and optimizing the structure of the electrode.[9,106] A well-designed catalyst layer with low Pt loading is possible, if the interface between Pt and ionomer is optimized and oxygen transport is not overly inhibited by ionomer. [74] The distribution, optimization and continuity of perfluorosulfonated acid (PFSA) ionomer in a catalyst layer is critical because it provides proton accessibility and hydrophobicity to limit electrode flooding.[107,108] However, interaction between the Pt surface and the ionomer SO_3^- group, as shown by Kodama et al. [51], essentially leads to a loss of Pt activity known as "Pt poisoning."

Further studies investigated in-depth Nafion's SO_3^- group adsorption on Pt surface mostly using CO-displacement and stripping technique. Feliu and co-workers [52–55] first developed the technique of CO displacement/CO stripping to quantify anion adsorption within electrolyte at the Pt surface. Subbaraman et al.[44] extended the method to study the Nafion SO_3^- adsorption using a three-electrode setup in liquid electrolyte. Garrick et al.[56] was the first study to use CO displacement study in both rotating disk electrode (RDE) and membrane electrode assembly (MEA) setups. They also defined the SO_3^- group coverage calculation using the ratio of CO displacement and CO stripping charges. They found that when ionomer to carbon (I/C) ratio increased from 0.8 to 1.6 the SO_3^- groups coverage increased from 10 to 15 %. They have also shown that high surface area carbon supports had lower ionomer coverage compared to low surface area carbon. Van Cleve et al.[78] showed the independent relationship between SO_3^- group adsorption and Pt activity, which indicated that once Pt is poisoned by SO_3^- the additional poisoning does not impact Pt's activity. They studied Pt catalyst loadings of 0.05 to 0.3 mg/cm^2 and obtained SO_3^- coverages in a range of 16-26 %.

In this work, CO displacement and CO stripping techniques were performed in a membrane electrode assembly (MEA) setup. SO_3^- group coverages were calculated for the cells with various Pt loadings, ionomer contents and carbon supports. Furthermore, the conditioning and voltage recovery impact on Pt/ionomer interface was studied and the differences of double layer capacities (C_{dl}), electrochemical surface areas (ECSAs), effective ionic conductivities and SO_3^- group coverages were measured. Given this new understanding of catalyst-ionomer interface the ultimate goal is to utilize this knowledge to reduce Pt loading within cathode catalyst layer.

6.2 Results

6.2.1 Conditioning and voltage recovery impact

Figure 6.1a plots the $-\omega^{-1} \times Z_{img}^{-1}$ as a function of ω^{-2} for the cell 2 before and after cell conditioning and voltage recovery.
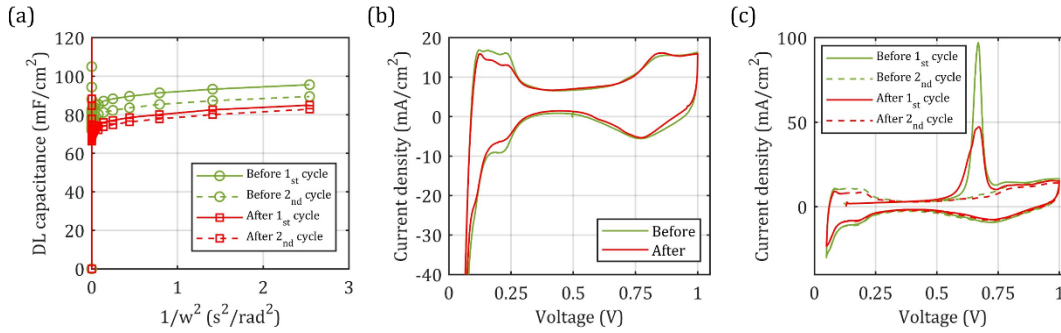
Figure 6.1 a) double layer capacitance b) CV and c) CO stripping comparisons for MEA before and after cell conditioning and voltage recovery process.

Figure 6.3a shows the C_{dl} before and after cell conditioning and recovery by extrapolating to $\omega^{-2} = 0$ from **Figure 6.1a**. C_{dl} decreased from 92.6 mF/cm² to 83.9 mF/cm² after conditioning and voltage recovery. According to Iden and Ohma's work [59], double layer capacity is measured for four interfaces within the catalyst layer, which are Pt/ionomer, Pt/water, carbon/ionomer, and carbon/water. C_{dl} total is the summation of these four interfacial capacities. After the cell conditioning and voltage recovery, the cell C_{dl} decreased likely because Pt particles agglomerated, which led to lower C_{dl} due to Pt particles surface area decrease because of Pt dissolution and precipitation [49]. **Figure 6.1b** and **Figure 6.1c** show the CV and CO stripping comparisons with 100 mV/s scan rate between before and after the cell conditioning and voltage recovery. A greater H_{upd} region was observed before the cell conditioning and

voltage recovery (**Figure 6.1b**). Similarly, the CO stripping peak was larger for the cell before it underwent conditioning and voltage recovery (**Figure 6.1c**). **Figure 6.3b** shows the averaged ECSA from the CV and CO stripping measurements. ECSA decreased from 45.7 m^2/g to 35.4 m^2/g after the cell conditioning and voltage recovery mainly due to increase in Pt particle size during this process. Kabir et al. have shown that voltage recovery results in removal of contaminants from the surface of Pt but at the same time increases their size due to Pt particles dissolution and precipitation [49]. Based on the H_2/N_2 EIS fitting model[109], the calculated effective ionic conductivity did not increase and remained at 0.0165 S/cm after the cell conditioning and voltage recovery probably because bulk ionomer remained unchanged during the activation process. (**Figure 6.3c**).

Figure 6.2a-d shows the CO displacement results for cell 2 before and after the cell conditioning and voltage recovery at 0.1 V, 0.2 V, 0.3 V and 0.4 V, respectively. CO stripping results at these corresponding voltages were shown in **Figure 6.2e-h**. Based on the Eqn. (21), SO_3^- group coverages were calculated and shown in **Figure 6.3d**. The species coverages were independent to the process of cell conditioning and voltage recovery. Because the ECSA decreased, similar SO_3^- group coverage before and after cell conditioning and voltage recovery indicates that some of the SO_3^- groups likely desorbed from the surface during conditioning. From **Figure 6.2** it is also seen that the CO-displacement charge decreased after cell conditioning and voltage recovery. At 0.4 V, SO_3^- group coverage was around 21 % for both cases. Overall, the cell conditioning and voltage recovery resulted in the ECSA and C_{dl} loss likely due to Pt particles size increase. The loss of the ECSA also resulted in loss of the SO_3^- group adsorption, so on net the SO_3^- group coverage remained the same before and after conditioning and voltage recovery.
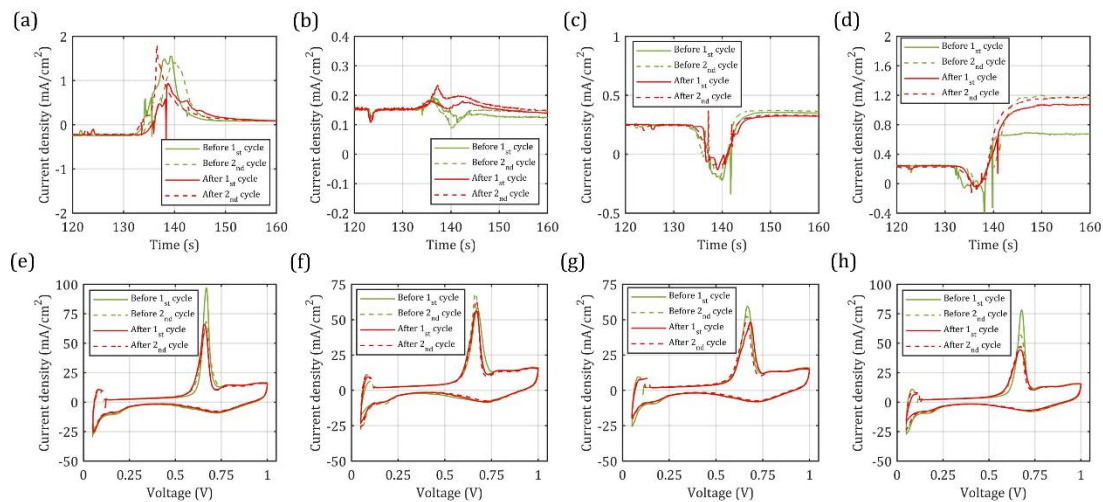
Figure 6.2 Comparisons of CO displacements at a) 0.1 V, b) 0.2 V, c) 0.3 V, d) 0.4 V and CO strippings at e) 0.1 V, f) 0.2 V, g) 0.3 V and h) 0.4 V for cell 2 before and after cell conditioning and voltage recovery at 60℃, 100 % RH and without additional back pressure. The 1st and 2nd here refers to two trials of CO displacement and stripping for reproducibility.
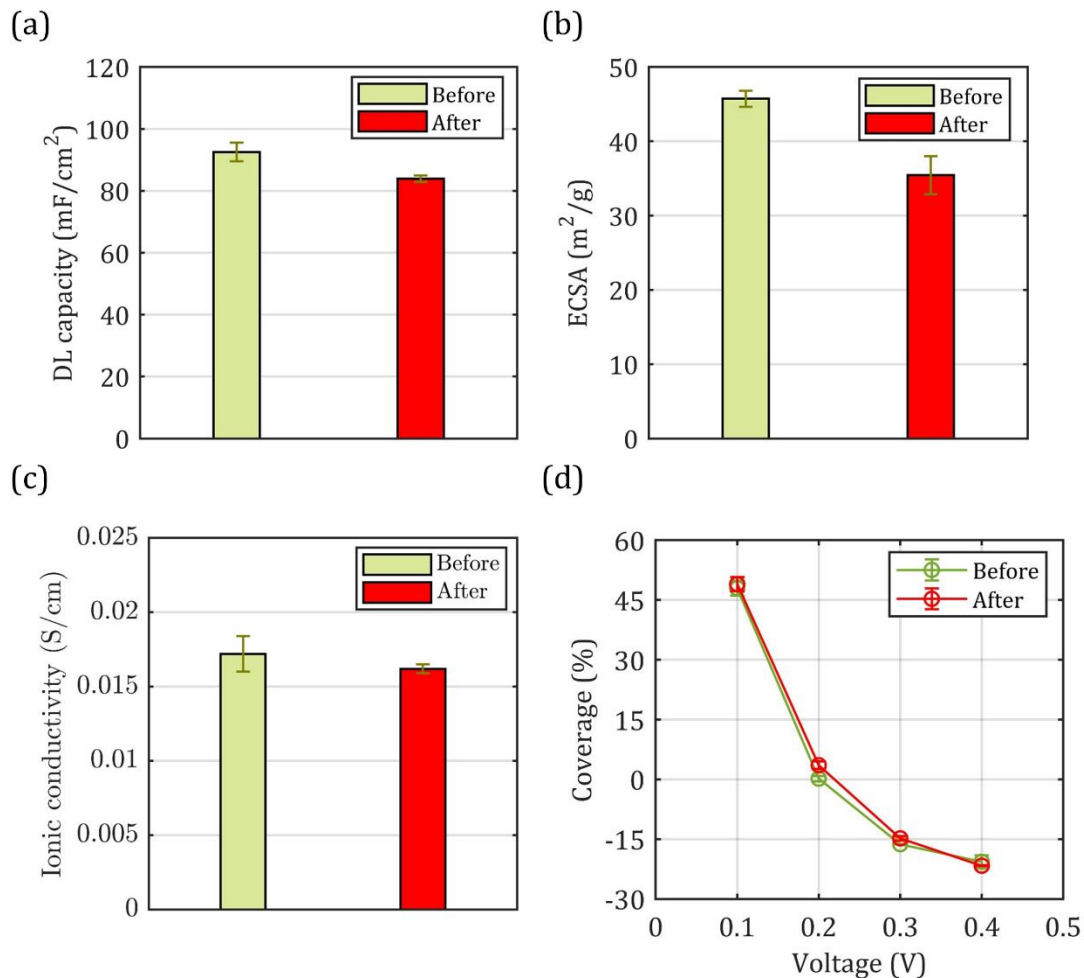
Figure 6.3 Comparisons of a) double layer capacities, b) ECSAs, c) catalyst layer ionic conductivities and d) H+ and SO$_3^-$ group coverages for cell 2 before and after cell conditioning and voltage recovery at 60 °C and 100 % RH with differential gas flows.

6.2.2 Pt loading effect

In this study cell 2 and cell 3 results were compared, as these cells have similar composition but different loadings of 0.19 mg/cm^2 for cell 2 and 0.35 mg/cm^2 for cell 3. **Figure 6.6a** shows the calculated C$_{dl}$ based on the plot of $-\omega^{-1} \times Z_{img}^{-1}$ (**Figure 6.4a**) for cell 2 and cell 3. C$_{dl}$ increased from 83.9 mF/cm^2 to 147 mF/cm^2 as Pt loading increased from 0.19 mg/ cm^2 to 0.35 mg/ cm^2 because the higher Pt loading in cell 3 resulted most likely in larger contact between solid/ionic

phase leading to a greater C_{dl}. **Figure 6.4b** shows CVs for cell 2 and cell 3, and cell 3 showed a greater H_{upd} region compared to cell 2 because of higher Pt loading. Apart from that, for the CO stripping, **Figure 6.4c** shows that cell 3 had a significantly higher CO stripping peak than cell 2. The resulting ECSAs were calculated according to integrations of H_{upd} regions and CO stripping peaks and were shown in **Figure 6.6b**. Cell 2 had ECSA of 35.4 m^2/g, compared to cell 3's 39.4 m^2/g. Higher Pt loadings might have had impact on ink rheology and might have resulted in lower carbon agglomeration resulting in better local Pt dispersion and higher ECSA. Effective ionic conductivities were calculated and shown in **Figure 6.6c**. Cell 2 had higher effective ionic conductivity of 1.62×10^{-2} S/cm compared to 1.29×10^{-2} S/cm for cell 3 because of possibly less carbon agglomerations for cell 3 during manufacturing, which led to a worse continuity and higher tortuosity of ionomer.
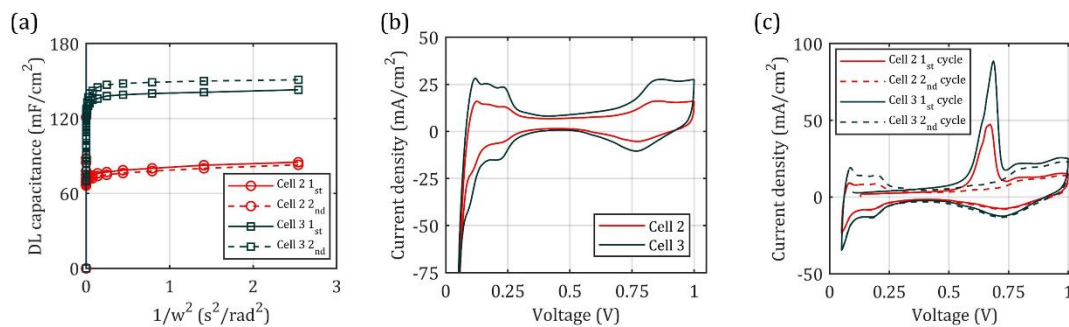
Figure 6.4 a) double layer capacitance b) CV and c) CO stripping comparisons for cell 2 and cell 3.

Figure 6.5a-d show the CO displacement results for cell 2 and cell 3 at 0.1 V, 0.2 V, 0.3 V and 0.4 V, respectively. CO stripping results at corresponding voltages were shown in **Figure 6.5e-h**. Ion species coverages at these voltages were calculated and shown in **Figure 6.6d**. At 0.1 V, H^+ coverage instead of SO_3^- group coverage was represented in the **Figure 6.6** since voltage was

lower than the PZC. Cell 2 and cell 3 showed identical H^+ coverages of 48.9 %. Both cell 2 and cell 3 showed the Pt PZC to lie somewhere between 0.2 – 0.25 V. As applied potential increased from PZC to 0.3 V, SO_3^- group coverage for cell 2 increased to 14.8 % compared to 14.2 % for cell 3. At 0.4 V, SO_3^- group coverage for cell 2 showed a value of 21.7 %, compared to cell 3's 17.8 %. Lower ionomer coverage for cell 3 may be due to higher Pt surface area exposed to ionomer. However, the difference in SO_3^- group coverage observed here for cell 2 and cell 3 is quite small and strong conclusion cannot be drawn.
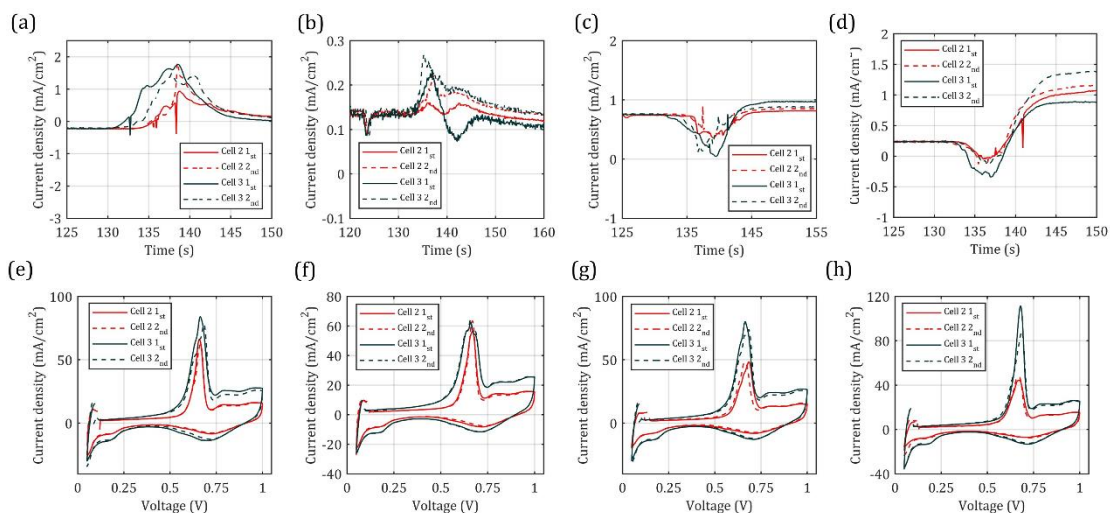
Figure 6.5 Comparisons of CO displacements at a) 0.1 V, b) 0.2 V, c) 0.3 V, d) 0.4 V and CO strippings at e) 0.1 V, f) 0.2 V, g) 0.3 V and h) 0.4 V for cell 2 and cell 3 at 60°C, 100 % RH and without additional back pressure.
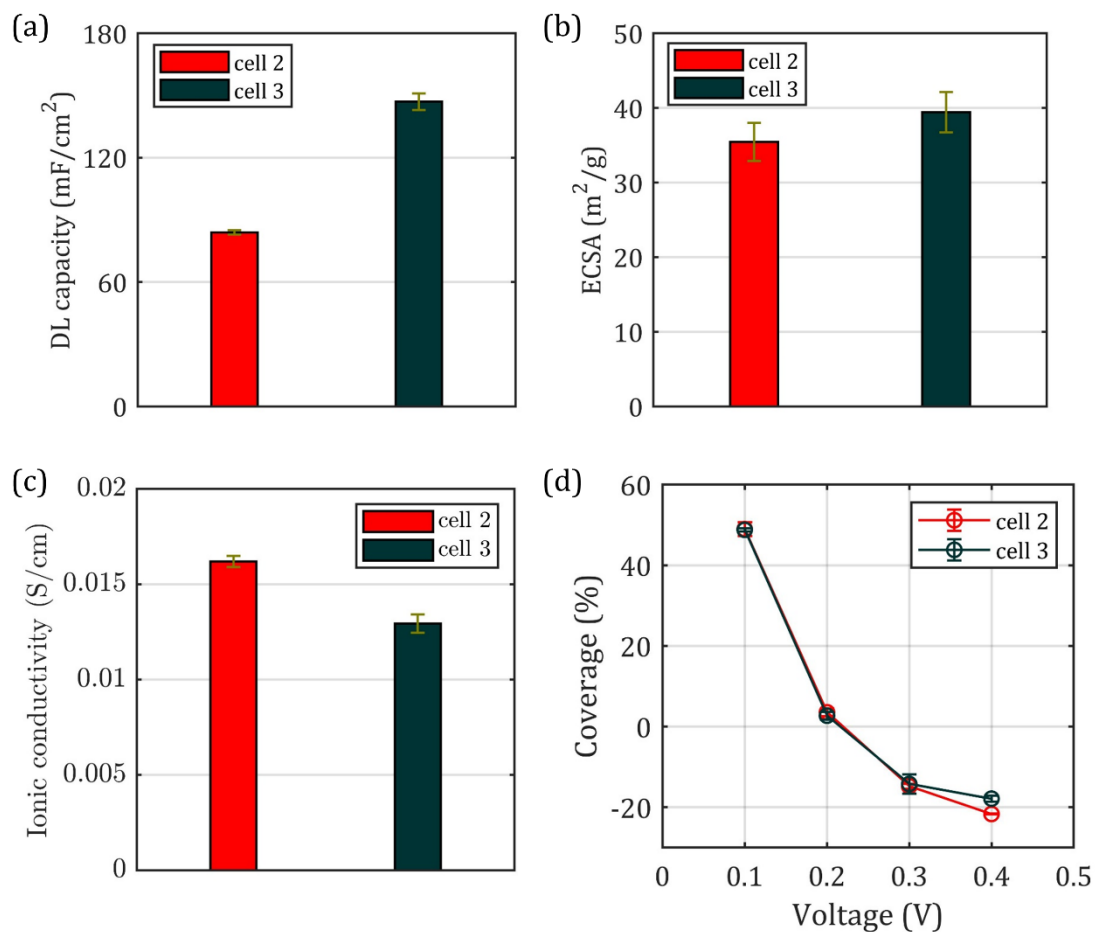
Figure 6.6 Comparison of cell 2 (0.19 mg/ cm^2) and cell 3 (0.35 mg/ cm^2) electrochemical data. a) Double layer capacities, b) ECSAs, c) catalyst layer ionic conductivities and d) H+ and SO$_3^-$ group coverages for cell 2 and cell 3 at 60 °C and 100 % RH with differential gas flows.

6.2.3 Ionomer content effect

Cell 2 with I/C of 0.9 was compared to cell 4 having the I/C of 0.3, the remaining properties of these cells were very similar. **Figure 6.7a** plots $-\omega^{-1} \times Z_{img}^{-1}$ as a function of ω^{-2} for cell 2 and

132

cell 4. The resulting C_{dl} were calculated and shown in **Figure 6.9a**. C_{dl} for cell 2 was 83.9 mF/cm² and it was compared to 82.1 mF/cm² for cell 4. C_{dl} was fairly independent to the I/C ratio indicating that cell 2 and cell 4 had similar amount of solid/ionic phase interfaces at fully humidified condition because C_{dl} is the summation of all four interfacial capacities and water also made contributions to the C_{dl}. For CVs, **Figure 6.7b** shows similar H_{upd} regions for both cell 2 and cell 4 and from the CO stripping results shown in **Figure 6.7c**, similar CO stripping peak integration areas were observed. ECSAs for both cells were similar because Pt surfaces were fully hydrated and accessible for H^+: cell 2 had 35.4 m²/g and cell 4 had 34.1 m²/g (**Figure 6.9b**). Effective ionic conductivities were derived and shown in **Figure 6.9c**. Cell 2 had 1.62×10^{-2} S/cm effective ionic conductivity, which was greater than cell 3's 1.32×10^{-2} S/cm because higher ionomer content improved bulk proton transport by forming thicker ionomer layers.
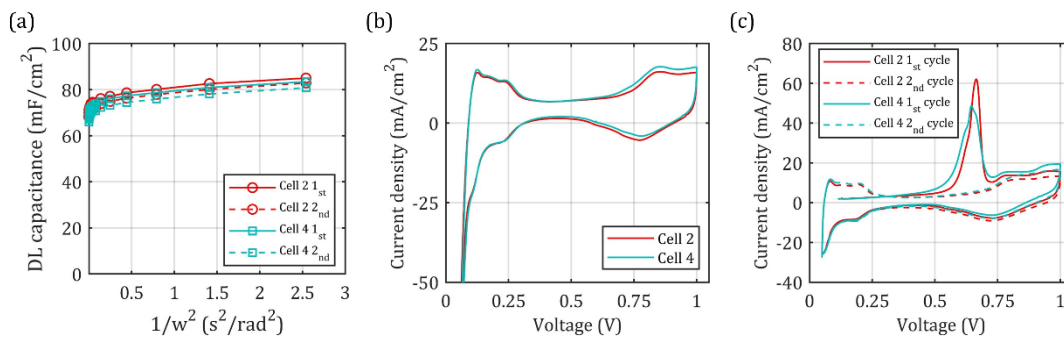
Figure 6.7 a) double layer capacitance b) CV and c) CO stripping comparisons for cell 2 and cell 4.

Figure 6.8a-d show the CO displacement results for cell 2 and cell 4 at 0.1 V, 0.2 V, 0.3 V and 0.4 V, respectively. CO stripping results at corresponding voltages are shown in **Figure 6.8e-h**. The resulting SO_3^- group and H^+ coverage comparison were shown in **Figure 6.9d**. At 0.1 V cell

2 had 48.9 % H^+ coverage compared to 43.6 % coverage for cell 3. As applied voltage increased from PZC to 0.3 V, similar increasing trends of SO_3^- group coverage were shown for both cell 2 and cell 4. SO_3^- group coverage for cell 2 increased to 14.8 % compare to 18.9 % for cell 4. At 0.4 V cell 2 showed SO_3^- group coverage of 21.7 % compared to 21.2 % for cell 4. PZCs for cell 2 and cell 4 were around 0.2-0.25 V.

Overall, increase in I/C ratio from 0.3 to 0.9 for catalyst layers having Vulcan XC-72 carbon black support resulted in similar ECSA and improved ionic conductivity. The SO_3^- group coverage was similar for both cells indicating that the saturated coverage for low I/C ratio cell and extra ionomer most likely did not form thin film on Pt but instead formed thicker ionomer film and ionically conductive network in larger pores. Even with I/C ratio of 0.3, SO_3^- group coverage was as high as 21.2 %. And for I/C ratio of 0.9, SO_3^- group coverage only increased 0.5 % after two times increase in the ionomer content.
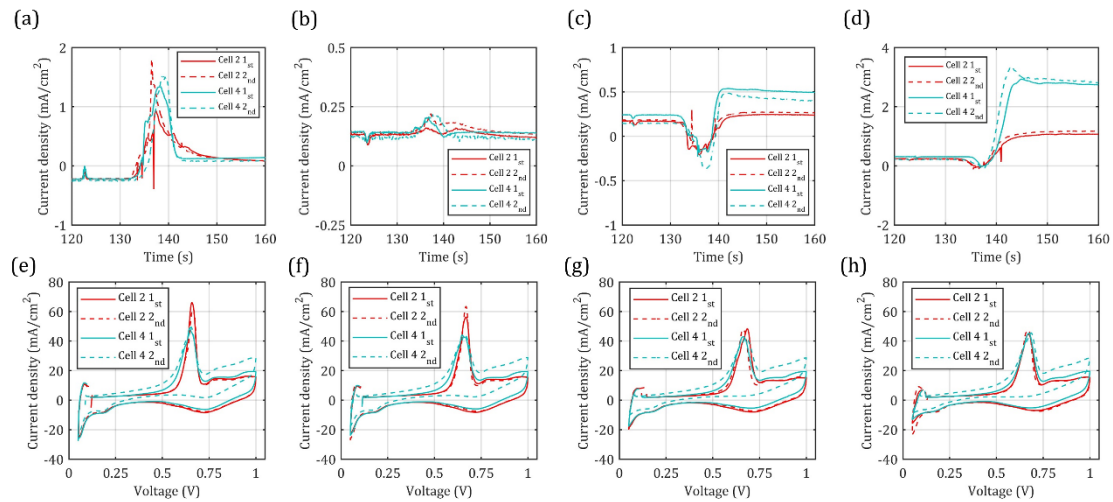
Figure 6.8 Comparisons of CO displacements at a) 0.1 V, b) 0.2 V, c) 0.3 V, d) 0.4 V and CO strippings at e) 0.1 V, f) 0.2 V, g) 0.3 V and h) 0.4 V for cell 2 and cell 4 at 60℃, 25 % RH and without additional back pressure.
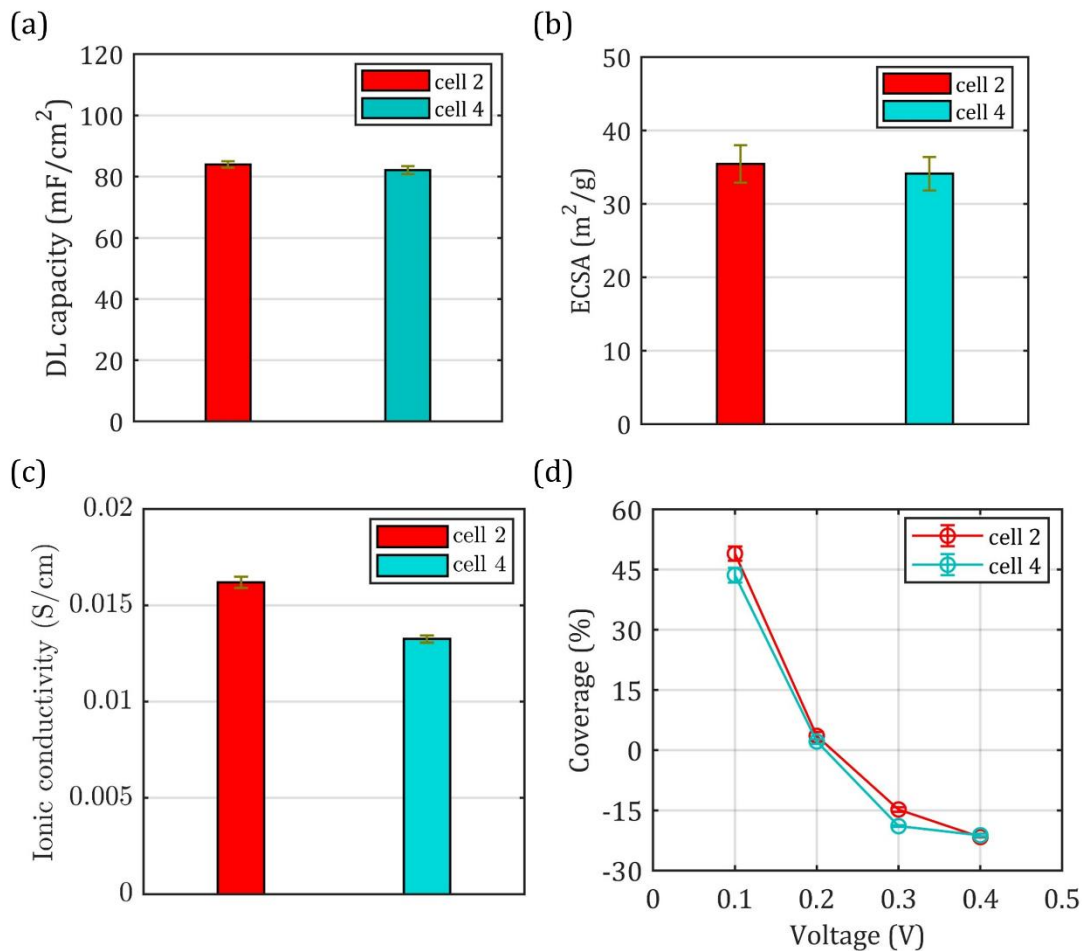
Figure 6.9 Comparisons of cells with varied I/C ratios, where cell 2 has I/C of 0.9 and cell 4 has I/C of 0.3. a) Double layer capacities, b) ECSAs, c) catalyst layer ionic conductivities and d) H+ and SO_3^- group coverages for cell 2 and cell 4 at 60 °C and 100 % RH with differential gas flows.

6.2.4 Carbon support effect

In this work, catalyst layer having HSA carbon was compared to Vulcan carbon. **Figure 6.12a** shows the calculated C_{dl} based on the plot of $-\omega^{-1} \times Z_{img}^{-1}$ (**Figure 6.10a**) for cell 1 and cell 2. C_{dl} for cell 1 was 145.4 mF/cm^2 and it was compared to 83.9 mF/cm^2 for cell 2 due to the greater surface area of carbon support resulted from the internal porous structure [93]. **Figure**

6.10b shows the CV measurements for cell 1 and cell 2. Cell 1 with HSA carbon displayed much

greater H_{upd} region and double layer capacitance region indicating higher ECSA and higher

contact between solid/ionic phase interfaces. Pt is better dispersed in HSA carbon and can be

deposited on the surface of carbon and within the meso-pores of the carbon support. The CO

stripping results shown in **Figure 6.10c** also show higher CO stripping peak for cell 1. The

comparison of ECSAs for cell 1 and cell 2 was shown in **Figure 6.12b**. Cell 1 had ECSA of 46.8

m^2/g compared to cell 2 ECSA of 35.4 m^2/g because of better Pt dispersion and less

agglomeration. **Figure 6.12c** shows the calculated catalyst layer ionic conductivities for cell 1

and cell 2. Cell 2 has higher effective ionic conductivity of 1.62×10^{-2} S/cm compared to

1.33×10^{-2} S/cm for cell 1 because the surface area of smaller meso-pores of carbon support

determined a better ionomer continuity and uniformity. [93]
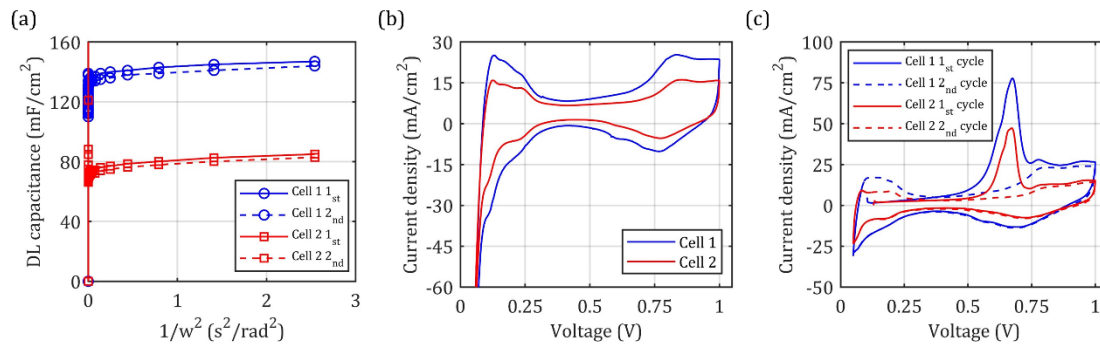
**Figure 6.10 a) double layer capacitance b) CV and c) CO stripping comparisons for cell 1
and cell 2.**

CO displacement results for cell 1 and cell 2 at 0.1 V, 0.2 V, 0.3 V and 0.4 V are shown in

Figure 6.11a-d, respectively. **Figure 6.11e-h** show the CO stripping results for both cells at

corresponding voltages, respectively. **Figure 6.12d** shows the comparison of SO_3^- group

coverages for cell 1 and cell 2. At 0.1 V, cell 1 showed 61.2 % H^+ coverage compared to cell 2's 43.9 %, which was consistent with the result that HSA carbon had better Pt dispersion due to the internal porous structure, and water provided proton accessibility for the Pt particles inside of the internal pores. As applied voltage increased from PZC to 0.3 V, SO_3^- group coverage of cell 1 increased to 13.1 %, whereas SO_3^- group coverage of cell 2 changed to 14.8 %. At 0.4 V, cell 2 showed higher SO_3^- group coverage of 21.7 % compared to cell 1's 16.3 %. Thus, the cell with HSA carbon support had lower SO_3^- group coverage compared to cell with Vulcan XC-72 carbon support because Pt within carbon meso-pores was not in contact with ionomer. Recent studies showed that meso-porous carbon support design is critical to ensure that Pt is buried not too far into the pores but at the same time is not contacted by SO_3^- groups. [76,93,110]
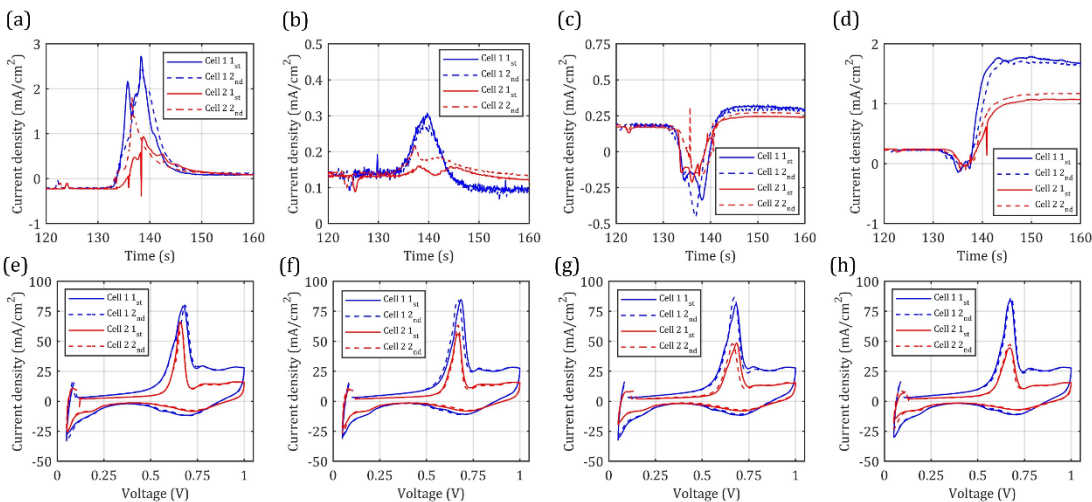
Figure 6.11 Comparisons of CO displacements at a) 0.1 V, b) 0.2 V, c) 0.3 V, d) 0.4 V and CO strippings at e) 0.1 V, f) 0.2 V, g) 0.3 V and h) 0.4 V for cell 1 and cell 2 at 60℃, 25 % RH and without additional back pressure.
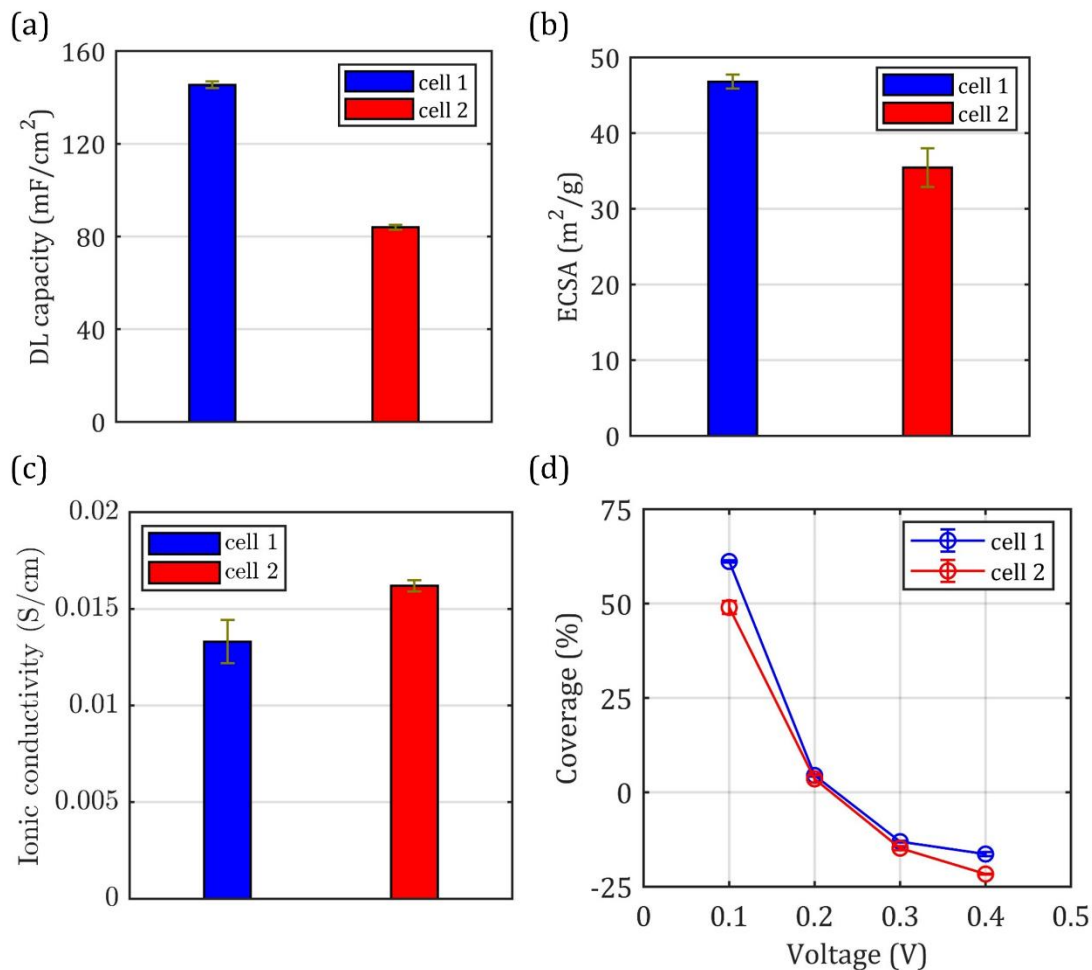
Figure 6.12 Comparison of cells with different carbon supports, where cell 1 has HSA carbon support and cell 2 has Vulcan XC-72 carbon black. a) Double layer capacities, b) ECSAs, c) catalyst layer ionic conductivities and d) H+ and SO_3^- group coverages for cell 1 and cell 2 at 60 °C and 100 % RH with differential gas flows.

6.3 Conclusion

In this work, electrochemical characterization was used to characterize four cells with various catalyst compositions varying Pt loading, ionomer content and carbon support. C_{dl} were derived using EIS data and effective ionic conductivities were obtained by inputting EIS data into the H_2/N_2 fitting transmission line model. SO_3^- group coverages were derived using CO displacement

and CO stripping techniques. The impact of conditioning and voltage recovery was studied using cell 2 and it was shown that after conditioning and voltage recovery the C_{dl} and ECSA decreased, which indicated that less solid/ionic phase interfaces were created due to Pt particle size growth. Furthermore, after conditioning and voltage recovery the cells showed similar SO_3^- group coverages and catalyst layer ionic conductivities. Similar SO_3^- group coverages but lower ECSA indicates that as Pt agglomerated after conditioning some of the SO_3^- groups desorbed from the surface. So on net the SO_3^- group coverage did not change.

Cells with 0.19 and 0.35 mg/cm^2 of Pt loadings were compared to understand the impact of catalyst loading on the ionomer adsorption. These cells had the same Pt contents on carbon weight percentage but different loadings, indicating that the catalyst layer with 0.35 mg/cm^2 will be thicker. The ECSA for higher Pt loading cell was higher likely because better local Pt particles dispersion created less carbon agglomeration. Potentially higher Pt agglomeration on the carbon support surfaces resulted in relatively lower SO_3^- group coverage for the cell with higher Pt loading. The effective ionic conductivity was lower for higher Pt loading cell maybe because the worse ionomer continuity due to carbon agglomerations.

For two cells having I/C ratios of 0.9 and 0.3 there was no difference in the ECSA and C_{dl} indicating that equal contact areas of different interfaces and similar proton accessibility at fully hydrated condition. Higher ionomer content resulted in higher effective ionic conductivity, as anticipated. Both cells showed very similar SO_3^- group coverage at 0.4 V. This is indicative that at I/C of 0.3 ionomer already formed a thin film around Pt and additional ionomer filled the larger pores and formed better ionic pathways network for proton transport.

Catalyst layers with HSA carbon and Vulcan carbon black supports were compared next. It was shown that the cell with HSA carbon had higher C_{dl} and ECSA compared to Vulcan carbon support because the internal porous structure of HSA carbon resulted in higher surface area and better Pt dispersion and less agglomeration. The averaged SO_3^- group coverage at 0.4 V was much lower for HSA carbon support compared to Vulcan XC-72, since ionomer did not have accessibility to the Pt particles, which were inside the HSA carbon support.

Chapter. 7 Study ionomer properties change during carbon corrosion AST.

7.1   Introduction

Polymer electrolyte fuel cell (PEFCs) using hydrogen as fuel show higher fuel efficiency and decrease pollutant emissions, which provides a promising way to combat climate change [5]. The major PEFCs applications are developed in the transportation sectors to replace the internal combustion engines (ICEs), where other applications focus on forklift power sources and electric vehicles range extenders [10,11]. However, due to the high voltage and some transient operations, fuel cell lifetimes are shortened due to the corrosions [111–113], which makes PEFCs vehicles difficult to be durability competitive to ICEs. U.S. Department of Energy (DOE) set the lifetime target of 8000 hours, 150000 equivalent driving miles with less than 10% performance lost for light-duty vehicles [41,114]. To meet the lifetime targets, electrochemical characterizations and morphology changes result from catalysts corrosion and carbon support corrosion must be investigated.

Carbon corrosion occurs at commercial PEFC catalyst layers, which consist of carbon-based support and Pt alloy catalysts especially for cathode catalyst layer due to: 1). Preferable oxidizing operation condition, 2). more water participation and Pt catalysis. The corrosion mechanism of carbon corrosion in catalyst layer is related to carbon oxidation by water [82,94]:

$$C + 2H_2O \rightarrow CO_2 + 4H^+ + 4e^-, \qquad E_0 = 0.207_{RHE} \tag{49}$$

Transient startup and shutdown (SUSD) operation usually shows 1.4-1.6 V voltage difference between cathode electrode and membrane, which is more favorable for carbon corrosion to occur [115,116]. Apart from that, cell voltage reversal results from starvation of H_2 leads to anode side carbon corrosion [113,117]. Based on these knowledge, two carbon corrosion accelerated stress test (AST) protocols are developed and recommended by U.S DOE, the U.S. DRIVE Fuel Cell Tech Team (FCTT), and the Japan Automobile Research Institute (JARI) [118]. The first protocol is related to cathode constant voltage hold at 1.2 V using H_2/N_2 [118], and the second protocol is H_2/N_2 cycling from 1-1.5 V with sweep rate of 500 mV s^{-1} [50]. However, due to formation of passive oxidation during AST, corrosion rate of the former shows 100-150 times slower than that of the latter [94]. In this work, 1-1.5 V cycling carbon corrosion AST was applied.

Selection of catalyst layer material and operation conditions are critical to extend the durability. For carbon support type, high surface area carbon (HSAC) shows the highest carbon oxidation rate due to the preferential oxidation of the more disordered domain of the carbon support [94,119]. The GrC support shows more resistant to electrochemical carbon corrosion with the lowest corrosion rate since it has the greatest graphitic carbon content, which are more robust than disordered amorphous carbon [94,119–122]. Another factor which impacts carbon corrosion rate is Pt content. It has been shown that the Pt catalyzes carbon corrosion in the

operation voltage range of 1-1.5 V, most likely via the formation of oxygen- containing surface groups (CO_{ad}) absorbed on the metal surface followed by their oxidation into CO_2 [60,123]:

$$C + H_2O \rightleftharpoons C - O_{ad} + 2H^+ + 2e^- \tag{50}$$

$$Pt + H_2O \rightleftharpoons Pt - OH_{ad} + H^+ + e^- \tag{51}$$

$$C - O_{ad} + Pt - OH_{ad} \rightleftharpoons Pt + CO_2 + H^+ + e^- \tag{52}$$
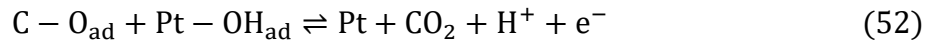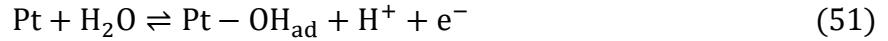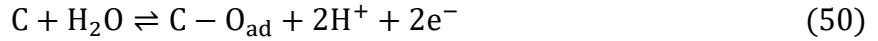
Pt/HSAC with most disordered amorphous carbon content usually shows better Pt dispersion because Pt nanoparticles preferentially deposit within the amorphous domain. However which also deteriorates carbon support corrosion due to Pt catalysis. Apart from material selection, operation condition also plays an important role on carbon corrosion in PEFC. Mittermeier et al. [124] showed carbon corrosion rate increased with relative humidity (RH). Overall, carbon corrosion in PEFC is still one of the key challenges and designation of catalyst layer and optimal operation condition provide much insights to mitigate this issue.

Carbon corrosion causes irreversible damages to the membrane electrode assembly (MEA). Electrochemical surface area (ECSA) reduced due to coalescence and sintering of Pt particles [94]. Collapse of catalyst layer porous structure was observed by previous studies [125,126]. Despite many studies focused on carbon support degradations, few works are related to comparison between different carbon support types using cycling AST protocol adopted by DOE and it is still unclear how their electrochemical performances change during AST. In this work,

lifetimes of HSAC and GrC supports and electrochemical characterizations were examined. Scanning electron microscopy (SEM) was performed to measure catalyst layer thickness reduction after AST. Scanning transmission electron microscopy (STEM) and transmission electron microscope (TEM) were applied to quantify Pt particle size growths. X-ray photoelectron spectroscopy (XPS) was used to study surface chemistry. Lastly, micro-X-ray fluorescence (XRF) was used to detect Pt content lost after carbon corrosion AST.

7.2   Results

7.2.1   Polarization curves, voltage performance and HFRs

Performance results from **Figure 7.1a** show the degradation of MEA using Pt/HSAC support over 1000 carbon corrosion AST cycles. After 100 cycles, Pt/HSAC showed slight loss in performance compared to the BOL, with a voltage loss of 13 mV at 1 A cm^{-2} (**Figure 7.1b**). From HFR results shown in **Figure 7.1a**, after 100 AST cycles, the HFR of the cell decreased from 66 ohms cm^2 to 62.5 ohms cm^2 due to the better contacts between GDL/catalyst layer and electrode hydration. After 500 cycles, a significant voltage loss of 391 mV at 0.6 A cm^{-2} was shown in **Figure 7.1a**. However, a similar HFR of the cell of 64.8 ohms cm^2 was measured after 500 AST cycles (**Figure 7.1a**), which indicates that the performance drop might be majorly due to the collapse of the catalyst layer porous structure leading to a mass transport problem. At EOL, the performance loss deteriorated to 443 mV at 0.2 A cm^{-2} (**Figure 7.1a**). However HFR increased to 103.1 ohms cm^2 (56.2 % increase compared to BOL) at EOL due to contacts loss between catalyst layer at GDL, which indicates that at EOL, the cell had both ohmic and mass transport issues leading to significant loss of performance.

For Pt/GrC, from the results shown in **Figure 7.1c**, cell performance did not change after 1000 AST cycles and voltage at 1 A cm^{-2} was maintained around 0.668 V (**Figure 7.1d**). After 2500 cycles, a 9 mV voltage loss at 1 A cm^{-2} was observed. HFR shown in **Figure 7.1c** after 2500 cycles decreased from 65.1 ohms cm^2 to 60.4 ohms cm^2 due to the better contacts at GDL/catalyst layer interfaces and further hydration of the electrode, which is similar to Pt/HSAC. After 5000 cycles, the cell degraded and a voltage loss of 51 mV at 1 A cm^{-2} was observed (**Figure 7.1c** and **Figure 7.1d**). The performance decreased significantly at the EOL shown in **Figure 7.1c**, which was after 10,000 AST cycles. Cell voltage decreased 289 mV at 0.2 A cm^{-2} at the EOL due to the loss of ECSA and porous structure collapse of catalyst layer. However, in **Figure 7.1c**, HFR maintained constant during the AST, which indicates the well contacts between catalyst layers and GDLs.
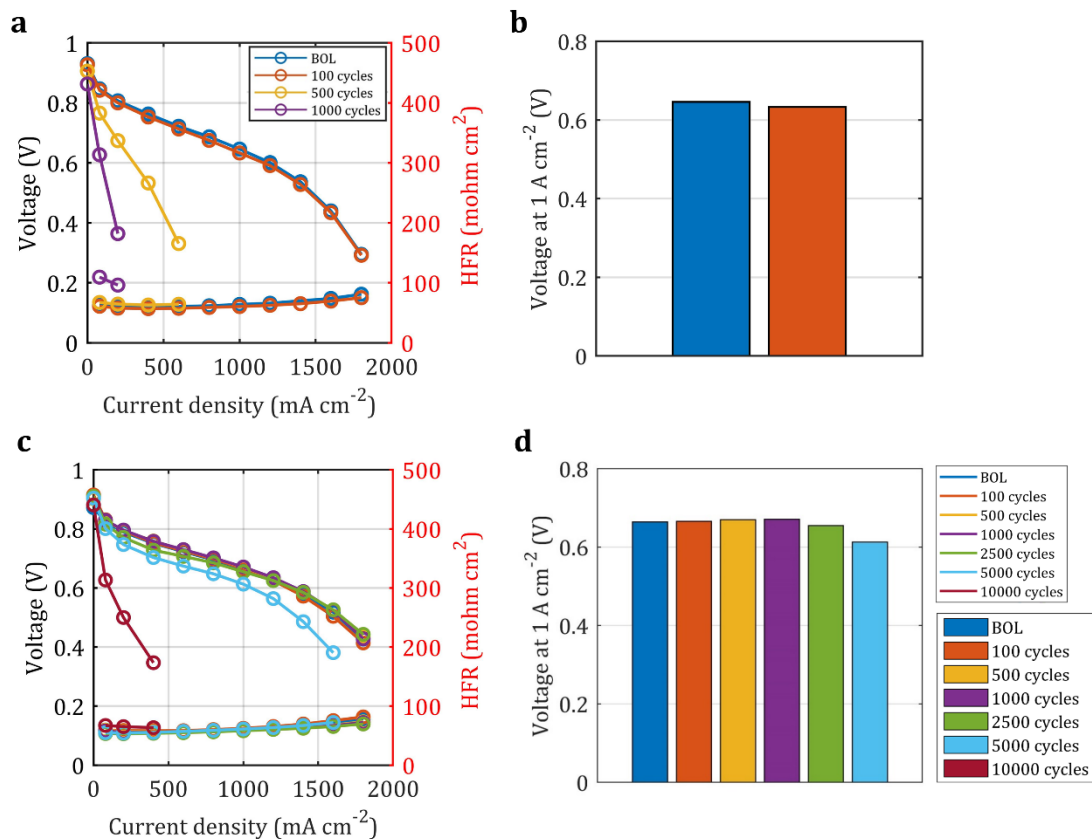
Figure 7.1 Performance and HFRs of MEAs using HSAC (a and b) and GrC (c and d) supports during carbon corrosion AST. For Pt/HSAC, (a) MEA performance at 80 °C, 100% RH, 150 kPa in H₂/Air with stoichiometric anode and cathode flows of 2 and 2 and HFR at BOL, after 100, 500, and 1000 AST cycles (EOL), (b) voltage at 1 A cm⁻². For Pt/GrC, (c) MEA performance at 80 °C, 100% RH, 150 kPa in H₂/Air with stoichiometric anode and cathode flows of 2 and 2 and HFR at BOL, after 100, 500, 1000, 2500, 5000, and 10000 AST cycles (EOL), (d) voltage at 1 A cm⁻².

7.2.2 Double layer capacities, CV measurements and ECSAs

Catalyst layer and interfacial properties were measured for both HSAC and GrC support during AST. For Pt/HSAC, C_{dl} was measured using the Eqn. (9) and shown in **Figure 7.2a**. According to Iden and Ohma's work [59], C_{dl} was determined as the summation of four interfaces within the catalyst layer, which are Pt/ionomer, Pt/water, carbon/ionomer, and carbon/water, which also

indicates the relative contacts between solid/ionic phase materials. At BOL, Pt/HSAC shows much higher C_{dl} of 108.3 mF cm^{-2} (**Figure 7.2a**) compared to 35.2 mF cm^{-2} of Pt/GrC (**Figure 7.2d**), because of the greater surface area of carbon black support due to the internal porous structure (amorphous domain) [93]. C_{dl} for Pt/HSAC increased to 132 mF cm^{-2} after 100 AST cycles and further increased to 154.8 mF cm^{-2} after 500 cycles because carbon corrosion formed rougher support surfaces, which created more contacts with ionomer and water. At EOL, C_{dl} decreased to 137 mF cm^{-2} likely because of the lack of contacts between water and catalyst material within the porous structure due to the structure collapse. A total capacity increase of 28.7 mF cm^{-2} (26.5 %) at EOL was shown in **Figure 7.2a**. For Pt/GrC, C_{dl} shown in **Figure 7.2d** remained at around 35.2 mF cm^{-2} after 100 cycles, followed by a gradual increase with the AST cycling number. Eventually a significant increase of 30.2 mF cm^{-2} (85.8 %) at EOL was observed, which reached 65.4 mF cm^{-2}. The increase of C_{dl} for Pt/GrC was much greater than that of Pt/HSAC and it might be because the disordered oxidation of ordered graphitic carbon created much more disorganized surface (more porous surface) leading to a significant C_{dl} increase compared to Pt/HSAC.

Figure 7.2b and **Figure 7.2e** show the CV measurements for Pt/HSAC and Pt/GrC during AST respectively. H_{upd} peaks decreased as a function of cycle number, as expected for both HSAC and GrC supports. The decrease of H_{upd} peak for Pt/GrC was much smaller compared to Pt/HSAC because Pt/HSAC had higher carbon oxidation rate at amorphous domains where Pt particles were well dispersed and catalyzed carbon corrosion reaction. ECSA results calculated from CV measurements for both carbon support types are shown in **Figure 7.2c** and **Figure 7.2f**. Reductions of ECSAs show consistency with H_{upd} results. Pt/HSAC, at the BOL showed higher

ECSA value of 41.9 m^2 g^{-1} (**Figure 7.2c**) compared to 30.6 m^2 g^{-1} for Pt/GrC (**Figure 7.2f**) because of less Pt agglomeration and a good dispersion within the internal porous structure. ECSA for Pt/HSAC (**Figure 7.2c**) decreased most rapidly at first 100 AST cycles from 41.9 m^2 g^{-1} to 35.0 m^2 g^{-1} (16.5 %), then slightly slowly decreased to 24.4 m^2 g^{-1} (41.8 %) after 500 AST cycles. Eventually ECSA decreased to 16.9 m^2 g^{-1} and a total ECSA loss of 25 m^2 g^{-1} (59.7 %) was observed for Pt/HSAC at the EOL. For Pt/GrC (**Figure 7.2f**), reduction of the ECSA was relatively moderate. ECSA maintained constant after the first 100 AST cycles and was reduced by 10 % after the first 1000 cycles, then followed by a decrease of 23 % after 5000 AST cycles. Eventually, ECSA for Pt/GrC decreased by 44 % and reached 17.1 m^2 g^{-1} after 10,000 cycles (EOL). Possible reasons for ECSA reduction might be: 1) Pt detachment occurred and Pt became inactive, 2) Pt was lost during the AST, 3) Pt particle size growth, and 4) Pt surfaces lost H$^+$ and/or oxygen accessibility due to collapse of catalyst layer porous structure. Reduction of the ECSA was another reason for performance drop shown in **Figure 7.1a** and **Figure 7.1c**.
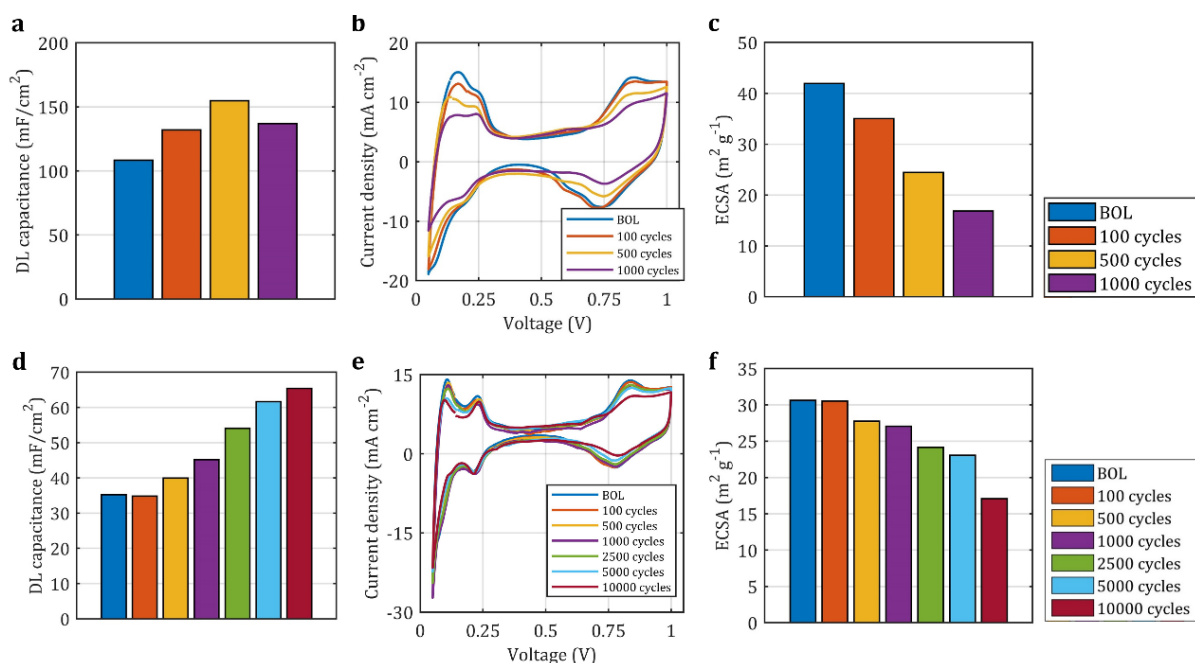
Figure 7.2 Double layer capacitance, CV measurements and ECSAs of MEAs using HSAC (Figure 7.2(a)-(c)) and GrC (Figure 7.2(d)-(f)) supports during carbon corrosion AST. For Pt/HSAC, (a) double layer capacitance, (b) cyclic voltammetry measurements, (c) ECSA at BOL, after 100, 500, and 1000 cycles (EOL). For Pt/GrC, (d) double layer capacitance, (e) cyclic voltammetry measurements. (f) ECSA at BOL, after 100, 500, 1000, 2500, 5000, and 10000 cycles (EOL).

7.2.3 Pt loading maps

Local averaged Pt loading distributions at the BOL and EOL for Pt/HSAC and Pt/GrC are shown in **Figure 7.3c** and **Figure 7.3f** respectively according to micro XRF maps for BOL (**Figure 7.3a** and **Figure 7.3d**) and EOL (**Figure 7.3b** and **Figure 7.3e**). Local averaged Pt loadings for Pt/HSAC shown in **Figure 7.3c** reached 0.635 mg cm^{-2} at the BOL and increased to 0.702 mg cm^{-2} at the EOL. For Pt/GrC, local averaged Pt loading shown in **Figure 7.3f** increased from 0.746 mg cm^{-2} at BOL to 0.829 mg cm^{-2} at EOL. For both carbon supports, Pt loadings did not decrease at their EOLs, which rules out any Pt lost during the AST. The reason for

150

increase in Pt loadings is because only 2 mm x 2 mm area was mapped and the BOL and EOL samples were from the same batch but it was not identical MEA. The combined results of the ECSA losses shown in **Figure 7.3c** and **Figure 7.3f** indicate that Pt detachment and particle size growth are the main reasons for the decrease of the ECSA.
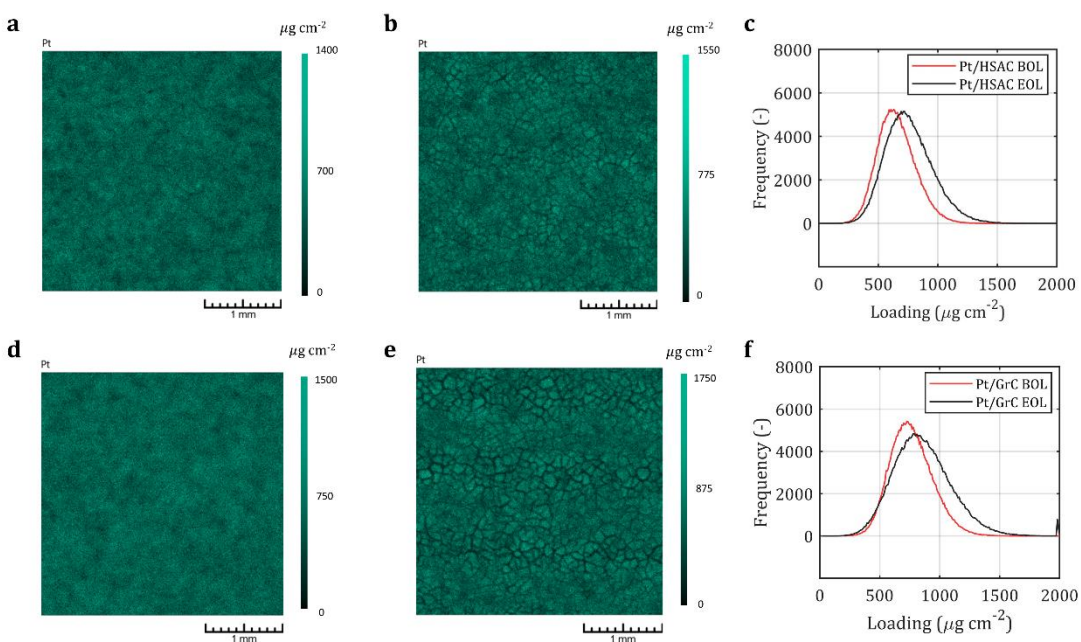
Figure 7.3 Micro X-ray fluorescence (XRF) maps for Pt/HSAC at (a) BOL and (b) EOL. (c) Loading-frequency distribution for Pt/HSAC at BOL and EOL. Micro X-ray fluorescence (micro XRF) maps for Pt/GrC at (d) BOL and (e) EOL. (f) Loading-frequency distribution for Pt/GrC at BOL and EOL.

7.2.4 Pt particle sizes

STEM and TEM were conducted to measure Pt particle sizes for Pt/HSAC and Pt/GrC, which are shown in **Figure 7.4**. For HSAC shown in **Figure 7.4a** and **Figure 7.4b**, Pt particle size increased from 2.25 nm at BOL to 3.96 nm (76 %) after 1000 AST cycles at EOL. However, a significantly larger nanoparticle size growth of 210 % was observed for GrC from 2.67 nm at BOL (**Figure 7.4c**) to 8.27 nm after 10000 cycles at EOL (**Figure 7.4d**). The growth of Pt

151

particle size was due to Pt particles coalescence and sintering for both carbon support types. Apart from that, greater ECSA loss but a lower particle size growth for Pt/HSAC strongly suggested that the greater Pt detachment occurred during the AST during carbon corrosion. More well dispersed Pt particles in HSAC support catalyzed carbon oxidation reaction in the disordered and amorphous domains of the HSAC support, perhaps resulting in Pt detachment and loss of electric contact with carbon. Once the detachment occurred, those Pt particles were recognized as inactive particles and their growth no longer occurred. For GrC support, due to lack of the disordered and amorphous carbon content and presence of mostly graphitic domains, Pt particles located on the surface of carbon support had higher mobility [94], leading to greater particle coalescence and less detachment during the AST, which was likely the major reason for the ECSA reduction. Macauley et al. [94] also found that Pt/GrC showed a significant Pt particle size growth compared to Pt/HSAC.
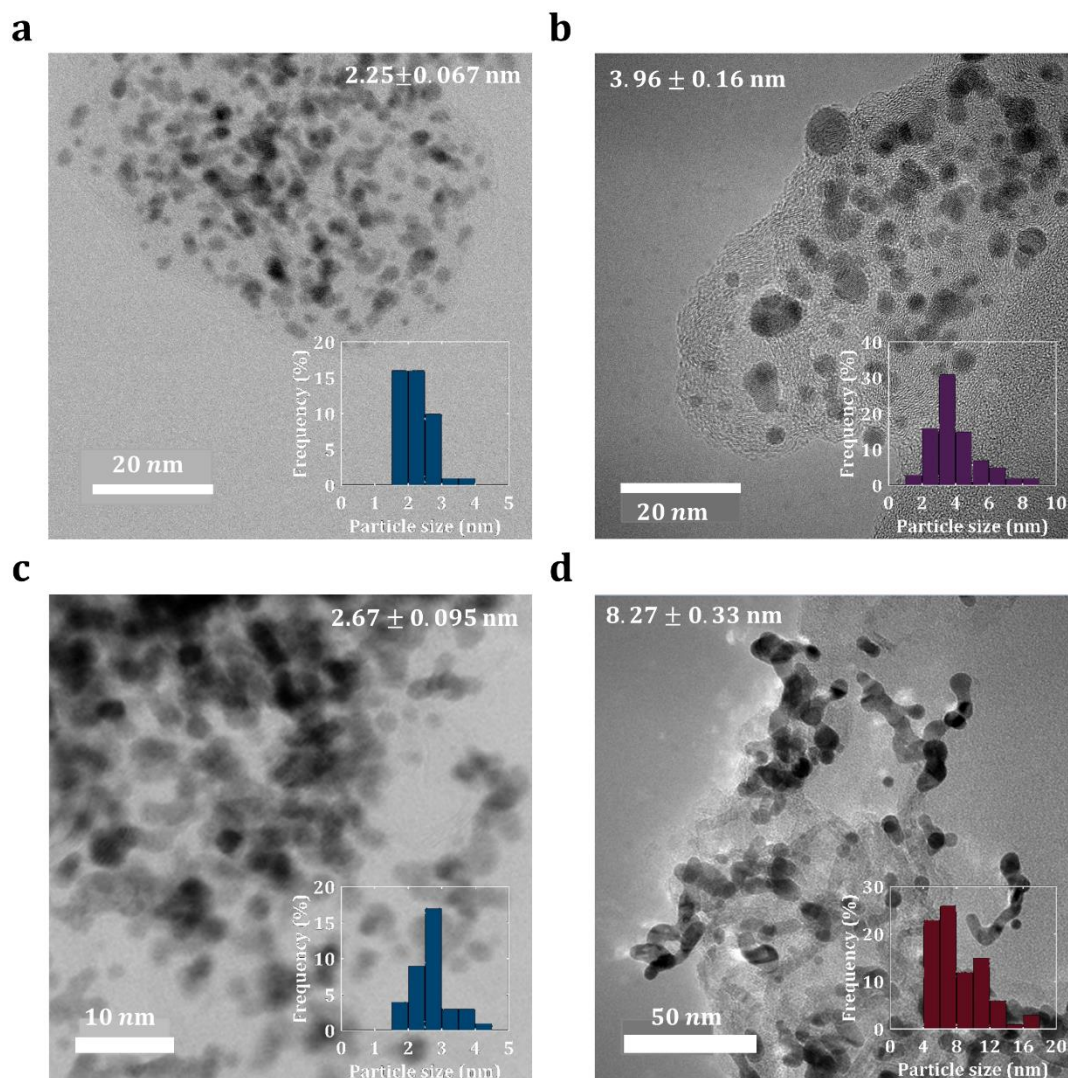
Figure 7.4 Scanning transmission electron microscopy (STEM) and transmission electron microscopy (TEM) measurements with Pt particle size distributions for Pt/HSAC (a and b) and Pt/GrC (c and d). (a) Scanning transmission electron micrographs of mean particles size at BOL for Pt/HSAC. (b) Transmission electron micrographs of mean particles size at EOL for Pt/HSAC. (c) Scanning transmission electron micrographs of mean particles size at BOL for Pt/GrC. (d) Transmission electron micrographs of mean particles size at EOL for Pt/GrC.

7.2.5 Catalyst layer thicknesses

Averaged catalyst layer thicknesses at BOL and EOL for Pt/HSAC and Pt/GrC are shown in

Figure 7.5c and **Figure 7.5f**, respectively according to the cross-section SEM measurement

results for BOL (**Figure 7.5a** and **Figure 7.5d**) and EOL (**Figure 7.5b** and **Figure 7.5e**).

Catalyst layer thickness of Pt/HSAC decreased from 8 μm at BOL to 3.43 μm after 1000 AST

cycles at EOL (57 %). For Pt/GrC, thickness of catalyst layer decreased from 13 μm at BOL to

6.45 μm after 10000 AST cycles at EOL (50.4 %). Thickness reduction for Pt/HSAC due to the

carbon support oxidation also explained the increase of HFR (**Figure 7.1a**). At EOL, HFR for

Pt/HSAC increased 56.2 % due to the reduction of catalyst layer thickness, which resulted in

insufficient contacts between GDL and catalyst layer. However, for Pt/GrC, even though catalyst

layer thickness decreased to 6.45 μm at EOL, it still provided sufficient contacts at the catalyst

layer/GDL interface, which resulted in a maintained HFR (**Figure 7.1c**).
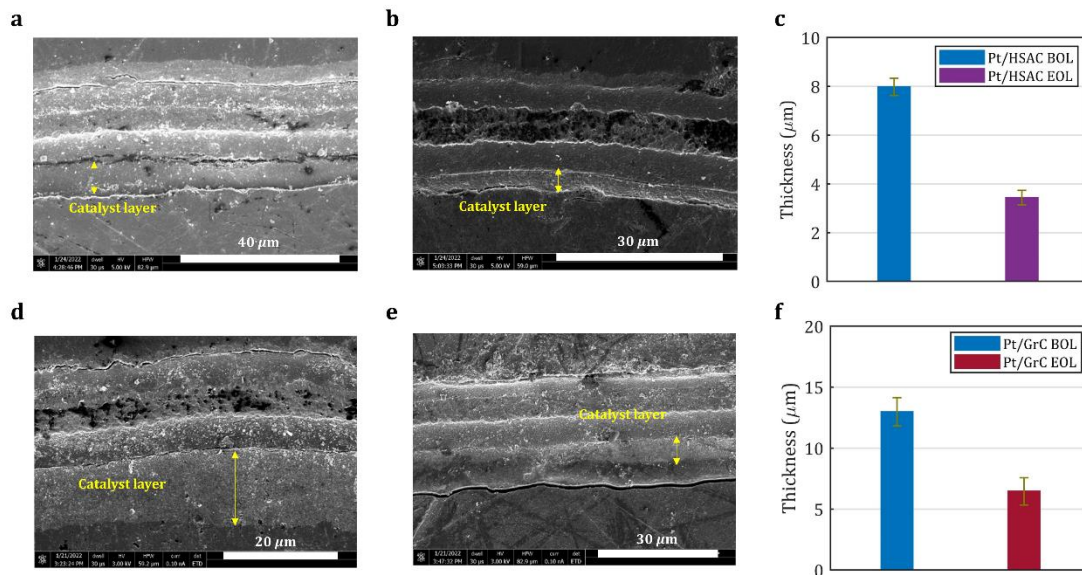
Figure 7.5 Cross-sectional scanning electron microscope (SEM) and averaged catalyst layer thickness reductions for Pt/HSAC (a-c) and Pt/GrC (d-f) during AST. Catalyst layer thicknesses for Pt/HSAC using SEM at (a) BOL and (b) EOL. (c) Thickness reduction at

EOL for Pt/HSAC. Catalyst layer thicknesses for Pt/GrC using SEM at (d) BOL and (e) EOL. (f) Thickness reduction at EOL for Pt/GrC.

7.2.6   Surface chemistry

In this work, XPS was performed to study the surface chemistry and high-resolution XPS spectras were measured at BOL and EOL for Pt/HSAC and Pt/GrC, respectively. **Figure 7.6** shows the relative percentages of different surface carbonaceous moieties and Table 12 shows the summarized quantitative results. For Pt/HSAC (**Figure 7.6a** and **Figure 7.6b**), the relative content of the sp^3 hybridized moieties decreased from 4.55 % at BOL to 1.59 % at EOL, which can be interpreted by the oxidation of disordered and amorphous carbon. The increase of relative concentration of COOH group from 7.25 % at BOL to 14.17 % at EOL also indicates the carbon oxidation during AST. The decrease of C-F bond relative percentage from 20.31 % at BOL to 11 % at EOL can be explained as the degradation of ionomer during AST. Compared to Pt/HSAC, Pt/GrC (**Figure 7.6c** for BOL and **Figure 7.6d** for EOL) had more sp^2 moieties with relative concentration of 56.3 % at BOL since it has the most ordered and graphitic carbon. At EOL, sp^2 moieties relative concentration decreased to 46.1 % because of the oxidation of carbon support. Due to the relative percentage decrease of sp^2 moieties, relative concentrations of some of other moieties increased for example, C-F2 group. C-F group relative concentration remained the same between the BOL and EOL indicating the ionomer degradation is minor during carbon corrosion AST using GrC support.
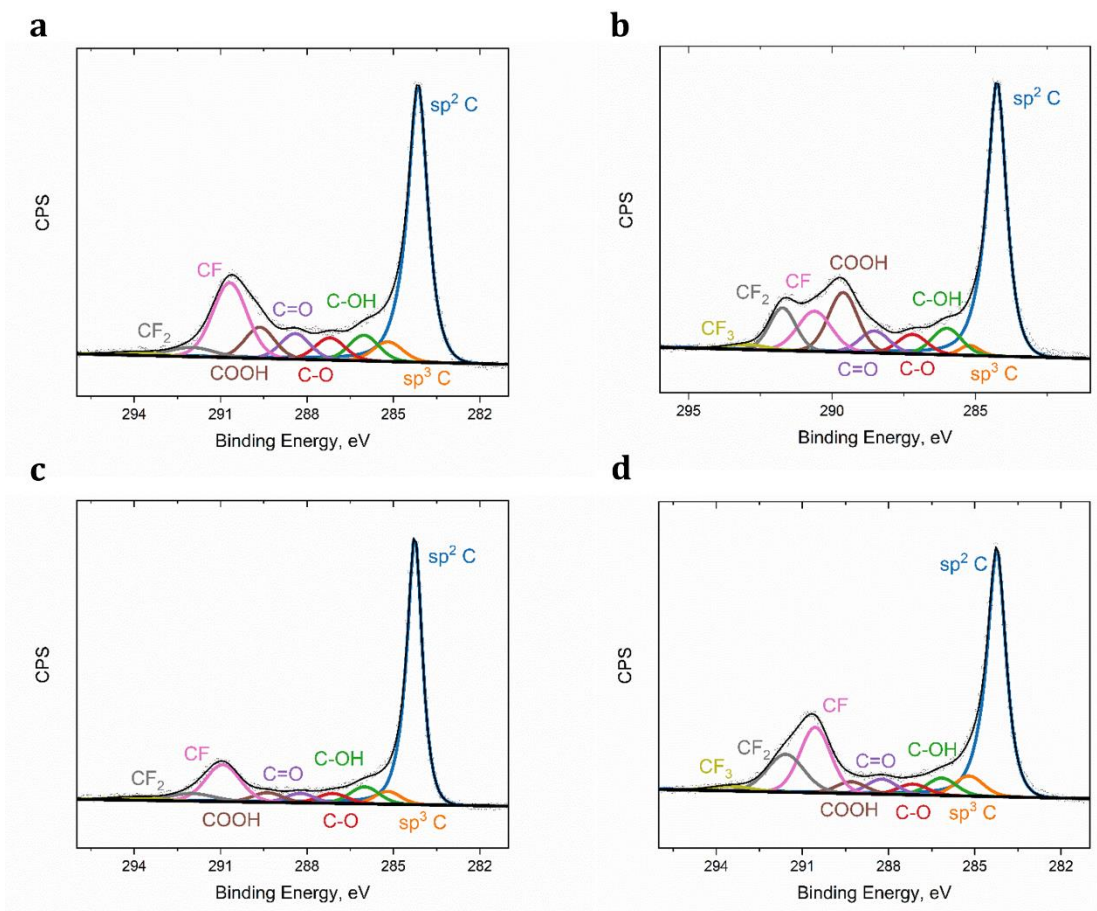
Figure 7.6 X-ray photoelectron spectroscopy of cathode catalyst layers for Pt/HSAC (a and b) and Pt/GrC (c and d) at BOLs and their EOLs: (a) Pt/HSAC at BOL, (b) Pt/HSAC at EOL, (c) Pt/GrC at BOL, (d) Pt/GrC at EOL.

Table 12. Relative concentrations for surface species for Pt/HSAC and Pt/GrC at BOLs and their EOLs

(%)	Binding energy (eV)	HSAC BoL	HSAC 1000 cycles (EOL)	GrC BoL	GrC 10000 cycles (EOL)
sp^2 C	~284	46.56	46.30	56.26	46.14
sp^3 C	~285	4.55	1.59	4.25	5.35

C-OH	~286	5.97	6.32	6.44	4.75
C-O	~287	5.16	4.65	3.71	2.94
C=O	~288	5.94	5.23	3.4	4.11
COOH	~289	7.25	14.17	3.65	3.22
C-F	~291	20.31	11.00	16.28	18.78
C-F2	~292	3.22	9.10	4.32	12.89
C-F3	~293	1.03	1.65	1.68	1.32

7.2.7 Catalyst layer ionic conductivities and sulfonic acid group coverages

Catalyst ionic conductivities were measured and shown in **Figure 7.7Error! Reference source not found.** by using a H_2/N_2 EIS fitting model according to Qi et al. [109] for both Pt/HSAC and Pt/GrC at the BOL and EOL. In that work, cell active area, frequency, real part of impedance, imaginary part of impedance and catalyst layer thickness were input into the developed H_2/N_2 EIS impedance fitting model and effective ionic conductivity was derived. For Pt/HSAC, according to impedance Nyquist plot shown in Fig. S6a, catalyst layer ionic conductivity decreased from 1.38×10^{-2} S/cm at BOL to 8.47×10^{-3} S/cm (38.6 %) after 1000 AST cycles at EOL (**Figure 7.7a**). For Pt/GrC, ionic conductivity of catalyst layer according to impedance Nyquist plot shown in Fig. S7b was 3.48×10^{-2} S/cm at BOL, which was 2.5 times higher compared to Pt/HSAC, since the GrC support has better ionomer continuity and uniformity than HSAC support [93]. At EOL, catalyst ionic conductivity increased to 3.93×10^{-2} S/cm (**Figure 7.7b**). The reduction of ionic conductivity for Pt/HSAC was due to the collapse of catalyst layer porous structure leading to the increase of discontinuity of ionomer and water distributions within the catalyst layer. However for Pt/GrC, it is likely that Pt particles with higher mobility

formed greater size Pt particle on carbon support surface, which resulted in less tortuous H^+

pathways, and consequently the catalyst layer ionic conductivity increased.

SO_3^- group coverages at 0.4 V were calculated and shown in **Figure 7.7c** using CO displacement

(Fig. S2a for Pt/HSAC and Fig. S2c for Pt/GrC) and CO stripping (Fig. S2b for Pt/HSAC and

Fig. S2d for Pt/GrC) methods for both Pt/HSAC and Pt/GrC. For Pt/HSAC, SO_3^- group coverage

decreased from 12.1 % at BOL to 3.4 % after 10000 AST cycles at EOL. According to the

combined results of the ECSA loss, Pt detachment might be the principal reason for the 71.9 %

reduction of SO_3^- group coverage at EOL. Pt/GrC shows a higher SO_3^- group coverage of 17.5 %

at BOL compared to Pt/HSAC because Pt particles within HSAC support meso-pores were not in

contact with ionomer. Recent studies showed that Pt nanoparticles within meso-porous carbon

support are buried not too far into the pores but at the same time were not contacted by SO_3^-

groups [76,93,110]. After 5000 AST cycles, SO_3^- group coverage for Pt/GrC decreased 22.3 %

and reached 13.6 %, which was not as significant compared to Pt/HSAC and it also indicated

lower degree of ionomer detachment and reorientation during the AST. This is further confirmed

with XPS data for Pt/GrC support, showing similar relative percentage of C-F bond at the BOL

and EOL.
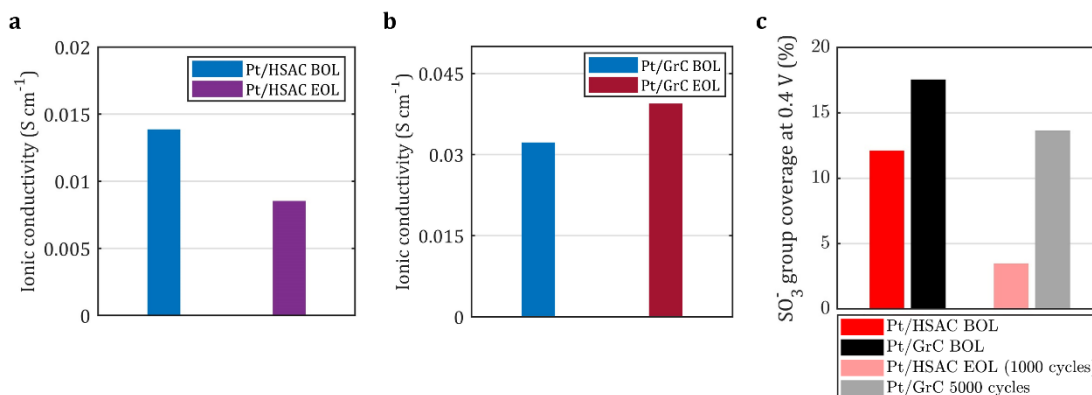
Figure 7.7 Catalyst layer ionic conductivity reduction for (a) Pt/HSAC, and (b) Pt/GrC. (c) SO$_3^-$ group coverage reduction for Pt/HSAC and Pt/GrC.

7.3 Conclusion.

Commercial PEFC MEAs with HSAC and GrC were subjected to the carbon corrosion AST adopted by U.S.DOE. Electrochemical characterizations and spectroscopic technologies were performed and the performance changes after ASTs were measured and summarized in Table 13. Carbon corroded during the AST and formed rougher carbon surfaces and created more contacts with ionomer and water, which resulted in increases of C_{dl} for Pt/HSAC (26.5 %) and Pt/GrC (85.8 %) at their EOLs after AST. Morphology for Pt/GrC support was more ordered and organized, however after AST, more disordered carbon surface contacts were created due to carbon oxidation leading to a more significant increase of C_{dl}. ECSA lost during AST for both Pt/HSAC and Pt/GrC because of Pt detachment and particle size growth. For Pt/HSAC, according to an increase of particle size of 76 % at EOL, Pt detachment was the major reason leading to the 59.7 % reduction of ECSA. However for Pt/GrC, a more significant particle size increase of 210 % was observed at EOL, which indicates Pt particle size growth was the principal reason that caused 44 % loss of ECSA. Apart from that, Pt loading distributions from XRF measurements ruled out Pt lost during AST causing the reductions of ECSA. At EOL, for

Pt/HSAC, catalyst layer thickness reduced 57 % leading to a 56.2 % increase of HFR due to

insufficient contacts between GDL and catalyst layer. For Pt/GrC, a catalyst layer thickness

reduction of 50.4 % was observed whereas the HFR almost maintained due to sufficient contacts

between GDL and catalyst layer after AST. Catalyst layer ionic conductivities decreased 38.6 %

for Pt/HSAC due to the collapse of catalyst layer porous structure, which reduced the

continuities of ionomer and water pathways. However for Pt/GrC, catalyst layer ionic

conductivity increased due to less tortuous H^+ pathways formation resulted from greater Pt

particles coalescence and sintering.

Table 13. Summarized changes of electrochemical characterizations for Pt/HSAC and Pt/GrC after carbon corrosion ASTs.

	HASC BOL	HASC 1000 cycles (EOL)	GrC BOL	GrC 10000 cycles (EOL)
C_{dl} (mF cm^{-2})	108.3	137	35.2	65.4
ECSA (m^2 g^{-1})	41.9	16.9	30.6	17.1
Pt loading (µg cm^{-2})	635	702	746	829
Pt particle size (nm)	2.25	3.96	2.67	8.27
Catalyst layer thickness (µm)	8	3.43	13	6.45
HFR (ohm*cm^2)	66	103.1	65.1	65.4
Catalyst layer ionic conductivity (S cm^{-1})	1.38e-2	8.47x10^{-3}	3.48x10^{-2}	3.93x10^{-2}

Chapter. 8 Conclusion, Contributions and Recommendations for Future work

8.1 Conclusions and Contributions

This dissertation studies catalyst layer interfacial and transport properties for PEFC, especially Pt/ionomer interfacial and transport properties. For ionomer transport property, and three different methods were used to investigate catalyst layer ionic conductivity. First, DC H_2 pump and AC H_2 pump methods were studied. After that, H_2/N_2 EIS method was applied and a developed H_2/N_2 EIS impedance fitting model based on de Levie's transmission line model was investigated. A first and unique comparison was made regarding these three different methods. Then Pt/ionomer interfacial properties and performance was studied on MEA using novel ionomer. Then some possible factors were investigated, for example, process of cell conditioning and voltage recovery, Pt loading, I/C ratio and different carbon support types. Pt/ionomer interfacial and transport properties change during carbon corrosion were investigated. The following subsections summarized the developments and findings of this research.

8.2 Recommendations for Future work

8.2.1 Determining Proton Transport in Pseudo Catalyst Layers Using Hydrogen Pump DC and AC Techniques

Due to the special cell geometry of H_2 pump. Electrode with Pt catalyst can not be placed with the membranes. Also since H_2 pump set up only takes account ionic pathways that fully though the PCL, H_2 pump set up indeed underestimate catalyst layer ionic conductivity. Apart from that, due to 6 or 10 PCLs were located between two membranes, RH saturation is a big issue. It is more likely if gases purging is applied for insufficient time, RH unevenness would occur within the PCLs, then it is difficult to study the ionic conductivity. Also, in H_2 pump work, as PCLs were hot pressed before assembled the cell. Another reason may should not be ignored is the contact resistance between each PCL even after hot press treatment. Once the some resistors corresponding to contact resistance are added in the equivalent circuit, the calculation method would be different. So developing the DC H_2 pump method must take account these issues above.

8.2.2 Interpreting Ionic Conductivity for Polymer Electrolyte Fuel Cell Catalyst Layers with Electrochemical Impedance Spectroscopy and Transmission Line Modeling

Catalyst layer ionic conductivity was also calculated using H_2/N_2 EIS method and the impedance fitting model. Using H_2/N_2 EIS impedance fitting model over estimates catalyst ionic conductivity since it takes account all the ionic pathways that connected to the membrane side. Also, our model is based on De Levie's transmission line mode, adopted Obermaier et al 's [58] model and did a lot of simplifications. It simplifies catalyst layer averaged pore size and pore distribution by using an equivalent cylindrical pore with a specific area of 1×10^8 1/m. Comparing to other models, due to simplifications made by our model, it might be very accurate

to some extent. According to the equivalent circuit, impedance of catalyst layer, double layer capacitance, resistance and capacitance of some side reactions for example H_2 crossover and anion groups adsorption were connected in parallel. Hence there are several outputs for instance catalyst layer ionic conductivity, double layer capacitance etc. However due to the assumption of specific area of 1×10^8 1/m, some of parameters can not be accurately evaluated, for example double layer capacitance. Future work need to be working on the building a more precise catalyst layer model take account more precise specific area.

8.2.3   High O_2 permeability ionomer for improved PEM fuel cell performance and electrochemical characterizations

Novel ionomer with porous backbone has much better performance at high current density region and reach 1.25 W/cm^2 with 1/3 SLPM H_2/air flow rate. Due to mass transport limitation was mitigated by the porous backbone, MEAs with PDD ionomer can have very high ionomer on Pt coverage. However, degradation on this novel type ionomer hasn't been investigated. Recommendation and suggestions regarding the durability study of this ionomer is related to ionomer RH cycling, which is using high air/air flow rate at 0 ℃ and 90 ℃ dew point. For each dew point, constant voltage hold at OCV for 5 seconds. Apart from that, the biggest concern of ionomer as SO_3^- group coverage poisoning still is the challenge for the community. For this PDD novel ionomer, PTFE backbone was replaced, however SO_3^- group and the side chain still didn't change. For the future work, overcoming the SO_3^- group poisoning is still one of the biggest change in PEFC field.

8.2.4   Determining Pt/ionomer interfacial properties using CO displacement/stripping methods.

Pt/ 3M PFSA ionomer interfacial and transport properties were comprehensively studied. For Vulcan carbon, at fully hydrated conditions, equivalent H^+ accessibility (ECSA) was also reached at dry condition. Which suggests us when manufacturing the catalyst layer, it is possible to well disperse the ionomer and enable a saturated ionomer coverage to provide an equivalent ECSA. Apart from that, due to thin ionomer film coverage, mass transport issue would be mitigated for MEA with low ionomer content. One improvement of the experimental setup is using the separated CO gas line, and should be considered in the future CO measurement.

8.2.5   Studying Pt/ionomer properties change during carbon corrosion AST.

HASC support improves Pt performance by increasing the ECSA of the cell, however it causes degradation problem since HSAC has great amount of amorphous carbon domain. This dissertation work studied carbon corrosion on different carbon supports comprehensively. However, MEAs used in this work had very high cathode side Pt loading, as shown as 0.5 mg/cm^2. Due to DOE's target [50], future Pt loading would be further decreased to 0.125 mg/cm^2. Suggestions and future work to this topic, is the durability studies using MEAs with low Pt loadings, for example, 0.1 mg/cm^2. Also carbon corrosion is not the only concern regarding degradation when PEFCs are operating. Pt degradation also occurs at high voltage operation mode (0.6-0.95 V). However Pt degradation studies also studied high Pt loading MEAs, and it would be insightful if low Pt loading MEAs are conducted degradation tests.

Reference

[1]   S.E. Hosseini, A.M. Andwari, M.A. Wahid, G. Bagheri, A review on green energy

       potentials in Iran, Renew. Sustain. Energy Rev. 27 (2013) 533–545.

       https://doi.org/10.1016/j.rser.2013.07.015.

[2]   M. Granovskii, I. Dincer, M.A. Rosen, Greenhouse gas emissions reduction by use of

       wind and solar energies for hydrogen and electricity production: Economic factors, Int. J.

       Hydrogen Energy. 32 (2007) 927–931. https://doi.org/10.1016/j.ijhydene.2006.09.029.

[3]   E.L.V. Eriksson, E.M.A. Gray, Optimization and integration of hybrid renewable energy

       hydrogen fuel cell energy systems – A critical review, Appl. Energy. 202 (2017) 348–364.

       https://doi.org/10.1016/j.apenergy.2017.03.132.

[4]   U.S.E.I. Administration, March 2022 Monthly Energy Review, 2022.

[5]   Y. Manoharan, S.E. Hosseini, B. Butler, H. Alzhahrani, B.T.F. Senior, T. Ashuri, J. Krohn,

       Hydrogen fuel cell vehicles; Current status and future prospect, Appl. Sci. 9 (2019) 2296.

       https://doi.org/10.3390/app9112296.

[6]   KPMG International, Industry leaders foresee dramatic changes, (2021).

[7]   T. Hasegawa, H. Imanishi, M. Nada, Y. Ikogi, Development of the Fuel Cell System in

       the Mirai FCV, SAE Tech. Pap. 2016-April (2016). https://doi.org/10.4271/2016-01-1185.

[8]   F.T. Wagner, B. Lakshmanan, M.F. Mathias, Electrochemistry and the future of the

       automobile, J. Phys. Chem. Lett. 1 (2010) 2204–2219. https://doi.org/10.1021/jz100553m.

[9]   H.A. Gasteiger, S.S. Kocha, B. Sompalli, F.T. Wagner, Activity benchmarks and

       requirements for Pt, Pt-alloy, and non-Pt oxygen reduction catalysts for PEMFCs, Appl.

Catal. B Environ. 56 (2005) 9–35. https://doi.org/10.1016/j.apcatb.2004.06.021.

[10]   J. Kast, R. Vijayagopal, J.J. Gangloff, J. Marcinkoski, Clean commercial transportation: Medium and heavy duty fuel cell electric trucks, Int. J. Hydrogen Energy. 42 (2017) 4508–4517. https://doi.org/10.1016/j.ijhydene.2016.12.129.

[11]   X. Liu, K. Reddi, A. Elgowainy, H. Lohse-Busch, M. Wang, N. Rustagi, Comparison of well-to-wheels energy use and emissions of a hydrogen fuel cell electric vehicle relative to a conventional gasoline-powered internal combustion engine vehicle, Int. J. Hydrogen Energy. 45 (2020) 972–983. https://doi.org/10.1016/j.ijhydene.2019.10.192.

[12]   X. Ren, Q. Lv, L. Liu, B. Liu, Y. Wang, A. Liu, G. Wu, Current progress of Pt and Pt-based electrocatalysts used for fuel cells, Sustain. Energy Fuels. 4 (2019) 15–30. https://doi.org/10.1039/c9se00460b.

[13]   W. Bernhart, S. Riederle, M. Yoon, W.G. Aulbur, Fuel Cells — A Realistic Alternative for Zero Emission?, Auto Tech Rev. 3 (2014) 20–23. https://doi.org/10.1365/s40112-014-0541-x.

[14]   A. Kongkanand, M.F. Mathias, The Priority and Challenge of High-Power Performance of Low-Platinum Proton-Exchange Membrane Fuel Cells, J. Phys. Chem. Lett. 7 (2016) 1127–1137. https://doi.org/10.1021/acs.jpclett.6b00216.

[15]   H.A. Gasteiger, J.E. Panels, S.G. Yan, Dependence of PEM fuel cell performance on catalyst loading, J. Power Sources. 127 (2004) 162–171. https://doi.org/10.1016/j.jpowsour.2003.09.013.

[16]   D.A. Cullen, K.C. Neyerlin, R.K. Ahluwalia, R. Mukundan, K.L. More, R.L. Borup, A.Z. Weber, D.J. Myers, A. Kusoglu, New roads and challenges for fuel cells in heavy-duty transportation, Nat. Energy. 6 (2021) 462–474. https://doi.org/10.1038/s41560-021-

00775-z.

[17]   B.D. James Jennie M Huya-Kouadio Cassidy Houchins Daniel A DeSantis Rev, Mass
        Production Cost Estimation of Direct H 2 PEM Fuel Cell Systems for Transportation,
        (2016) 1–43. www.sainc.com.

[18]   A.Z. Weber, A. Kusoglu, Unexplained transport resistances for low-loaded fuel-cell
        catalyst layers, J. Mater. Chem. A. 2 (2014) 17207–17211.
        https://doi.org/10.1039/c4ta02952f.

[19]   K. Sasaki, H. Naohara, Y. Cai, Y.M. Choi, P. Liu, M.B. Vukmirovic, J.X. Wang, R.R.
        Adzic, Core-protected platinum monolayer shell high-stability electrocatalysts for fuel-
        cell cathodes, Angew. Chemie - Int. Ed. 49 (2010) 8602–8607.
        https://doi.org/10.1002/anie.201004287.

[20]   S.L. Knupp, M.B. Vukmirovic, P. Haldar, J.A. Herron, M. Mavrikakis, R.R. Adzic,
        Platinum Monolayer Electrocatalysts for O 2 Reduction: Pt Monolayer on Carbon-
        Supported PdIr Nanoparticles, Electrocatalysis. 1 (2010) 213–223.
        https://doi.org/10.1007/s12678-010-0028-8.

[21]   L. Gan, C. Cui, M. Heggen, F. Dionigi, S. Rudi, P. Strasser, Element-specific anisotropic
        growth of shaped platinum alloy nanocrystals, Science (80-.). 346 (2014) 1502–1506.
        https://doi.org/10.1126/science.1261212.

[22]   S. Il Choi, S. Xie, M. Shao, J.H. Odell, N. Lu, H.C. Peng, L. Protsailo, S. Guerrero, J.
        Park, X. Xia, J. Wang, M.J. Kim, Y. Xia, Synthesis and characterization of 9 nm Pt-Ni
        octahedra with a record high activity of 3.3 A/mgPt for the oxygen reduction reaction,
        Nano Lett. 13 (2013) 3420–3425. https://doi.org/10.1021/nl401881z.

[23]   M.K. Carpenter, T.E. Moylan, R.S. Kukreja, M.H. Atwan, M.M. Tessema, Solvothermal

synthesis of platinum alloy nanoparticles for oxygen reduction electrocatalysis, J. Am. Chem. Soc. 134 (2012) 8535–8542. https://doi.org/10.1021/ja300756y.

[24]   J. Wu, J. Zhang, Z. Peng, S. Yang, F.T. Wagner, H. Yang, Truncated octahedral Pt3Ni oxygen reduction reaction electrocatalysts, J. Am. Chem. Soc. 132 (2010) 4984–4985. https://doi.org/10.1021/ja100571h.

[25]   J. Zhang, H. Yang, J. Fang, S. Zou, Synthesis and oxygen reduction activity of shape-controlled Pt 3Ni nanopolyhedra, Nano Lett. 10 (2010) 638–644. https://doi.org/10.1021/nl903717z.

[26]   Q. Jia, K. Caldwell, J.M. Ziegelbauer, A. Kongkanand, F.T. Wagner, S. Mukerjee, D.E. Ramaker, The Role of OOH Binding Site and Pt Surface Structure on ORR Activities, J. Electrochem. Soc. 161 (2014) F1323–F1329. https://doi.org/10.1149/2.1071412jes.

[27]   K.M. Caldwell, D.E. Ramaker, Q. Jia, S. Mukerjee, J.M. Ziegelbauer, R.S. Kukreja, A. Kongkanand, Spectroscopic in situ measurements of the relative pt skin thicknesses and porosities of dealloyed PtMn (Ni, Co) electrocatalysts, J. Phys. Chem. C. 119 (2015) 757–765. https://doi.org/10.1021/jp5098553.

[28]   M. Oezaslan, M. Heggen, P. Strasser, Size-Dependent morphology of dealloyed bimetallic catalysts: Linking the nano to the macro scale, J. Am. Chem. Soc. 134 (2012) 514–524. https://doi.org/10.1021/ja2088162.

[29]   N. Konno, S. Mizuno, H. Nakaji, Y. Ishikawa, Development of compact and high-performance fuel cell stack, SAE Int. J. Altern. Powertrains. 4 (2015) 123–129. https://doi.org/10.4271/2015-01-1175.

[30]   A. Haug, M. Lindell, J. Abulu, M. Yandrasits, G. Thoma, A. Steinbach, M. Kurkowski, G. Weatherman, I. Khan, F. Sun, M. Krueger, DOE 2018 Annual Merit Review, 2018.

[31] Z. Yang, S. Ball, D. Condit, M. Gummalla, Systematic Study on the Impact of Pt Particle Size and Operating Conditions on PEMFC Cathode Catalyst Durability, J. Electrochem. Soc. 158 (2011) B1439. https://doi.org/10.1149/2.081111jes.

[32] M. Gummalla, S.C. Ball, D.A. Condit, S. Rasouli, K. Yu, P.J. Ferreira, D.J. Myers, Z. Yang, Effect of particle size and operating conditions on Pt3Co PEMFC cathode catalyst durability, Catalysts. 5 (2015) 926–948. https://doi.org/10.3390/catal5020926.

[33] B.T. Sneed, D.A. Cullen, R. Mukundan, R.L. Borup, K.L. More, PtCo Cathode Catalyst Morphological and Compositional Changes after PEM Fuel Cell Accelerated Stress Testing, J. Electrochem. Soc. 165 (2018) F3078–F3084. https://doi.org/10.1149/2.0091806jes.

[34] D.D. Papadias, R.K. Ahluwalia, N. Kariuki, D. Myers, K.L. More, D.A. Cullen, B.T. Sneed, K.C. Neyerlin, R. Mukundan, R.L. Borup, Durability of Pt-Co Alloy Polymer Electrolyte Fuel Cell Cathode Catalysts under Accelerated Stress Tests, J. Electrochem. Soc. 165 (2018) F3166–F3177. https://doi.org/10.1149/2.0171806jes.

[35] T. Ioroi, Z. Siroma, S. ichi Yamazaki, K. Yasuda, Electrocatalysts for PEM Fuel Cells, Adv. Energy Mater. 9 (2019) 1–20. https://doi.org/10.1002/aenm.201801284.

[36] K. Yasuda, A. Taniguchi, T. Akita, T. Ioroi, Z. Siroma, Platinum dissolution and deposition in the polymer electrolyte membrane of a PEM fuel cell as studied by potential cycling, Phys. Chem. Chem. Phys. 8 (2006) 746–752. https://doi.org/10.1039/b514342j.

[37] S. Cherevko, N. Kulyk, K.J.J. Mayrhofer, Durability of platinum-based fuel cell electrocatalysts: Dissolution of bulk and nanoscale platinum, Nano Energy. 29 (2016) 275–298. https://doi.org/10.1016/j.nanoen.2016.03.005.

[38] J.C. Meier, C. Galeano, I. Katsounaros, J. Witte, H.J. Bongard, A.A. Topalov, C.

Baldizzone, S. Mezzavilla, F. Schüth, K.J.J. Mayrhofer, Design criteria for stable Pt/C fuel cell catalysts, Beilstein J. Nanotechnol. 5 (2014) 44–67. https://doi.org/10.3762/bjnano.5.5.

[39]　Y. Shao-Horn, W.C. Sheng, S. Chen, P.J. Ferreira, E.F. Holby, D. Morgan, Instability of supported platinum nanoparticles in low-temperature fuel cells, Top. Catal. 46 (2007) 285–305. https://doi.org/10.1007/s11244-007-9000-0.

[40]　R.K. Ahluwalia, D.D. Papadias, N.N. Kariuki, J.-K. Peng, X. Wang, Y. Tsai, D.G. Graczyk, D.J. Myers, Potential Dependence of Pt and Co Dissolution from Platinum-Cobalt Alloy PEFC Catalysts Using Time-Resolved Measurements, J. Electrochem. Soc. 165 (2018) F3024–F3035. https://doi.org/10.1149/2.0031806jes.

[41]　T.F. Cells, F. Cell, T. Office, F. Cells, T. Office, T.F. Cells, Fuel Cell 2016 Multi-Year Research, Development, and Demonstration Plan, 2015 (2016) 1–58.

[42]　K. Shinozaki, Y. Morimoto, B.S. Pivovar, S.S. Kocha, Suppression of oxygen reduction reaction activity on Pt-based electrocatalysts from ionomer incorporation, J. Power Sources. 325 (2016) 745–751. https://doi.org/10.1016/j.jpowsour.2016.06.062.

[43]　K. Shinozaki, J.W. Zack, S. Pylypenko, B.S. Pivovar, S.S. Kocha, Oxygen Reduction Reaction Measurements on Platinum Electrocatalysts Utilizing Rotating Disk Electrode Technique, J. Electrochem. Soc. 162 (2015) F1384–F1396. https://doi.org/10.1149/2.0551512jes.

[44]　R. Subbaraman, D. Strmcnik, V. Stamenkovic, N.M. Markovic, Three phase interfaces at electrified metal-solid electrolyte systems 1. study of the pt(hkl)-nafion interface, J. Phys. Chem. C. 114 (2010) 8414–8422. https://doi.org/10.1021/jp100814x.

[45]　R. Subbaraman, D. Strmcnik, A.P. Paulikas, V.R. Stamenkovic, N.M. Markovic, Oxygen

reduction reaction at three-phase interfaces, ChemPhysChem. 11 (2010) 2825–2833. https://doi.org/10.1002/cphc.201000190.

[46] K. Kodama, R. Jinnouchi, T. Suzuki, H. Murata, T. Hatanaka, Y. Morimoto, Increase in adsorptivity of sulfonate anions on Pt (111) surface with drying of ionomer, Electrochem. Commun. 36 (2013) 26–28. https://doi.org/10.1016/j.elecom.2013.09.005.

[47] K. Kodama, K. Motobayashi, A. Shinohara, N. Hasegawa, K. Kudo, R. Jinnouchi, M. Osawa, Y. Morimoto, Effect of the Side-Chain Structure of Perfluoro-Sulfonic Acid Ionomers on the Oxygen Reduction Reaction on the Surface of Pt, ACS Catal. 8 (2018) 694–700. https://doi.org/10.1021/acscatal.7b03571.

[48] J. Zhang, B. Litteer, F. Coms, R.R. Makharia, Recoverable Performance Loss due to Membrane Chemical Degradation in PEM Fuel Cells, ECS Meet. Abstr. MA2011-02 (2011) 1125–1125. https://doi.org/10.1149/ma2011-02/16/1125.

[49] S. Kabir, D.J. Myers, N. Kariuki, J. Park, G. Wang, A. Baker, N. Macauley, R. Mukundan, K.L. More, K.C. Neyerlin, Elucidating the Dynamic Nature of Fuel Cell Electrodes as a Function of Conditioning: An ex Situ Material Characterization and in Situ Electrochemical Diagnostic Study, ACS Appl. Mater. Interfaces. (2019). https://doi.org/10.1021/acsami.9b11365.

[50] N.G. Author, Fuel Cell Technical Team Roadmap, (2013). https://doi.org/10.2172/1220127.

[51] K. Kodama, A. Shinohara, N. Hasegawa, K. Shinozaki, R. Jinnouchi, T. Suzuki, T. Hatanaka, Y. Morimoto, Catalyst Poisoning Property of Sulfonimide Acid Ionomer on Pt (111) Surface, J. Electrochem. Soc. 161 (2014) F649–F652. https://doi.org/10.1149/2.051405jes.

[52] J.M. Orts, A. Fernández-Vega, J.M. Feliu, A. Aldaz, J. Clavilier, Electrochemical behaviour of CO layers formed by solution dosing at open circuit on Pt(111). Voltammetric determination of CO coverages at full hydrogen adsorption blocking in various acid media, J. Electroanal. Chem. 327 (1992) 261–278. https://doi.org/10.1016/0022-0728(92)80152-T.

[53] J.M. Feliu, J.M. Orts, R. Gómez, A. Aldaz, J. Clavilier, New information on the unusual adsorption states of Pt(111) in sulphuric acid solutions from potentiostatic adsorbate replacement by CO, J. Electroanal. Chem. 372 (1994) 265–268. https://doi.org/10.1016/0022-0728(93)03259-R.

[54] J. Clavilier, R. Albalat, R. Gomez, J.M. Orts, J.M. Feliu, A. Aldaz, Study of the charge displacement at constant potential during CO adsorption on Pt(110) and Pt(111) electrodes in contact with a perchloric acid solution, J. Electroanal. Chem. 330 (1992) 489–497. https://doi.org/10.1016/0022-0728(92)80326-Y.

[55] J. Clavilier, R. Albalat, R. Gómez, J.M. Orts, J.M. Feliu, Displacement of adsorbed iodine on platinum single-crystal electrodes by irreversible adsorption of CO at controlled potential, J. Electroanal. Chem. 360 (1993) 325–335. https://doi.org/10.1016/0022-0728(93)87025-Q.

[56] T.R. Garrick, T.E. Moylan, V. Yarlagadda, A. Kongkanand, Characterizing Electrolyte and Platinum Interface in PEM Fuel Cells Using CO Displacement, J. Electrochem. Soc. 164 (2017) F60–F64. https://doi.org/10.1149/2.0551702jes.

[57] Y. Liu, M.W. Murphy, D.R. Baker, W. Gu, C. Ji, J. Jorne, H.A. Gasteiger, Proton Conduction and Oxygen Reduction Kinetics in PEM Fuel Cell Cathodes: Effects of Ionomer-to-Carbon Ratio and Relative Humidity, J. Electrochem. Soc. 156 (2009) B970.

https://doi.org/10.1149/1.3143965.

[58] M. Obermaier, A.S. Bandarenka, C. Lohri-Tymozhynsky, A Comprehensive Physical Impedance Model of Polymer Electrolyte Fuel Cell Cathodes in Oxygen-free Atmosphere, Sci. Rep. 8 (2018) 1–9. https://doi.org/10.1038/s41598-018-23071-5.

[59] H. Iden, A. Ohma, An in situ technique for analyzing ionomer coverage in catalyst layers, J. Electroanal. Chem. 693 (2013) 34–41. https://doi.org/10.1016/j.jelechem.2013.01.026.

[60] S. Maass, F. Finsterwalder, G. Frank, R. Hartmann, C. Merten, Carbon support oxidation in PEM fuel cell cathodes, J. Power Sources. 176 (2008) 444–451. https://doi.org/10.1016/j.jpowsour.2007.08.053.

[61] K. Artyushkova, P. Atanassov, M. Dutta, S. Wessel, V. Colbow, Structural correlations: Design levers for performance and durability of catalyst layers, J. Power Sources. 284 (2015) 631–641. https://doi.org/10.1016/j.jpowsour.2015.02.135.

[62] A. Patel, K. Artyushkova, P. Atanassov, V. Colbow, M. Dutta, D. Harvey, S. Wessel, Investigating the effects of proton exchange membrane fuel cell conditions on carbon supported platinum electrocatalyst composition and performance, J. Vac. Sci. Technol. A Vacuum, Surfaces, Film. 30 (2012) 04D107. https://doi.org/10.1116/1.4707153.

[63] Y. Qi, J. Liu, D.C. Sabarirajan, Y. Huang, A. Perego, A.T. Haug, I. V. Zenyuk, Interpreting Ionic Conductivity for Polymer Electrolyte Fuel Cell Catalyst Layers with Electrochemical Impedance Spectroscopy and Transmission Line Modeling, J. Electrochem. Soc. 168 (2021) 054502. https://doi.org/10.1149/1945-7111/abf96d.

[64] T.A. Greszler, D. Caulk, P. Sinha, The Impact of Platinum Loading on Oxygen Transport Resistance, J. Electrochem. Soc. 159 (2012) F831–F840. https://doi.org/10.1149/2.061212jes.

[65]   Y. Liu, M.W. Murphy, D.R. Baker, W. Gu, C. Ji, J. Jorne, H.A. Gasteiger, Proton

Conduction and Oxygen Reduction Kinetics in PEM Fuel Cell Cathodes: Effects of

Ionomer-to-Carbon Ratio and Relative Humidity, J. Electrochem. Soc. 156 (2009) B970–

B980. https://doi.org/10.1149/1.3143965.

[66]   A. Kusoglu, T.J. Dursch, A.Z. Weber, Nanostructure/Swelling Relationships of Bulk and

Thin-Film PFSA Ionomers, Adv. Funct. Mater. 26 (2016) 4961–4975.

https://doi.org/10.1002/adfm.201600861.

[67]   F. Maillard, M. Eikerling, O. V. Cherstiouk, S. Schreier, E. Savinova, U. Stimming, Size

effects on reactivity of Pt nanoparticles in CO monolayer oxidation: The role of surface

mobility, Faraday Discuss. 125 (2004) 357–377. https://doi.org/10.1039/b303911k.

[68]   T. Binninger, E. Fabbri, R. Kötz, T.J. Schmidt, Determination of the Electrochemically

Active Surface Area of Metal-Oxide Supported Platinum Catalyst, J. Electrochem. Soc.

161 (2014) H121–H128. https://doi.org/10.1149/2.055403jes.

[69]   H. Iden, A. Ohma, K. Shinohara, Analysis of Proton Transport in Pseudo Catalyst Layers,

J. Electrochem. Soc. 156 (2009) B1078. https://doi.org/10.1149/1.3169514.

[70]   H. ANGERSTEIN-KOZLOWSKA; B. E. CONWAY and W. B. A. SHARP, Faraday

Trans. I, 1973., Langmuir. 43 (1973) 9–36.

[71]   D. Kramer, S.A. Freunberger, R. Flückiger, I.A. Schneider, A. Wokaun, F.N. Büchi, G.G.

Scherer, Electrochemical diffusimetry of fuel cell gas diffusion layers, J. Electroanal.

Chem. 612 (2008) 63–77.

[72]   M. Ciureanu, R. Roberge, Electrochemical impedance study of PEM fuel cells.

Experimental diagnostics and modeling of air cathodes, J. Phys. Chem. B. 105 (2002)

3531–3539. https://doi.org/10.1021/jp003273p.

[73] T. Soboleva, Z. Xie, Z. Shi, E. Tsang, T. Navessin, S. Holdcroft, Investigation of the through-plane impedance technique for evaluation of anisotropy of proton conducting polymer membranes, J. Electroanal. Chem. 622 (2008) 145–152. https://doi.org/10.1016/j.jelechem.2008.05.017.

[74] A. Kusoglu, A.Z. Weber, New Insights into Perfluorinated Sulfonic-Acid Ionomers, Chem. Rev. 117 (2017) 987–1104. https://doi.org/10.1021/acs.chemrev.6b00159.

[75] B.R. Matos, E.I. Santiago, J.F.Q. Rey, C.H. Scuracchio, G.L. Mantovani, L.A. Hirano, F.C. Fonseca, Dc Proton conductivity at low-frequency in Nafion conductivity spectrum probed by time-resolved SAXS measurements and impedance spectroscopy, J. Polym. Sci. Part B Polym. Phys. 53 (2015) 822–828. https://doi.org/10.1002/polb.23704.

[76] S. Ott, A. Orfanidi, H. Schmies, B. Anke, H.N. Nong, J. Hübner, U. Gernert, M. Gliech, M. Lerch, P. Strasser, Ionomer distribution control in porous carbon-supported catalyst layers for high-power and low Pt-loaded proton exchange membrane fuel cells, Nat. Mater. 19 (2020) 77–85. https://doi.org/10.1038/s41563-019-0487-0.

[77] A.Z. Weber, R.L. Borup, R.M. Darling, P.K. Das, T.J. Dursch, W. Gu, D. Harvey, A. Kusoglu, S. Litster, M.M. Mench, R. Mukundan, J.P. Owejan, J.G. Pharoah, M. Secanell, I. V. Zenyuk, A Critical Review of Modeling Transport Phenomena in Polymer-Electrolyte Fuel Cells, J. Electrochem. Soc. 161 (2014) F1254–F1299. https://doi.org/10.1149/2.0751412jes.

[78] T. Van Cleve, S. Khandavalli, A. Chowdhury, S. Medina, S. Pylypenko, M. Wang, K.L. More, N. Kariuki, D.J. Myers, A.Z. Weber, S.A. Mauger, M. Ulsh, K.C. Neyerlin, Dictating Pt-Based Electrocatalyst Performance in Polymer Electrolyte Fuel Cells, from Formulation to Application, ACS Appl. Mater. Interfaces. 11 (2019) 46953–46964.

https://doi.org/10.1021/acsami.9b17614.

[79] S.J. Normile, I. V. Zenyuk, Imaging ionomer in fuel cell catalyst layers with synchrotron nano transmission x-ray microscopy, Solid State Ionics. 335 (2019) 38–46. https://doi.org/10.1016/j.ssi.2019.02.017.

[80] Y. Liu, C. Ji, W. Gu, J. Jorne, H.A. Gasteiger, Effects of Catalyst Carbon Support on Proton Conduction and Cathode Performance in PEM Fuel Cells, J. Electrochem. Soc. 158 (2011) B614. https://doi.org/10.1149/1.3562945.

[81] I. Rubinstein, J. Rishpon, S. Gottesfeld, An AC-Impedance Study of Electrochemical Processes at Nafion-Coated Electrodes, J. Electrochem. Soc. 133 (1986) 729–734. https://doi.org/10.1149/1.2108663.

[82] R. Borup, J. Meyers, B. Pivovar, Y.S. Kim, R. Mukundan, N. Garland, D. Myers, M. Wilson, F. Garzon, D. Wood, P. Zelenay, K. More, K. Stroh, T. Zawodzinski, J. Boncella, J.E. McGrath, M. Inaba, K. Miyatake, M. Hori, K. Ota, Z. Ogumi, S. Miyata, A. Nishikata, Z. Siroma, Y. Uchimoto, K. Yasuda, K.I. Kimijima, N. Iwashita, Scientific aspects of polymer electrolyte fuel cell durability and degradation, Chem. Rev. 107 (2007) 3904–3951. https://doi.org/10.1021/cr050182l.

[83] M.C. Lefebvre, R.B. Martin, P.G. Pickup, Characterization of ionic conductivity profiles within proton exchange membrane fuel cell gas diffusion electrodes by impedance spectroscopy, Electrochem. Solid-State Lett. 2 (1999) 259–261. https://doi.org/10.1149/1.1390804.

[84] R. Makharia, M.F. Mathias, D.R. Baker, Measurement of Catalyst Layer Electrolyte Resistance in PEFCs Using Electrochemical Impedance Spectroscopy, J. Electrochem. Soc. 152 (2005) A970–A977. https://doi.org/10.1149/1.1888367.

[85] Y. Liu, C. Ji, W. Gu, D.R. Baker, J. Jorne, H.A. Gasteiger, Proton Conduction in PEM Fuel Cell Cathodes: Effects of Electrode Thickness and Ionomer Equivalent Weight, J. Electrochem. Soc. 157 (2010) B1154–B1162. https://doi.org/10.1149/1.3435323.

[86] R. Jiang, C.K. Mittelsteadt, C.S. Gittleman, Through-Plane Proton Transport Resistance of Membrane and Ohmic Resistance Distribution in Fuel Cells, J. Electrochem. Soc. 156 (2009) B1440–B1446. https://doi.org/10.1149/1.3240877.

[87] O.E. Barcia, E. D'Elia, I. Frateur, O.R. Mattos, N. Pébère, B. Tribollet, Application of the impedance model of de Levie for the characterization of porous electrodes, Electrochim. Acta. 47 (2002) 2109–2116. https://doi.org/10.1016/S0013-4686(02)00081-6.

[88] D.C. Sabarirajan, J. Liu, Y. Qi, A. Perego, A.T. Haug, I. V. Zenyuk, Determining Proton Transport in Pseudo Catalyst Layers Using Hydrogen Pump DC and AC Techniques, J. Electrochem. Soc. 167 (2020) 084521. https://doi.org/10.1149/1945-7111/ab927d.

[89] J. Zhao, A. Ozden, S. Shahgaldi, I.E. Alaefour, X. Li, F. Hamdullahpur, Effect of Pt loading and catalyst type on the pore structure of porous electrodes in polymer electrolyte membrane (PEM) fuel cells, Energy. 150 (2018) 69–76. https://doi.org/10.1016/j.energy.2018.02.134.

[90] D.C. Sabarirajan, J. Liu, Y. Qi, A. Perego, A. Haug, I. Zenyuk, Determining Proton Transport in Pseudo Catalyst Layers Using Hydrogen Pump DC and AC Techniques, J. Electrochem. Soc. 167 (2020) 084521. https://doi.org/10.1149/1945-7111/ab927d.

[91] J.T. Gostick, A.Z. Weber, Resistor-Network Modeling of Ionic Conduction in Polymer Electrolytes, Electrochim. Acta. 179 (2015) 137–145. https://doi.org/10.1016/j.electacta.2015.03.126.

[92] T.T. Nguyen, A. Demortière, B. Fleutot, B. Delobel, C. Delacourt, S.J. Cooper, The

electrode tortuosity factor: why the conventional tortuosity factor is not well suited for quantifying transport in porous Li-ion battery electrodes and what to use instead, Npj Comput. Mater. 6 (2020). https://doi.org/10.1038/s41524-020-00386-4.

[93] N. Ramaswamy, W. Gu, J.M. Ziegelbauer, S. Kumaraguru, Carbon Support Microstructure Impact on High Current Density Transport Resistances in PEMFC Cathode, J. Electrochem. Soc. 167 (2020) 064515. https://doi.org/10.1149/1945-7111/ab819c.

[94] N. Macauley, D.D. Papadias, J. Fairweather, D. Spernjak, D. Langlois, R. Ahluwalia, K.L. More, R. Mukundan, R.L. Borup, Carbon Corrosion in PEM Fuel Cells and the Development of Accelerated Stress Tests, J. Electrochem. Soc. 165 (2018) F3148–F3160. https://doi.org/10.1149/2.0061806jes.

[95] X.X. Wang, S. Hwang, Y.T. Pan, K. Chen, Y. He, S. Karakalos, H. Zhang, J.S. Spendelow, D. Su, G. Wu, Ordered Pt3Co Intermetallic Nanoparticles Derived from Metal-Organic Frameworks for Oxygen Reduction, Nano Lett. 18 (2018) 4163–4171. https://doi.org/10.1021/acs.nanolett.8b00978.

[96] A. Kongkanand, N.P. Subramanian, Y. Yu, Z. Liu, H. Igarashi, D.A. Muller, Achieving High-Power PEM Fuel Cell Performance with an Ultralow-Pt-Content Core-Shell Catalyst, ACS Catal. 6 (2016) 1578–1583. https://doi.org/10.1021/acscatal.5b02819.

[97] S. Jomori, K. Komatsubara, N. Nonoyama, M. Kato, T. Yoshida, An Experimental Study of the Effects of Operational History on Activity Changes in a PEMFC, J. Electrochem. Soc. 160 (2013) F1067–F1073. https://doi.org/10.1149/2.103309jes.

[98] H. Iden, T. Mashio, A. Ohma, Gas transport inside and outside carbon supports of catalyst layers for PEM fuel cells, J. Electroanal. Chem. 708 (2013) 87–94. https://doi.org/10.1016/j.jelechem.2013.09.011.

[99]   A. Orfanidi, P. Madkikar, H.A. El-Sayed, G.S. Harzer, T. Kratky, H.A. Gasteiger, The Key to High Performance Low Pt Loaded Electrodes, J. Electrochem. Soc. 164 (2017) F418–F426. https://doi.org/10.1149/2.1621704jes.

[100] H. Liu, W.K. Epting, S. Litster, Gas Transport Resistance in Polymer Electrolyte Thin Films on Oxygen Reduction Reaction Catalysts, Langmuir. 31 (2015) 9853–9858. https://doi.org/10.1021/acs.langmuir.5b02487.

[101] K. Shinozaki, Y. Morimoto, J.W. Zack, S. Pylypenko, R.M. Richards, B.S. Pivovar, S.S. Kocha, Special Feature : Popularizing Fuel Cell Vehicles : Designing and Controlling Electrochemical Reactions in the MEA Oxygen Reduction Reaction Activity Measurement for Fuel Cell Catalysts Using the Rotating Disk Electrode Technique, 49 (2018) 33–46.

[102] R. Jinnouchi, K. Kudo, N. Kitano, Y. Morimoto, Molecular Dynamics Simulations on O2 Permeation through Nafion Ionomer on Platinum Surface, Electrochim. Acta. 188 (2016) 767–776. https://doi.org/10.1016/j.electacta.2015.12.031.

[103] W. Yoon, A.Z. Weber, Modeling Low-Platinum-Loading Effects in Fuel-Cell Catalyst Layers, J. Electrochem. Soc. 158 (2011) B1007. https://doi.org/10.1149/1.3597644.

[104] A.D. Modestov, A. V. Kapustin, V.B. Avakov, I.K. Landgraf, M.R. Tarasevich, Cathode catalyst layers with ionomer to carbon mass ratios in the range 0-2 studied by electrochemical impedance spectroscopy, cyclic voltammetry, and performance measurements, J. Power Sources. 272 (2014) 735–742. https://doi.org/10.1016/j.jpowsour.2014.08.113.

[105] R. Shimizu, Y.-C. Park, K. Kakinuma, A. Iiyama, M. Uchida, Effects of Both Oxygen Permeability and Ion Exchange Capacity for Cathode Ionomers on the Performance and

Durability of Polymer Electrolyte Fuel Cells, J. Electrochem. Soc. 165 (2018) F3063–F3071. https://doi.org/10.1149/2.0071806jes.

[106] T. Asset, R. Chattot, M. Fontana, B. Mercier-Guyon, N. Job, L. Dubau, F. Maillard, A Review on Recent Developments and Prospects for the Oxygen Reduction Reaction on Hollow Pt-alloy Nanoparticles, ChemPhysChem. 19 (2018) 1552–1567. https://doi.org/10.1002/cphc.201800153.

[107] I. V. Zenyuk, S. Litster, Modeling ion conduction and electrochemical reactions in water films on thin-film metal electrodes with application to low temperature fuel cells, Electrochim. Acta. 146 (2014) 194–206. https://doi.org/10.1016/j.electacta.2014.08.070.

[108] A. Katzenberg, A. Chowdhury, M. Fang, A.Z. Weber, Y. Okamoto, A. Kusoglu, M.A. Modestino, Highly Permeable Perfluorinated Sulfonic Acid Ionomers for Improved Electrochemical Devices: Insights into Structure-Property Relationships, J. Am. Chem. Soc. 142 (2020) 3742–3752. https://doi.org/10.1021/jacs.9b09170.

[109] Y. Qi, J. Liu, D.C. Sabarirajan, Y. Huang, A. Perego, A.T. Haug, I. V. Zenyuk, Interpreting Ionic Conductivity for Polymer Electrolyte Fuel Cell Catalyst Layers with Electrochemical Impedance Spectroscopy and Transmission Line Modeling, J. Electrochem. Soc. 168 (2021) 054502. https://doi.org/10.1149/1945-7111/abf96d.

[110] J.K. Clark, S.J. Paddison, Side chain flexibility in perfluorosulfonic acid ionomers: An Ab initio study, J. Phys. Chem. A. 117 (2013) 10534–10543. https://doi.org/10.1021/jp407568d.

[111] S.G. Chalk, J.F. Miller, Key challenges and recent progress in batteries, fuel cells, and hydrogen storage for clean energy systems, J. Power Sources. 159 (2006) 73–80. https://doi.org/10.1016/j.jpowsour.2006.04.058.

[112] M.S. Wilson, F.H. Garzon, K.E. Sickafus, S. Gottesfeld, Surface Area Loss of Supported Platinum in Polymer Electrolyte Fuel Cells, J. Electrochem. Soc. 140 (1993) 2872–2877. https://doi.org/10.1149/1.2220925.

[113] A. Taniguchi, T. Akita, K. Yasuda, Y. Miyazaki, Analysis of electrocatalyst degradation in PEMFC caused by cell reversal during fuel starvation, J. Power Sources. 130 (2004) 42–49. https://doi.org/10.1016/j.jpowsour.2003.12.035.

[114] R. Borup, A. Weber, FC135 : FC-PAD : Fuel Cell Performance and Durability Consortium, 2019 DOE Fuel Cell Technol. Off. Annu. Merit Rev. 1 (2020) 1–42.

[115] Q. Shen, M. Hou, D. Liang, Z. Zhou, X. Li, Z. Shao, B. Yi, Study on the processes of start-up and shutdown in proton exchange membrane fuel cells, J. Power Sources. 189 (2009) 1114–1119. https://doi.org/10.1016/j.jpowsour.2008.12.075.

[116] E. Brightman, G. Hinds, In situ mapping of potential transients during start-up and shut-down of a polymer electrolyte membrane fuel cell, J. Power Sources. 267 (2014) 160–170. https://doi.org/10.1016/j.jpowsour.2014.05.040.

[117] P. Mandal, B.K. Hong, J.G. Oh, S. Litster, Understanding the voltage reversal behavior of automotive fuel cells, J. Power Sources. 397 (2018) 397–404. https://doi.org/10.1016/j.jpowsour.2018.06.083.

[118] N. Garland, T. Benjamin, DOE Fuel Cell Program: Durability Technical Targets and Testing Protocols, ECS Meet. Abstr. MA2007-02 (2007) 589–589. https://doi.org/10.1149/ma2007-02/9/589.

[119] L. Castanheira, W.O. Silva, F.H.B. Lima, A. Crisci, L. Dubau, F. Maillard, Carbon corrosion in proton-exchange membrane fuel cells: Effect of the carbon structure, the degradation protocol, and the gas atmosphere, ACS Catal. 5 (2015) 2184–2194.

https://doi.org/10.1021/cs501973j.

[120] K. Miyazaki, H. Shirakata, T. Abe, N. Yoshizawa, Z. Ogumi, Novel graphitised carbonaceous materials for use as a highly corrosion-tolerant catalyst support in polymer electrolyte fuel cells, Fuel Cells. 10 (2010) 960–965. https://doi.org/10.1002/fuce.201000075.

[121] H.S. Oh, K.H. Lim, B. Roh, I. Hwang, H. Kim, Corrosion resistance and sintering effect of carbon supports in polymer electrolyte membrane fuel cells, Electrochim. Acta. 54 (2009) 6515–6521. https://doi.org/10.1016/j.electacta.2009.06.028.

[122] S. Vinod Selvaganesh, G. Selvarani, P. Sridhar, S. Pitchumani, A.K. Shukla, Graphitic carbon as durable cathode-catalyst support for PEFCs, Fuel Cells. 11 (2011) 372–384. https://doi.org/10.1002/fuce.201000151.

[123] N. Linse, L. Gubler, G.G. Scherer, A. Wokaun, The effect of platinum on carbon corrosion behavior in polymer electrolyte fuel cells, Electrochim. Acta. 56 (2011) 7541–7549. https://doi.org/10.1016/j.electacta.2011.06.093.

[124] T. Mittermeier, A. Weiß, F. Hasché, H.A. Gasteiger, PEM Fuel Cell Start-Up/Shut-Down Losses vs Relative Humidity: The Impact of Water in the Electrode Layer on Carbon Corrosion, J. Electrochem. Soc. 165 (2018) F1349–F1357. https://doi.org/10.1149/2.0931816jes.

[125] A.G. Star, T.F. Fuller, FIB-SEM Tomography Connects Microstructure to Corrosion-Induced Performance Loss in PEMFC Cathodes, J. Electrochem. Soc. 164 (2017) F901–F907. https://doi.org/10.1149/2.0321709jes.

[126] F. Hegge, J. Sharman, R. Moroni, S. Thiele, R. Zengerle, M. Breitwieser, S. Vierrath, Impact of Carbon Support Corrosion on Performance Losses in Polymer Electrolyte

Membrane Fuel Cells, J. Electrochem. Soc. 166 (2019) F956–F962.

https://doi.org/10.1149/2.0611913jes.